Investigation of the Mott transition in chromium doped V2O3 by means of ultrasound and thermopower experiments

Sascha Populoh

ORSAY
N° d'ordre: 9437

THÈSE de DOCTORAT de l'UNIVERSITÉ PARIS SUD (PARIS XI)

présentée par:
Sascha Populoh

pour obtenir le titre de:
DOCTEUR DE L'UNIVERSITÉ PARIS XI

Investigation of the Mott transition in chromium doped V_2O_3 by means of ultrasound and thermopower experiments

Soutenue le 19 Juin 2009 devant la comission d'examen:

Michel Héritier
Michael Lang
Marino Marsi
Cyril Proust
Charles Simon
Pawel Wzietek

Acknowledgements

Many people contributed to this work and it would not have been possible to achieve this without their help.
First of all I want to thank my supervisor Pawel Wzietek, for whom it has been a pleasure to work for. His scientific knowledge and practical abilities deeply impressed me and allowed me to learn and advance with my work as it would not have been possible without him. Apart from all the scientific advices he helped me getting settled down in France and introduced me to the world of wine.
Next, I also want to thank Cyril Proust and Charles Simon who kindly accepted to be the referees of my work and the other members of my jury Michel Héritier, Michael Lang and Marino Marsi.
I also want to thank Claude Pasquier who especially helped me in the part about thermoelectric power in my thesis. His suggestions and the useful discussions with him provided much of the insights I gained on this subject.
Also I am thankful for the aid by Pascale Auban-Senzier who helped me with the sample preparation, gave help in technical question and often gave me a lift to the lab in case of strikes of the public transport.
I would like to thank the entire group HP at the LPS and the actual and former members Denis Jerome, Ning Kang, Belal Salameh, Nada Caud, and Patrice Limelette, who contributed to the good time I spent here.
Further I would like to express my gratitude towards Jean Yves Prieur, Luca di Medici, Marcelo Rozenberg, Antoine Georges and the workshop staff of the LPS.
My friends Alessandro, Andreas K., Andreas P., Gabriel, Johann, Jorge, Mirna, Mohammed, Peter, and the other PhD students and Post-docs of our lab, who greatly contributed to my pleasant stay in Orsay.
I am especially thankful to Johann and Kathrin for helping me on the spell check of this work.
My acknowledgements to the European Union that by financing my thesis with a Marie Curie Fellowship allowed me to carry out my work in France.
Finally, I thank my family and friends for their constant encouragement and support of my study.

I would like to dedicate this work to my mother and hope this achievement would have made her proud.

Contents

List of Figures

List of Tables

Chapter 1

General introduction

1.1 Introduction

The general goal of this thesis is to investigate the high temperature metal-insulator transition from the paramagnetic metallic to the paramagnetic insulating phase of $(V_{0.989}\,Cr_{0.011})_2O_3$ near the critical point by means of two different experimental techniques.

The first experimental technique we will employ is the measurement of the speed of sound. In the framework of the compressible Hubbard model it could be shown by Majumdar and Krishnamurthy [1, 2] that lattice effects might be responsible for the actual transition temperature that is different from purely electronic temperature. This model was recently applied to the speed of sound by Hassan et al. [3]. The basic concepts of these models will be presented in chapter 2. Within this work we will try to find evidence for the predicted vanishing of the speed of sound at a critical electronic temperature that differs from the temperature where the system actually transits and we will present the first systematic experimental study of the difference of these temperatures.

The second technique is the measurement of the thermoelectric power. We will try to get a complete picture of the variation of the Seebeck coefficient as a function of temperature and pressure. The thermoelectric power itself is a quantity difficult to interpret theoretically, but from the relation between S and the electrical conductivity σ we will be able to gain information about the variation of the electron-hole symmetry at the transition which is otherwise experimentally very difficult to access or even inaccessible. For this, we will compare our findings to the work of Limelette et al. [4, 5].

1.2 General plan of this thesis

In order to get familiar with this very important area of the physics of strongly correlated electron system, *the second chapter* is devoted to a brief introduction to the field of metal-insulator transitions. Several examples where this transition can be observed will be briefly discussed, including the driving mechanisms, before the basic theoretical descriptions in this field will be introduced. Commencing with the earliest works in this field an overview will be given towards the modern, more sophisticated model of the DMFT including examples where actual theoretical predictions were made, which will be verified as a part of this work.
In transition-metal oxides the electronic properties are determined by electron interactions. The transition-metal ions, for example d-shell electrons, experience localisation by Coulomb repulsion and delocalisation by hybridization with the oxygen p electron states. The subtle balance of the two competing forces makes many of the transition-metal oxides excellent resources for studying and taking advantage of the metal-insulator transition. In *the third chapter* of this thesis our sample system the transition-metal oxide V_2O_3 and systems derived from it by substitution of Vanadium by other transition metals will be introduced and their basic features will be described.
Further, the sample preparation will be illustrated. The high temperature metal-insulator transition (MIT) of $(V_{1-x}\ Cr_x)_2O_3$ is studied by means of hydrostatic pressure and in *the fourth chapter* the high pressure facility will be presented along with the experimental techniques used to investigate the transition, a new experimental set-up for the determination of the speed of sound and another for the estimation of the thermoelectric effect.
In *the fifth chapter* of this work the connection between the elastic constants and crystal symmetry will allow us to calculate the important modes for the propagation of sound waves within our sample system. Afterwards, several existing important results for the speed of sound and the elastic constants will be mentioned before the findings of our own experiments will be presented and analysed.
Subsequently, in *the sixth chapter* of this dissertation the second experimental technique used to investigate the MIT is described in detail. Some values of the literature are given to make it possible to compare our findings. Subsequently, the approach to measure not only the thermopower but also the heat conductivity at the same time is theoretically justified and the results of this trial shown. In the next part the data obtained in our experiments will be discussed and analysed.
Finally, in *the seventh chapter* a comparison between the experimental conclusions of both techniques will be taken and perspectives for further work in this area will be shown.

Chapter 2

Metal-insulator transitions

In the earliest effective theories describing metals (one early example is [6] by H. Bethe), insulators and transitions between them are based on just weakly or non-interacting electron systems. Here the general distinction between metals and insulators is made by the filling of the electronic bands at zero temperature: in the case of an insulator the highest filled band is completely filled and in the case of a metal it is only partially filled. In this theory the band structure formation is totally due to the periodic lattice structure in a crystal. In 1931 a model describing metals, insulators and semi-conductors was presented by Wilson [7].
Although this picture was successful in many respects, however the discovery of many transition-metal oxides with a partially filled d-electron band that were found to be only poor conductors or even insulators [8] could not be explained by this theory.
It became clear that electron-electron correlation played an important role: strong Coulomb repulsion between electrons could be the origin of the insulating behaviour. A term for the electron-electron interaction e^2/r_{12} was introduced in 1938 by Wigner [9].
By these discoveries the long and still continuing development of the field of strongly correlated electrons had begun, particularly with regard to the understanding of the conditions under which a system with partially filled bands could be an insulator and later also how an insulator could become a metal as controllable parameters were varied.
In order to solidify these parameters that allow control of metal-insulator transitions (MIT), in the following chapter this topic will be shortly summarised and two different ways of control will be introduced with a number of relevant examples of MIT and their controllable parameters.
In order to show the variety of effects in the mechanisms of MIT in the second short chapter two examples for the origin of the insulating state in transition metal oxides will be briefly discussed.

Finally, in the last part of this chapter the Mott MIT, which is for us the most interesting MIT will be reviewed in greater detail. Starting from the easiest theoretical models to describe this MIT to recent much more sophisticated approaches will be shortly described, including some results directly related to this work.

2.1 Two routes towards MIT

The two important parameters in the Hubbard model (see below) are the electron correlation strength U/t, where U is the on site Coulomb repulsion and t is the hopping probability for one electron to another site, and the filling of the band n [1]. A schematic phase diagram of the metal-insulator transition depending on these two parameters can be found in Fig. 2.1. In the case of a non degenerate

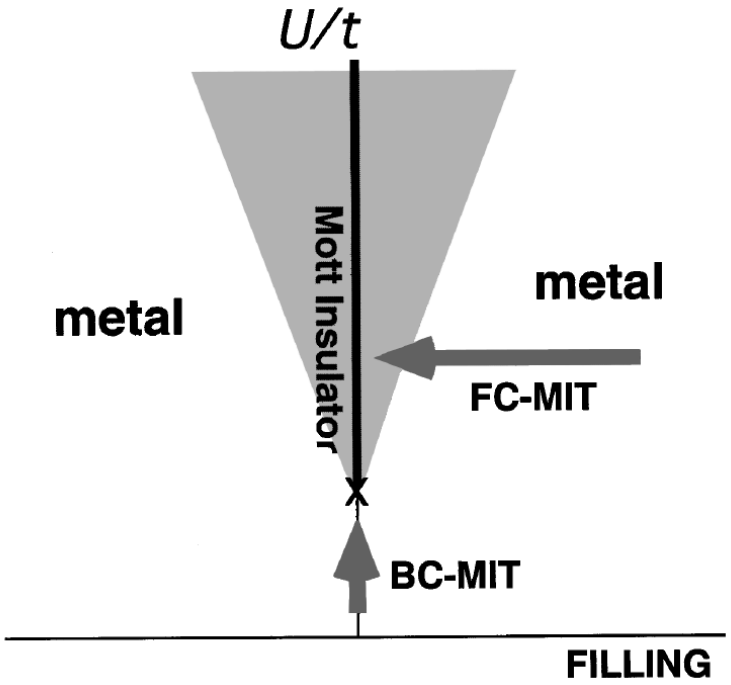

Figure 2.1: Phase diagram of a metal-insulator transition (based on the Hubbard model) in the plane U/t and filling n. In principle the shaded area is metallic, but it is under the strong influence of the metal-insulator transition. In this area the the carriers can easily be localised by external forces like electron-lattice coupling etc. For the actual MIT two different ways are shown: the filling control MIT (FC-MIT) and the bandwidth-control MIT (BC-MIT) [10].

[1] We use the convention that for a half filled band n equals 1

band a band insulator is existing for fillings of $n = 0$ and $n = 2$. For $n = 1$ the band is half-filled and a change of the ratio of the interaction to the bandwidth U/t drives the MIT at a critical value U_c/t. For the actual value the shape of the Fermi surface also plays a role, as for example in the case of perfect nesting where the critical value U_c is 0. At finite values of U_c this transition is called a *bandwidth control* (BC)-MIT. The electron correlation can be controlled by modifying the lattice parameters or the chemical composition while keeping the lattice structure unchanged. Because the Coulomb interaction is kept nearly unchanged during this approach usually the transfer integral t or the one-electron bandwidth W is the controlling parameter.

One method to control W is to apply hydrostatic pressure, because applied pressure decreases the interatomic distance and thus increases the transfer interaction. Typical examples of pressure induced Mott MIT are observed in V_2O_3 (e.g. [11]) and $RNiO_3$ (R = Pr or Nd) [12]. One downside of this method is that we have to know how pressure affects the lattice parameter to be able to obtain a more quantitative picture of the transition and this can in some cases prove to be a very difficult task.

Organic compounds are a further example where hydrostatic pressure can be used to control the bandwidth and thus to induce a MIT as, for example, for $\kappa-(BEDT-TTF)_2\,Cu\,[N\,(CN)_2]\,Cl$ it was shown by Lefebvre et al. in NMR experiments [13] and by Limelette et al. in transport measurements [14]. Furthermore, in organic compounds it is also possible to apply chemical pressure by anion substitution [15].

Another possibility to control W is the modification of the chemical composition using the solid solution or mixed crystal effect. One example for this kind of BC-MIT is the $NiS_{2-x}Se_x$ [16] compound, which undergoes the MIT at room temperature for $x = 0.6$. The substitution of S by Se enlarges the $2p$ band and increases the $d-p$ hybridisation.

In perovskite-type compounds, ABO_3, it is possible to control W by modification of the ionic radius of the A side r_A, since the change of r_A allows to vary continuously the $B-O-B$ bond angle (θ) in the orthorombic lattice. A change of θ on its part changes the one-electron bandwidth W, as the effective d electron transfer interaction of the adjacent B states is controlled by super-transfer processes over the O $2p$ sites. The huge advantage of this technique is that the electronic properties of the perovskite-systems are controlled by the $B-O$ network and the A side is nearly not relevant. A prime example for W control is the MIT in $RNiO_3$, where R stands for a trivalent rare-earth ion as La or Lu [17].

In case of non-integer band-filling n (see Fig. 2.1) a metal is to be expected. In metals with a filling near the insulating line $n = 1$ a *filling control* (FC)-MIT can be derived from the parent Mott insulator.

The importance of filling control has become widely recognised with the dis-

covery of high-temperature superconductivity as a function of filling in layered cuprate compounds. One possibility to achieve FC-MIT is to use ternary or multinary compositions in which ionic sites different from $3d$ ($4d$) or $2p$ electron related sites can be occupied by different valence ions. The band filling (n), for example, in $La_{2-x}Sr_xCuO_4$ is controllable by substitution of the divalent Sr on the sites of the trivalent La (n is given by the relation $n = 1 - x$) [18].
In a similar manner a large number of filling controlled components can be established by forming A-site mixed crystals of perovskites. An example here is $La_{1-x}Sr_xMO_3$, with M being a $3d$ transition metal element.
The perovskites yield a vast area of metal-insulator transitions which can be controlled by filling as well as by bandwidth. In Fig. 2.2 a schematic phase diagram showing the wide range of band fillings by A-site substitution in this material class can be found. The relative electron correlation U/W is an ordinate, the band fill-

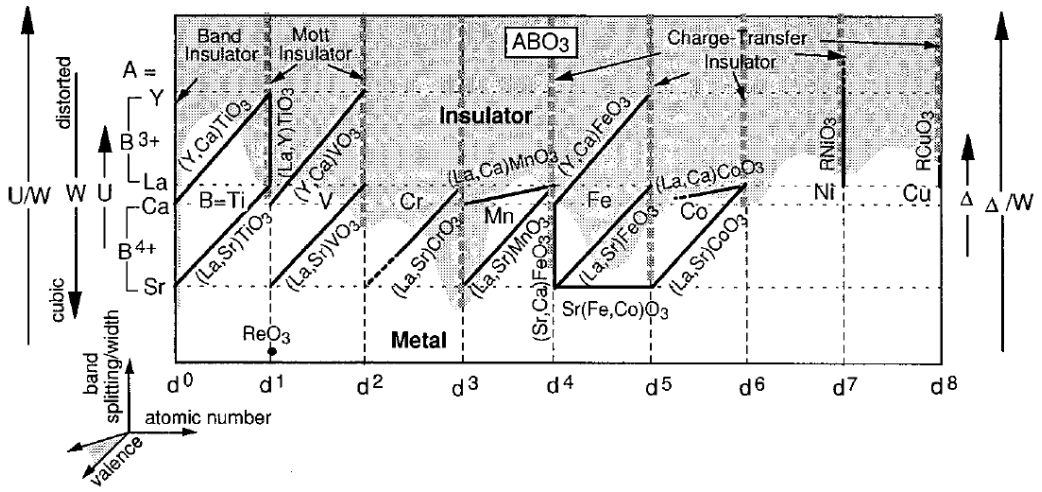

Figure 2.2: Different perovskite-type oxides plotted against A side cation and the filling of the d-band [19].

ing of the $3d$ band an abscissa and the filling controlled MIT in the $A_xA^*_{1-x}BO_3$ components is represented by the black lines as a function of the chemical composition x, showing the mixed-crystals that could have been synthesised successfully until now.
Another possibility is to employ filling control by non-stoichiometry, as for example in $YBa_2Cu_3O_{6+y}$ [20]. Here the reduction of the oxygen content from $y = 1$ towards $y = 0$ drives the system around $y \approx 0.4$ to a Mott insulator. During this process the nominal valence of Cu is reduced from $\approx +2.5$ for the compounds with $y = 1$ to $+1$ for $y = 0$. Further examples of filling control by non-stoichiometry are $V_{2-y}O_3$ (i. e. [21]) and $LaTiO_{3+y}$ [22].

2.2 Overview of different metal-insulator transitions

In strongly correlated materials, as for example in the oxides of the transition metals, the electronic properties depend not only on the filling of the bands as already mentioned above, but also on the bandwidth and the Coulomb interaction, which themselves strongly depend on the precise structure of every component. Additionally, the interaction of the conduction bands with the neighbouring valence bands is another pivotal factor. In the case of the oxides the atoms of the metallic structure realise a hybridisation with the oxygen neighbours, which in most cases reduces the bandwidth and emphasises the relative correlation effects. Taking t as the kinetic energy of the electrons, U as the Coulomb interaction within the d orbital and Δ as the energy of the charge transfer between the d orbital and the neighbouring p orbital, we can distinguish the following cases in the example of transition metal oxides. If $\Delta \gg U \gg t$ the electrons are localised in the d band and as U is much bigger than t the system is in the so called Mott insulating state. In the next case, which appears when $U \gg \Delta \gg t$, the electrons are blocked by the oxygen sites, a so called charge transfer insulator. When $t \geq U$ or Δ these two different kinds of insulators undergo an insulator to metal transition and form a metallic state in which interaction effects are still very important.

2.3 The Mott metal-insulator transition

The first very important steps for a theoretical understanding how electron-electron correlations could explain the insulating state were taken by N. F. Mott in a series of papers [23, 24, 25, 26]. To honour him for his contribution the insulating state due to electron-electron correlations is now called a *Mott insulator*. It will be briefly explained in the following chapter.

A milestone for the theoretical understanding of the transition between the Mott insulator and a metal was the employment of simplified models for the lattice fermions. Particularly, the so called *Hubbard model* was very successful and proved itself as a powerful tool in this context. This model was proposed in the 1960s by J. Hubbard [27, 28, 29]. It considers only the electrons in a single band and gives a simplified Hamiltonian to describe the problem. *The Hubbard model* will be described in detail below.

But even in this very simplified model the Hamiltonian can only be solved exactly in one dimension. Within *Dynamic mean-field theory (DMFT)* the lattice problem is replaced by a single site quantum impurity in an effective medium [30]. Though the DMFT becomes exact for infinite dimensions [31] and can, in analogy to the

Weiss mean-field theory for most investigations in the classical statistical mechanics, be viewed as a starting point for many finite-dimensional strongly correlated systems. Some important results of DMFT concerning metal-insulator transitions will be reviewed below.

2.3.1 The Mott-insulating state

N.F. Mott proposed a lattice model with a single electronic orbital per site. Without any electron-electron interactions this would lead to a single band formed by the overlapping of the different atomic orbitals of this system. This band would be fully filled with two electrons of opposite spin at each site. But the two electrons on the same site would be exposed to a large Coulomb repulsion, which Mott argued would split the band in two: a lower band formed from electrons that occupy an empty site and an upper band from electrons that occupy a site already containing another electron. These two electrons would be separated by an energy gap equal to the Coulomb repulsion and for systems with one electron per site the lower band would be full and the system an insulator.
In a paper of 1949 [23] Mott was able to employ his model to qualitatively explain the insulating properties of pure NiO.
In his original work Mott argued that the existence of the insulator did not depend on whether the system is magnetic or not, but most of the Mott insulators show magnetic ordering at least at zero temperature. Mott [24] predicted the transition would be of first order due to the competition between screening and carrier density. It should be noted that the validity of Mott's argument is still a subject of debate [10].

2.3.2 The Hubbard model

This prototype model for the theoretical understanding of the transition between a Mott insulator and a metal was proposed by J. Hubbard and commences with an oversimplification of the situation with barely the minimum of features needed to afford band-like and localized behaviour of the electrons in suitable limits. The vast variety of bound and continuum electron levels of each ion is reduced to a single localized orbital level. For each ion there are four different possible configurations (its levels can be empty, they can contain one electron with either of both spins or two electrons of opposite spins) and the states of this model are defined by specifying the configuration for every ion.
The Hamiltonian describing the model is of this form:

$$H = H_t + H_U = \sum_{<ij>,\sigma} t\left(c^{\dagger}_{i\sigma}c_{j\sigma} + h.c.\right) + U\sum_i n_{i\uparrow}n_{i\downarrow}. \qquad (2.1)$$

Here $c^{\dagger}_{i\sigma}$ and $c_{j\sigma}$ are, respectively the annihilation and creation operators for an electron of spin σ in the Wannier state at the lattice position i and $n_{i\sigma} = c^{\dagger}_{i\sigma}c_{i\sigma}$ is the occupation number operator. The summation <ij> is over nearest neighbours (usually periodic boundary conditions are presumed, with the result that <ij> includes a term coupling opposite edges). t represents the hopping probability for one electron to another site and U the correlation energy at a site (Coulomb repulsion).

The Hamiltonian can be divided in two types of terms: H_U is diagonal in the above described states and is just a positive energy U multiplied by the number of double occupied ionic levels; and a term H_t off-diagonal in these states that has nonvanishing matrix elements t between just those pairs of states that differ only by a single electron having been moved (without change in spin) from a given ion to one of its neighbours.

Thus it is convenient to use this Hamiltonian for the modelling of a metal-insulator transition, because the H_U set of terms, in the case of the absence of H_t, would result in localized single electrons, because the possibility of a second electron at single occupied sites is suppressed. The second set of terms in absence of the first leads to a conventional band spectrum and one-electron Bloch levels in which each electron is distributed throughout the entire crystal.

As a result of the used simplifications it is implied that the Hubbard Hamiltonian neglects multiband effects and thereby is, strictly spoken, only valid when the atom has only a single orbital, as in hydrogen. When this model is used for d-electron systems, it assumes implicitly that orbital degeneracy is lifted by a strong anisotropic crystal field so that relevant low-energy excitations can be described by a single band near the Fermi level. Furthermore, the intersite Coulomb repulsion is neglected (except in the so called “extended Hubbard model”, where nearest-neighbour interaction is taken into account).

When both sets of terms H_t and H_U are present, even this simple model has proved to be too difficult for exact analysis. An exact solution for this problem could only be found in one dimension by Lieb and Wu in 1968 [32] and yields an insulating ground state that orders antiferromagnetically for $U \neq 0$.

Due to the lack of analytic solutions for higher dimensions approximations are needed to be able to treat them. In several trials Hubbard tried to solve the Hamiltonian proposed by him and finally was able to reproduce a MIT for a non zero value of U [29]. Two sketches of this so called Hubbard approximation III are given in Fig. 2.3 and 2.4. In the first example, Fig. 2.3, departing from a localized electron with zero kinetic energy the two single and the double occupied states are energetically separated by the Coulomb repulsion energy U. With increasing kinetic energy the localized states become broader and broader and smear out transforming into electronic bands, which finally overlap at a certain finite ratio

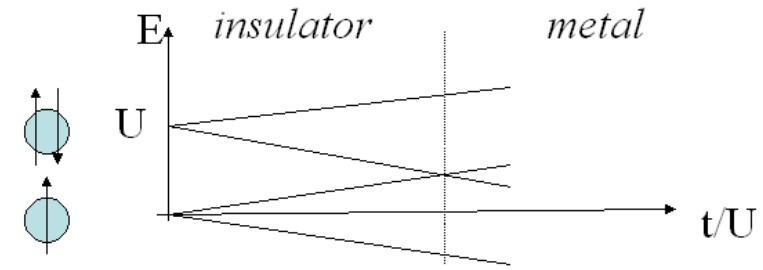

Figure 2.3: Schematic view of the evolution of the band structure of the Hubbard model within the Hubbard approximation.

t/U. In contrast to Mott's argumentation the progressive closure of the gap results in a continuous transition. The second figure 2.4 shows the density of states near

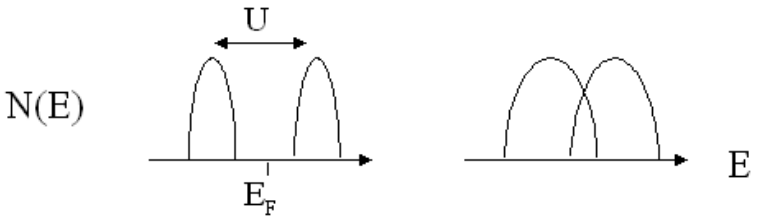

Figure 2.4: Density of states at E_F as a function of the Coulomb repulsion within the Hubbard approximation [28, 29].

the Fermi level for the two limits. For large U the band is split in the so-called lower and upper Hubbard band whilst for small U it merges to a single band in the metallic phase.
Despite these simplifications the Hubbard approximation III is nevertheless capable of reproducing the Mott insulating phase with basically correct spin correlations and the transition between Mott insulators and metals, but a metal-insulator transition only takes place for a band close to half filling. While the insulating phase is reasonably described, Hubbard was not able to implement correctly the characteristics of the metallic phase near the Mott insulator as, for example, the Fermi liquid quasiparticles are absent [33].
In order to understand this mass enhancement this approximation was re-examined by Brinkman and Rice [34] and treated with the Gutzwiller approximation [35]. Using this approach the energy of the ground state is calculated by neglecting spin and charge short ranged correlations with the help of a variational parameter that takes the reduction of the double occupancy with increasing interactions into account. The probability of double occupation vanishes at a critical

value of the interactions U_c where the effective mass $m^\star$ diverges within the Fermi liquid in a continuous manner. An insulating state is established where all sites are occupied singly.
The Gutzwiller approximation, as used by Brinkman and Rice, provides a correct description of the metallic phase, but it gives an incomplete image of the insulator. Further, this variational approach only describes the ground state at zero temperature and the thermodynamics of the transition can not be taken into account.

2.3.3 Dynamical mean-field theory

Because of the absence of an exact solution for the Hubbard Hamiltonian in 2 or 3 dimensions, theoretical predictions in these dimensions are often inexact or contain artefacts of the used approximations. This reflects the presence of different competing physical phenomena. The basic idea of DMFT is to replace a lattice model by a localized single-site quantum impurity problem that is embedded in an effective medium determined self-consistently. This impurity model naturally features a picture of the local dynamics of a quantum system of N bodies. The condition of self-consistence accommodates the translation invariance and coherence effects of the lattice.
This *local impurity self-consistent approximation* is often referred to as *LISA*. The main and capital improvement of Lisa over other static mean-field theories (e.g. Weiss mean-field theory) is that it also neglects all spatial fluctuations, but all local quantum fluctuations are fully taken into account. Because of this LISA is more conveniently characterised as a *Dynamical mean-field theory (DMFT)*.
In analogy to classical mean field theory of phase transitions DMFT becomes exact in the limit of large spatial dimensions $d \rightarrow \infty$ [31], which is proportional to the lattice coordination number, but this approach can be viewed as a starting point for the solution of many problems in finite dimensions, though it is a good approximation for 3-d systems such as V_2O_3 with large coordination numbers.
Some of the most important results obtained with DMFT are presented below.

2.3.3.1 MIT at T = 0

The Hubbard Hamiltonian treated in the framework of DMFT reveals a metal-insulator transition at zero temperature.
In Fig. 2.5 a plot of the local spectral function[2] is shown in addition to the Hubbard bands for different values of U. The displayed results were obtained by using the

[2]The spectral function is interpreted as a probability function and gives the probability that a quasiparticle or electron has the momentum $\underline{p}$ and energy ω. In can be considered as a generalised density of states. The diagonal elements of the spectral function give the local density of states and the trace of the spectral function represents the density of states.

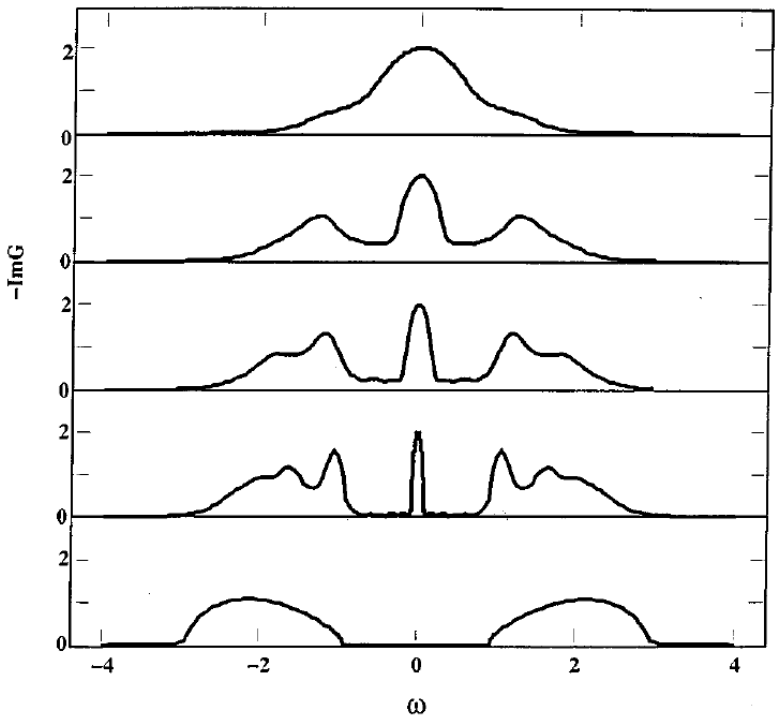

Figure 2.5: Variation of the spectral density at T = 0 for different interaction values. The first four curves (from top to bottom $U/D = 1, 2, 2.5, 3$) correspond to an increasingly correlated metal, while the bottom one ($U/D = 4$) is an insulator [30].

so called iterated perturbation theory (IPT). For small U the function is similar to a bare lattice density of states and for larger values of U a narrow quasi-particle peak is formed at the Fermi level with width ϵ_F^*. This quasi-particle peak is responsible for the Fermi liquid behaviour in the presence of a gap and indeed the system behaves like a Fermi liquid with a Fermi energy in the order of ϵ_F^*. The metallic solution disappears continuously at $T = 0$ until $U/D \approx 2.92$ and we see in the lowest curve ($U/D = 4$) that just two insulating Hubbard bands remain.
In contrast to the Hubbard approximation shown in Fig. 2.4, where metallic behaviour is only possible in the absence of a gap, the local spectral function of Fig. 2.5 proves the possibility of the coexistence of the Hubbard gap and Fermi liquid behaviour.

2.3.3.2 Phase diagram and thermodynamics

Within DMFT both coherent and incoherent excitations are taken into account and this makes DMFT a powerful technique for the study of thermodynamics, in

contrast to earlier methods neglecting the incoherent excitations.
The first order transition occurs when equality between the free energy of the metallic and insulating phase is achieved. This is the case even though no lattice deformations have been included in the model. The curvature of the transition line dT/dU in Fig. 2.6(a) obtained by a fully frustrated model[3] is negative.

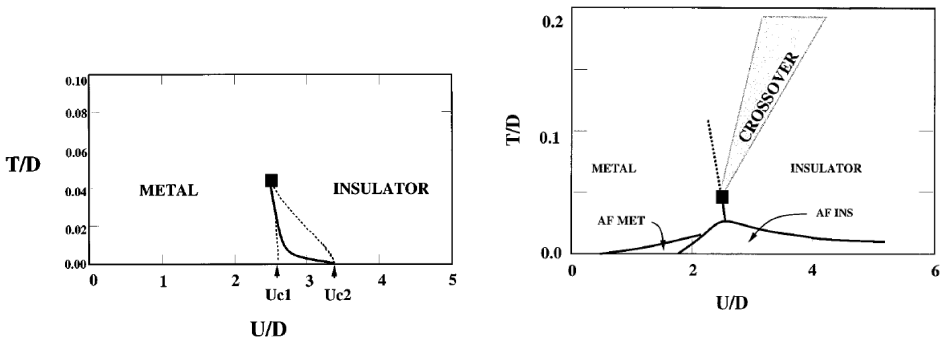

(a) Phase diagram of the fully frustrated model at half-filling [30].

(b) Phase diagram in the nearest- and next-to-nearest-neighbour approximation ($t_2/t_1 = \sqrt{1/3}$ [30].

Figure 2.6: Phase diagrams obtained by DMFT.

In the graph the dotted lines $U_{c1}(T)$ and $U_{c2}(T)$ appear, which correspond to the overlap of the Hubbard bands and the disappearance of the quasi-particle peak. Consequently, the area limited by these two lines is an area of metastability and two solutions are possible of which one is thermodynamically unstable. First order transitions are characterised by a metastable domain and possibly a hysteresis that can theoretically be observed up to the critical point symbolised by a black square in Fig. 2.6. At this critical point the free energies of the metastable phases are equal $U_{c1}(T) = U_{c2}(T) = U_c(T)$ and the metal-insulator transition becomes of second order. For temperatures higher than the critical temperature T_c a crossover is awaited as shown schematically in the second figure of Fig. 2.6(b). The crossover region is on the insulating side limited by the temperature $T \approx \Delta$ and on the metallic side the crossover line is defined at temperatures of the order of the coherence energy of the quasiparticles $T \approx \epsilon_F^*$.

[3]Fully frustrated model refers to the fact that in the originally proposed single-site DMFT beside some other limitations does not capture the effects of the magnetic exchange interaction on the single particle properties in the paramagnetic phase. In order to overcome these deficiencies are within the so called cellular DMFT (CDMFT) the lattice is divided in a superlattice of $x \times x$ squares and the DMFT equations applied to the superlattice and solved [36]. By this CDMFT is capable to produce informations for problems where correlations between more sites and orbitals need to be taken into account.

In Fig. 2.7 the local spectral density at different temperatures is plotted, showing

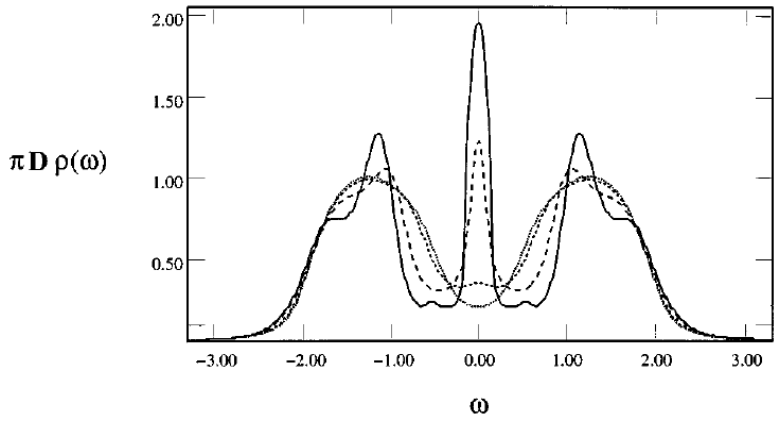

Figure 2.7: Variation of the spectral density at $U/D = 2.5$ for several temperatures ($T/D = 0.03$ full line, $T/D = 0.05$ dashed line, $T/D = 0.08$ short dashed line and $T/D = 0.1$ dotted line) [30].

the evolution of the spectral density in the metallic phase ($U/D = 2.5$). It is worth noting that the quasi particle peak disappears above temperatures of the order of ϵ_F^*. The density of states decreases at the Fermi level. This phenomenon is often called pseudo-gap. By this the appearance of the crossover and the change from a coherent towards an incoherent metal is signalled.

2.3.3.3 Anomaly of the lattice constants

In the results obtained using DMFT shown above in Fig. 2.6 and Fig. 2.7 lattice degrees of freedom were not taken into account at all. But they do play a role at the Mott transition of real materials, as for example the lattice spacing changes discontinuously in Chromium doped V_2O_3. Experimental evidence in organic materials for this was found in ultrasound experiments by Fournier et al. [37, 38] and by Lang et al. [39] and de Souza et al. [40, 41] by observation of the thermal expansion coefficients.
In order to describe this effect the electronic degrees of freedom and the ionic positions have both to be taken into account. Majumdar et al. [1] presented the first approach to include lattice effects in this theoretical framework and treated it in the simplest approximation where all phonon excitations are neglected. They were able to point out that the instability of the compressibility $\kappa < 0$ may be responsible for the first order MIT observed in the transition oxides.
Here we shortly present the point of view developed in two articles by Majumdar and Krishnamurthy [1, 2] who used the local DMFT approach to the half-filled Hubbard model on a compressible lattice.

Starting from the expression of the free energy:

$$F(v) = F_{el}(v) + F_{lat}(v), \tag{2.2}$$

which is the sum of the electronic free energy F_{el} and a contribution of the lattice F_{lat}. Both quantities depend on the volume. The overall stiffness (i.e. the inverse compressibility per cell volume) of the system, defined by $\kappa = -\frac{v\partial P}{\partial v}$ and $P = -\frac{\partial F}{\partial v}$ is given by:

$$\kappa_{tot} = v\frac{\partial^2 F}{\partial v^2} = \kappa_{el} + \kappa_{lat}, \tag{2.3}$$

where κ_{el} is negative and divergent near T_c^{el}, U_c^{el}. κ_{lat} is a positive contribution to κ_{tot} arising from the volume dependence of the site energies of the core electrons and from the ions.
A system is only stable as long as $\kappa_{tot} \geq 0$ and the critical point (U_c, T_c) is defined by $\kappa_{tot} = 0$, where the compressibility of the (electron + lattice) system diverges and the two contributions to the overall stiffness nullify each other. At this point a first order MIT accompanied by a discontinuous volume change occurs to avoid the unphysical region where $\kappa_{tot} < 0$. It is important to note that the critical temperature T_c where the system transits differs from the temperature T_c^{el} where κ_{el} diverges.
One of the goals of this thesis is to observe the different temperatures and to estimate experimentally the difference of these two temperatures $\Delta T = |T_c - T_c^{el}|$.

2.3.3.4 The speed of sound in the case of V_2O_3

Following this Hassan et al. [3] were able to make some remarkable predictions for the sound velocity at the metal-insulator transition for V_2O_3 and the organic conductor $BEDT$ using DMFT. Hassan et al. compared their findings for $BEDT$ to the results of Fournier et al. [37] and found the overall shape of their curves, as well as the order of magnitude of the effect in good agreement to the experimental data. One of the inspirations of this work was to test these predictions for V_2O_3 and to compare them with experiments in this compound.
Within the DMFT electronic degrees of freedom are the driving force of the Mott transition and the critical endpoint is associated with a diverging electronic response function χ_{el} (defined below), in analogy with the liquid-gas transition. But in real materials lattice degrees of freedom also play a role at the Mott transition, as it is to be expected because in a metal the itinerant electrons participate more in the cohesion of the solid than they do in an insulator. This results in a discontinuous increase of the lattice spacings at the first order transition as observed by A. Jayaraman et al. [42] for $(V_{1-x}\ Cr_x)_2O_3$. Hassan et al. proposed a qualitative theory connecting the lattice effects to the behaviour of the speed of sound at

the transition. As a starting point they used a compressible Hubbard model introduced by Majumdar et al. in Ref. [1], which allows treatment of the electronic and lattice degrees of freedom.
It is assumed that the free energy depends on the unit-cell volume in the following manner:

$$F = F_0 - P_0(v - v_0) + \frac{1}{2}B_0\frac{(v - v_0)^2}{v_0} + F_{el}\left[D(v)\right], \tag{2.4}$$

where the last term F_{el} is due to the contribution of the electronic degrees of freedom that are active through the transition (e.g. the d shell) and the first three terms come from other degrees of freedom when the system is parting from the reference unit cell volume v_0, reference pressure P_0 and the reference bulk elastic modulus B_0. $D(v)$ is the half-bandwidth depending on the unit cell volume.
For small relative changes in v a linearised exponential parametrization for $D(v)$ allows the pressure $P = -\partial F/\partial v$ to be written as:

$$P = P_0 - B_0\frac{(v - v_0)}{v_0} - \frac{\gamma D_0}{v_0}\tau_{el}, \tag{2.5}$$

using τ_{el} as the dimensionless kinetic energy $\tau_{el}\left((T, D(v), U\right) \equiv \partial F_{el}/\partial D$ and the compressibility $K \equiv -\left(v\partial P/\partial v\right)^{-1} = \left(v\partial^2 F/\partial v^2\right)^{-1}$ is given by:

$$(Kv)^{-1} = \frac{B_0}{v_0} - \left(\frac{\gamma D_0}{v_0}\right)^2 \chi_{el}. \tag{2.6}$$

Here the electronic response function is $\chi_{el}\left((T, D(v), U\right) \equiv -\partial^2 F_{el}/\partial D^2$.
In [1] it is shown that, within the compressible Hubbard model, K diverges at T_C and because the inverse compressibility K^{-1} is directly proportional to the square of the sound velocity s, $s \propto 1/\sqrt{K}$, it follows from a diverging K at T_C that s will vanish. Thus, from a calculation of the inverse compressibility the dependence of the speed of sound on temperature and pressure can be determined.
For the actual calculation the following values were used: $D_0 = 1\ eV$ for the initial half-bandwidth, $B_0 = 2140\ kbar$ as the reference value for the elastic bulk modulus, $v_0 = 100$ Å^3 for the initial unit cell volume, $\gamma = 3$, $B_0 v_0 = 133\ eV$, $U/D_0 = 2.468$ and finally $B_0 v_0/(\gamma^2 D_0) = 14.7$. The value U/D_0 is hereby adjusted to reproduce the critical pressure correctly to $P_c \approx -4\ kbar$ in pure V_2O_3. The high value for the dimensionless combination $B_0 v_0/(\gamma^2 D_0)$ implies that the Mott transition emerges due to large values of $D_0\chi_{el}$, which means the experimentally observed transition for V_2O_3 is very close to the purely electronic Mott transition and solely driven by the electronic degrees of freedom. This point will be studied experimentally within this work.
In Fig. 2.8 the predictions for the temperature dependence of the sound velocity are shown. From equation 2.6 follows that very close to T_c, where χ_{el} can be

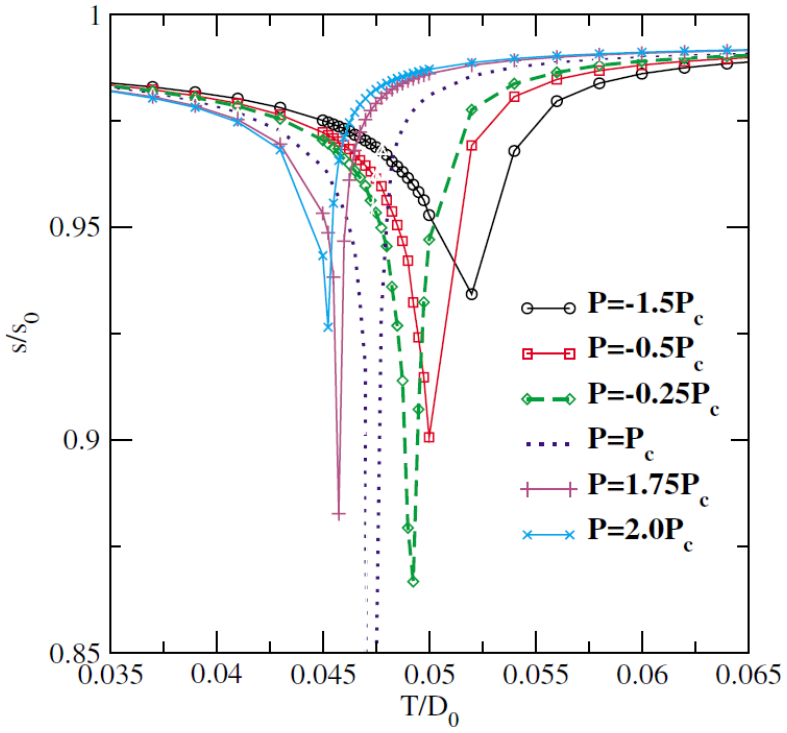

Figure 2.8: Prediction for the temperature dependence of the sound velocity at various pressures for parameters corresponding to pure V_2O_3 [3]. The negative pressure can be reached by doping with chromium (see chapter 3).

approximated by a linear function, the speed of sound s vanishes according to the mean field law

$$s \propto (T - T_c)^{1/2}\,, \tag{2.7}$$

at the critical pressure $P = P_c$. K diverges as $1/(T - T_c)$ and a prominent dip remains visible over a rather big pressure range above and below P_c. The relative size $\Delta s/s \approx 15\%$ at P_c is very big. In reality s will be sensitive to details of the variation of χ_{el} and the regime where Eq. 2.7 is valid will not be attained.
In Fig. 2.9 the sound velocity is plotted as a function of pressure for several different temperatures. At the critical temperature T_c the speed of sound vanishes again and the different curves show a striking asymmetry: on the insulating (low pressure) side the pressure dependence is weaker and the dip appears only very close to P_c, while the metallic (high pressure) side shows a much stronger dependence on the pressure. This reflects the asymmetry in the electronic response function χ_{el} and represents qualitatively that the electrons contribute less to the cohesive energy on the insulating side. According to this calculation the anomaly in the sound velocity is largest along a crossover line that continues smoothly the first

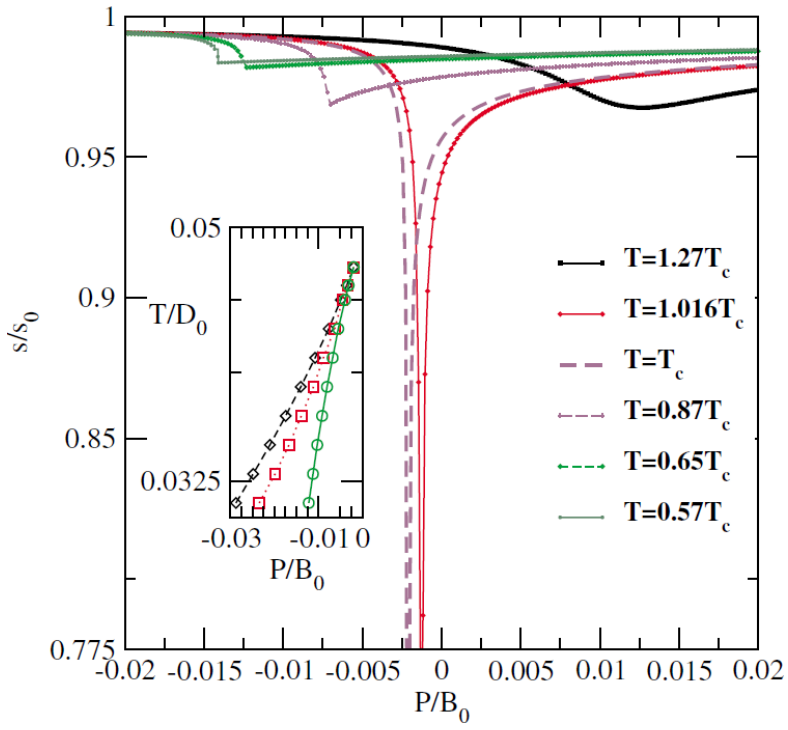

Figure 2.9: Prediction for the sound velocity as a function of pressure at several fixed temperatures for parameters corresponding to pure V_2O_3. Inset: the corresponding phase diagram. The central line and the line on either side correspond to the transition pressure P_{tr} and the spinodal pressure, respectively [3].

order transition line for $T > T_c$. The relative size $\Delta s/s \approx 20\%$ at P_c is also rather large.

According to Hassan it is to be expected that screening effects would reduce (enhance) the effective Hubbard U and analogously enhance (reduce) τ in the metallic (insulating) phase. Hence, this would result in an overall enhancement of $(v_i - v_m)/v_0$. Another enhancement factor might arise from the orbital degeneracy in V_2O_3.

Chapter 3

Presentation of the investigated system

Since the discovery of Vanadium sesquioxide (V_2O_3) it has been intensively studied, both experimentally and theoretically, because it is a prime example for observing a metal-insulator transition [43, 44].
Even preceding Mott's theory, in 1946 a first order metal-insulator transition was observed for the first time by M. Foex [45] when cooling V_2O_3 to temperatures below 160K.
But not only pure V_2O_3 is of special interest; for a long time also compounds derived from Vanadium sesquioxide $(V_{1-x}\ M_x)_2O_3$, where the Vanadium is substituted by another $3d$ transition metal M (Cr, Ti, ...) in order to cause variations in the lattice parameters, came early to the centre of attention. These compounds were already extensively studied in the early seventies by McWhan et al., who published a remarkable series of articles on this topic [46, 47, 11, 48].
In the following paragraph a closer look at the phase diagram, the crystal structure and the effects of doping of V_2O_3 on the crystal structure will be taken.

3.1 Phase diagram of V_2O_3

After several measurements on pure and Cr and Ti doped samples, which are shown in Fig. 3.1, a detailed phase diagram of V_2O_3 could already be established in the early seventies [11, 48]. In fig. 3.2 it is shown as a function of temperature and pressure.
The pressure influencing the phase transitions can be of two different natures, external (hydrostatic pressure applied) or internal (chemical) pressure. The effect of the chemical pressure can for example be established by the substitution of vanadium V^{3+} ($3d^2$, ionic radius r_i= 0.64 Å) by another transition metal such as

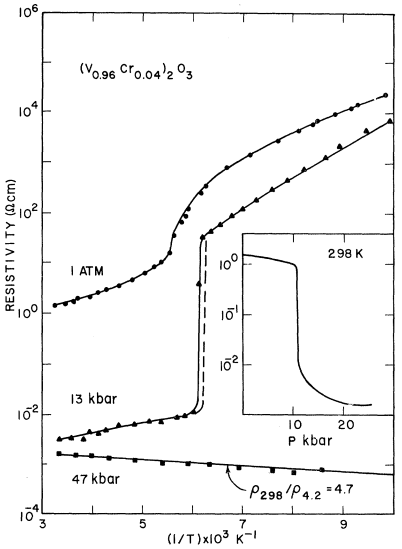

(a) Resistivity against reciprocal temperature for $(V_{0.96}\ Cr_{0.04})_2O_3$ [46].

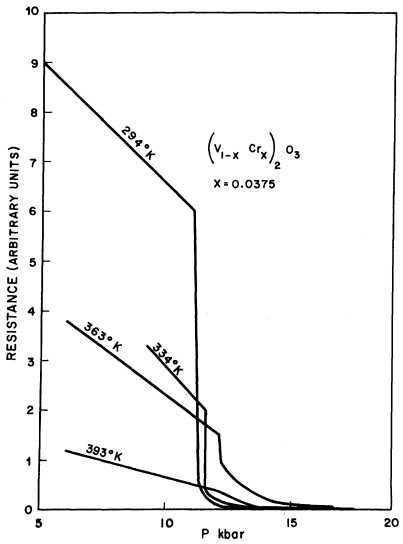

(b) Resistivity versus pressure for Cr doped V_2O_3 [42].

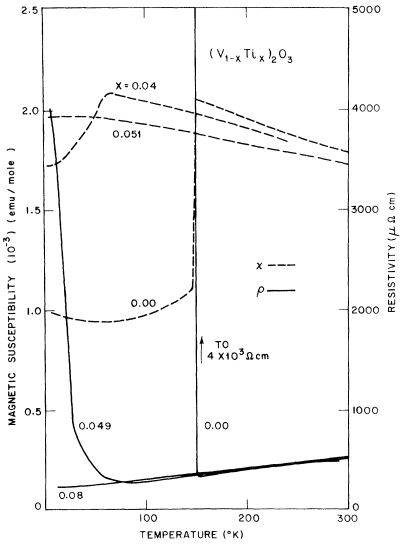

(c) Susceptibility (dashed curves) and resistivity (solid curves) for V_2O_3 and several Ti doped samples as a function of temperature [11].

Figure 3.1: The Figures (a) and (b) show different resistivity measurement on V_2O_3 samples doped with different amounts of Cr. Figure (c) shows susceptibility and resistivity measurements of pure V_2O_3 and several Ti doped samples.

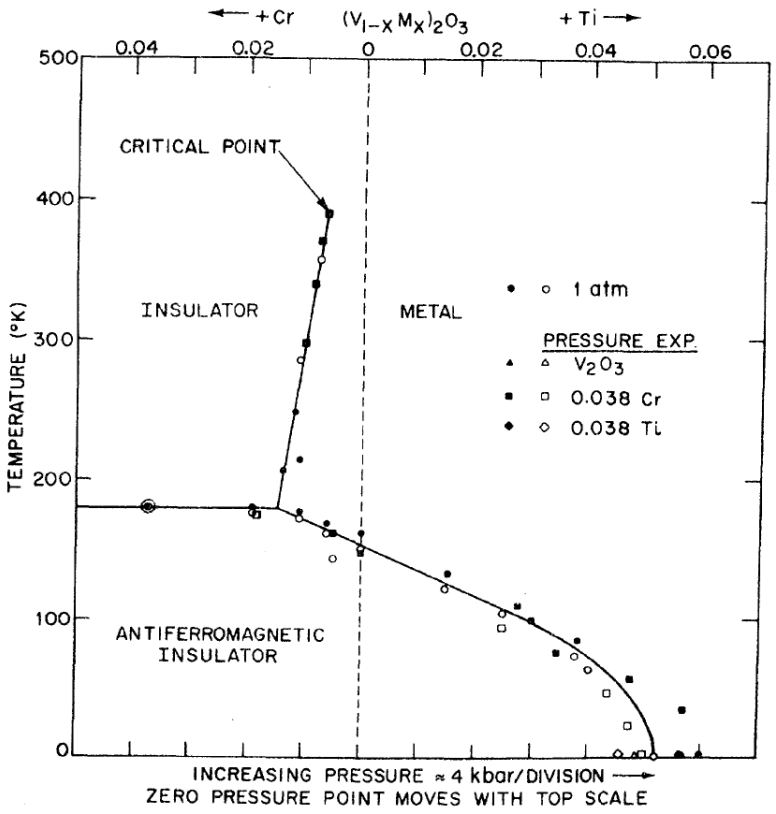

Figure 3.2: Generalized phase diagram of V_2O_3 showing the metal-insulator transition as a function of hydrostatic pressure and as a function of doping with Cr or Ti. The first order metal-insulator transition terminates at a critical point [48].

chrome Cr^{3+} ($3d^3$, r_i= 0.615 Å) or titanium Ti^{3+} ($3d^1$, r_i= 0.67 Å) and an empirical scaling was found between the addition of Cr^{3+} or Ti^{3+} and the application of hydrostatic pressure (1% of doping ≈ 4kbar of negative or respectively positive hydrostatic pressure). Analogous to the effect of doping with Ti, nonstoichiometry (V_2O_{3+x}) also has the same effect as positive pressure [49]. Nonstoichiometry (V_2O_{3+x}) creates V^{4+} ($3d^1$, r_i= 0.58 Å) ions to maintain electric neutrality in the sample. The departure from stoichiometry is obtained by a partial occupancy of the metal sites and is therefore caused by metal deficiency [50], whilst the oxygen sites are fully occupied.

In the phase diagram there are three different regions that can be easily identified. Pure V_2O_3 (in figure 3.2 represented by the line at x = 0) is at room temperature in a paramagnetic metallic (PM) state and has a rhombohedral symmetry [51]. When the temperature is lowered below approximately 160K a first order metal-insulator transition takes place where the sample orders magnetically [52, 53],

to be exact antiferromagnetically, and becomes insulating. This phase transition is accompanied by a change in the structure from rhombohedral to monoclinic [54, 55] and it shows a large hysteresis in temperature in either cooling or heating. With increasing applied hydrostatic pressure the transition temperature decreases and is totally suppressed by the application of pressures higher than 26 kbar [56, 57].

Already the addition of small amounts of chromium to pure V_2O_3 has a dramatic effect on the electrical properties [46, 42] and leads to the formation of a new insulating phase that does not exist in the pure compound. The transition from the PM to the paramagnetic insulating (PI) phase is also of first order and the temperature for the transition depends on the Cr concentration. At room temperature the transition in $(V_{1-x}\ Cr_x)_2O_3$ occurs near x=0.01 [58] and for higher Cr concentrations the system is in the PI state. To cross the transition hydrostatic pressure has to be applied. The PM-PI transition shifts to higher pressures with increasing Cr concentration and the high pressure is equivalent to decreasing doping (doping with Cr $\approx$ negative pressure). The transition line finally terminates in a critical point [42] at which the transition becomes of second order [58]. For not too high percentages of Cr (up to x $\approx$ 30%) the PI-AFI transition is nearly unaffected by doping with Chromium and the transition temperature remains between 150 and 180 K [59].

Doping with some other transition metal oxides such as Ti [60] or Mg stabilizes the PM phase, as does oxygen excess [61, 49]. Here a decrease in the PM-AFI transition temperature is induced with increasing x and for high x the transition is totally suppressed. This is in total analogy with applied hydrostatic pressure.

This work will be about both pure V_2O_3 and doped $(V_{0.989}\ Cr_{0.011})_2O_3$ in the temperature region from room temperature up to around 500K to investigate the transition from the PI to the PM phase. Thus, the AFI phase can be left aside for the rest of this work.

In a preceding work by P. Limelette [4] a series of resistivity measurements were carried out (see Fig. 3.3) and a detailed, more recent phase diagram for the sample system $(V_{0.989}\ Cr_{0.011})_2O_3$ in dependence of temperature and hydrostatic pressure could be established for the regions of pressure and temperature that will also be investigated in this thesis (Fig. 3.4).

In this diagram it is easy to identify the large region of coexistence of the metallic and the insulating phases and the large hysteresis for pressure dependent scanning below the critical point, which is designated for this compound at $T_c \approx 457.5K$ and $P_c \approx 3738bar$, where the first order transition becomes second order. In this phase of coexistence both phases can exist depending on commencing from the metallic or insulating side of the transition. For isothermal pressure cycles the area of coexistence broadens with decreasing temperature coming from T_c.

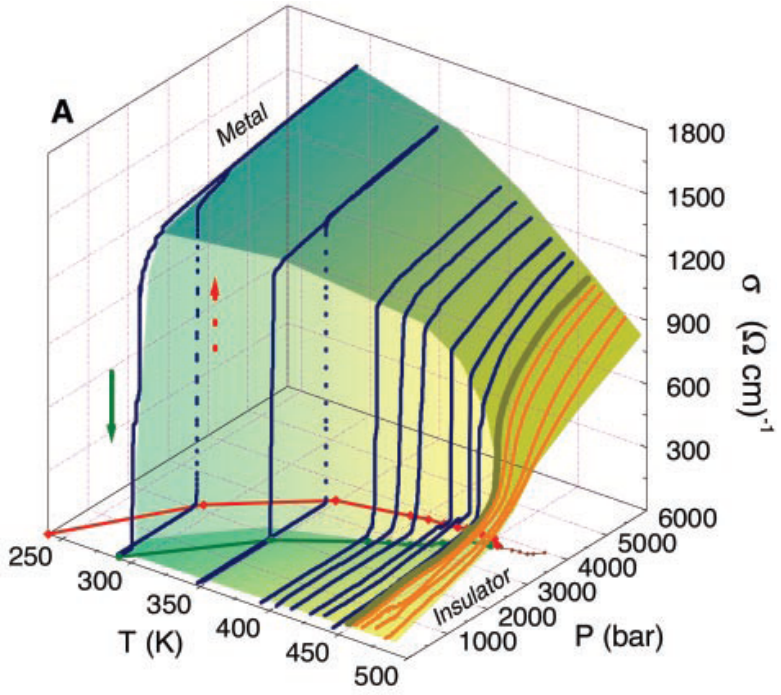

Figure 3.3: Conductivity as a function of pressure, for temperatures ranging from T = 485 K (> Tc = 457.5 K, orange curves) down to T = 290 K (< Tc, blue curves). The dark yellow curve represents the conductivity at Tc. Examples of a hysteresis cycle are shown for T = 290 K and T = 348 K. Arrows indicate direction of pressure sweeps [5].

3.2 The crystal structure

Pure V_2O_3 and also V_2O_3 doped with 1.1% Chromium exist at room temperature in an isostructural phase to corrundum, $\alpha - Al_2O_3$, which posesses rhombohedral symmetry. The rhombohedral (or trigonal) crystal system is named after the two-dimensional rhombus and the crystal is described by vectors of equal length $a = b = c$, of which all three are not mutually orthogonal with angles $\alpha = \beta = \gamma \neq 90°$. The rhombohedral system can be thought of as the cubic system stretched diagonally along a body. To be more exact the appropriate space group for corundum is $R\bar{3}c$, named rhombohedral holohedral.
The oxygen ions are in the form of a close-packed hexagonal lattice (2H), with a sub-lattice composed of octahedral interstitial sites that are two-thirds occupied by V atoms. The distribution of the vacant sites has thereby threefold symmetry. In some classification schemes, the rhombohedral system is grouped into a larger hexagonal system and the lattice parameters of V_2O_3 based on hexagonal indexing are $a = 4.9492$ and $c = 13.998$Å[62].

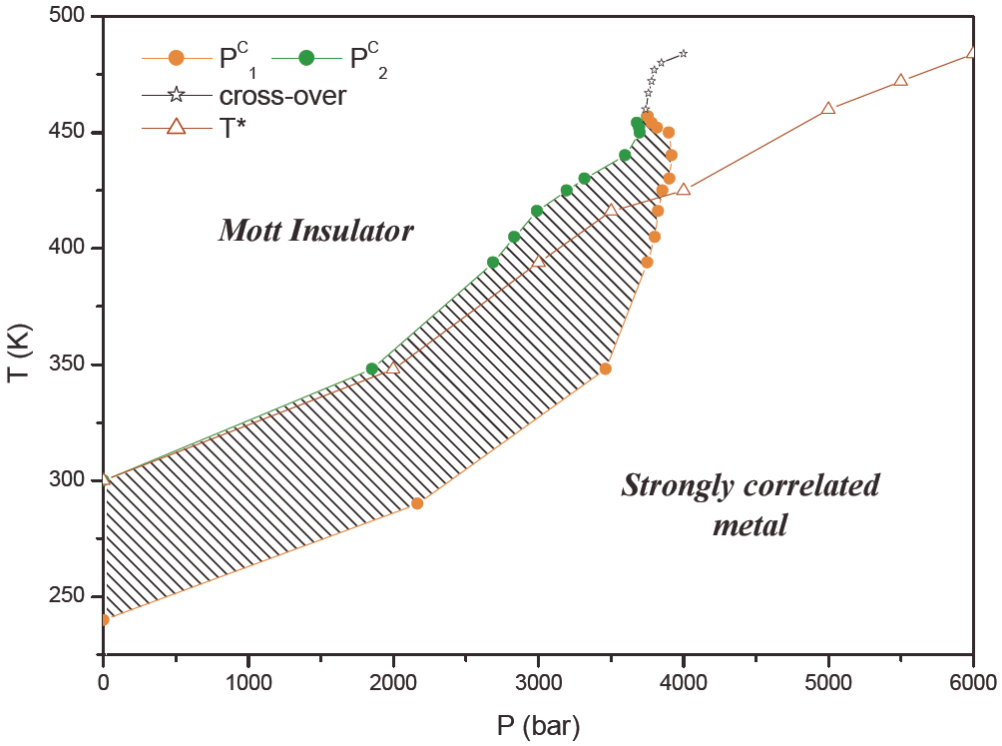

Figure 3.4: Phase diagram of $(V_{0.989}\ Cr_{0.011})_2O_3$ in dependence of temperature and pressure. The two lines P_1^c and P_2^C correspond respectively to the borders of the metastable regions of the insulating and the metallic phase, and delimitate the region of coexistence of the two phases that is drawn shaded. P_1^c and P_2^C merge at the critical point (T_c, P_c), with $T_c \approx 457.5K$ and $P_c \approx 3738bar$ to continue as a cross-over line (indicated with a *) which is defined as the maximum of the resistivity as function of temperature [4]. Here the line T^* represents a cross-over between Fermi-liquid and bad metal.

The positions of the Vanadium atoms in both the primitive trigonal and the hexagonal cell are illustrated on the left side in Figure 3.5. On the right side the corun-

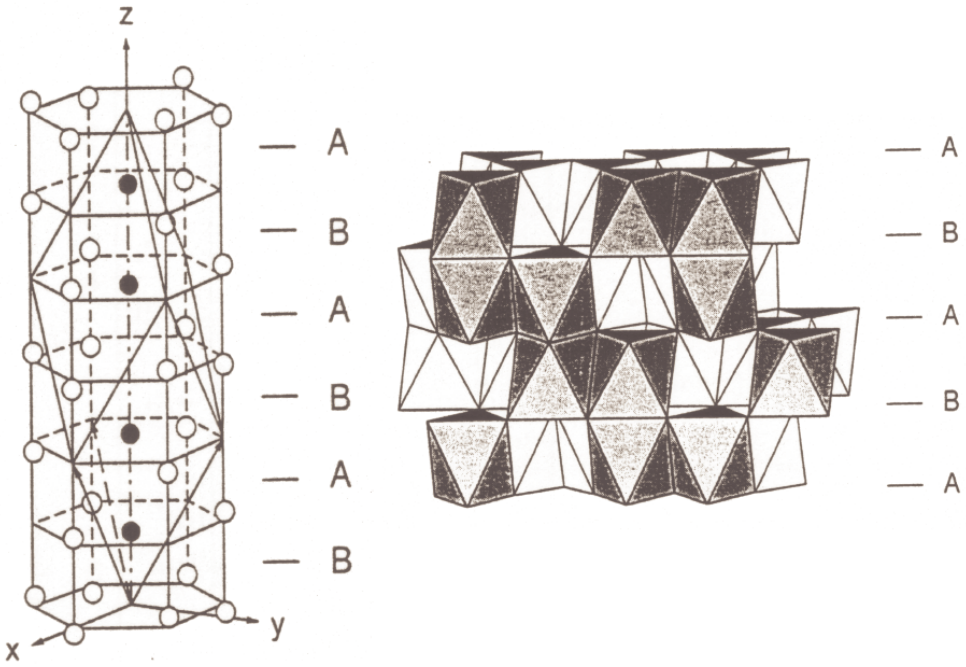

Figure 3.5: On the left: Positions of the Vanadium atoms for V_2O_3 in the corundum phase. The filled circles indicate the positions of the V atoms in the primitive trigonal cell and the positions in the non primitive hexagonal cell are also indicated (filled and non filled circles). On the right: The corundum structure build by VO_6 octahedra with NiAs-type vacancies [63].

dum structure is composed of VO_6 octahedra with ordered NiAs-like vacancies [63].

3.3 The effect of doping on the crystal structure

For this work it is important to note how the crystal structure of V_2O_3 evolves with different dopings and different concentrations of doping. Hence in graph 3.6 the effects of doping the V_2O_3 host lattice with small percentages of Ti or Cr is shown.
In spite of the fact that Ti^{3+} is larger and Cr^{3+} is smaller than V^{3+}, the atomic movements caused by doping up to 1.25% of Cr (the limit for having Cr doped V_2O_3 in the metallic phase at room temperature) or up to 5.5% of Ti are in the same direction. As Cr^{3+} is smaller it produces and ineffective orbital overlap

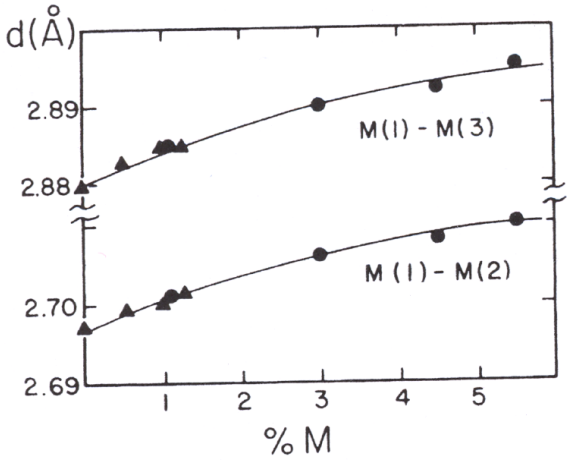

Figure 3.6: Variation of metal-metal distance with percentage of dopant. The solid circles represent Ti doped V_2O_3 and the triangles Cr doped V_2O_3 [64].

when replacing V^{3+} and thereby causes the removal of bonding states in the host lattice, bonding electrons are removed and the metal-metal distances increase. In addition by the removal of these states the bands are narrowed.
On the other hand addition of the larger Ti^{3+}, which is a d^1 ion while V^{3+} is a d^2 ion, also results in a decrease in the number of valence electrons in the band and an increase in the metal-metal distances. From the comparison of these structural variations Chen et al. [64] concluded that the change from metallic to insulating behaviour cannot be a structure effect.
In summary, different X-ray studies[1] [65, 62, 66] confirm that the PM-phase of $(V_{0.99}\,Cr_{0.01})_2O_3$ is isostructural to pure V_2O_3 and the PI-phase of $(V_{0.99}\,Cr_{0.01})_2O_3$ is isostructural to $(V_{0.962}\,Cr_{0.038})_2O_3$ (all at room temperature) and these two are very close to pure V_2O_3 at 600°C.

[1]Two tables giving interatomic distances and bond angles can be found in Appendix A

Chapter 4

The employed experimental techniques

Within this chapter the principle experimental techniques employed in this work will be presented. Starting from the preparation of the samples in the next part the fundamental technique of the presented studies: the high pressure facility will be introduced. Further the set-ups of the two used experimental approaches will be briefly described before finally a short test of the correct chemical composition of the sample will be presented.

4.1 Sample preparation

The samples of pure V_2O_3 and V_2O_3 doped with 1.1%Cr single crystals used in this work were grown using the skull-melter technique [67] followed by appropriate annealing by P. Metcalf of Purdue University [1].
In the first step the single crystals are oriented with an apparatus for X-ray diffraction using the Laue method. After this the samples for the different experimental techniques had to be treated unequally.
The samples used for the experiment to determine the speed of sound were, after being oriented along the desired crystal axis, cut perpendicular to this axis with a diamond wire saw to a thickness of between 2-3 mm. Then, to achieve perfectly parallel planes on both sides of the sample, it is consecutively polished with sand paper of smaller grain thicknesses until arriving at a grain thickness of 1 μm. In the next step a thin chromium bonding layer and a gold layer were deposited on one of the two polished sides of the sample onto which a piezoelectric ZnO transducer

[1] Metcalf, P., Department of Chemistry, Purdue University, West Lafayette, Indiana 47907, USA

was sputtered [2]. The thickness of ZnO film was chosen in a way that the half wavelength corresponded to a resonance frequency of circa 200 MHz. The very broad resonance allows the excitation of sound waves in the range of 100MHz - 500MHz in the sample. Finally from the big batch smaller units, suitable for the pressure cell, were cut with a diamond wire saw into rectangular pieces of an approximate size of 2 mm $\times$ 2 mm.
The samples used to evaluate the thermoelectric power did not require any special treatment. After being oriented they were just cut into bars along the desired axis of a typical length of 5 mm and cross-section of 1 mm $\times$ 0.2 mm.

4.2 The high pressure facility

The properties of strongly correlated electron systems such as V_2O_3 depend fundamentally on the density of states (and thus on the bandwidth) especially near the Fermi-Level. Hence a change in the inter-atomic spacing may result in enormous variations of the physical properties of these systems. Undoubtedly pressure increases the bandwidth and because in a first approximation hydrostatic pressure reduces the inter-atomic distances linearly, increasing pressure is a perfectly adapted method to investigate these systems.
The measurements in the pressure cell were either performed at different fixed temperatures between 290 K and 493 K, while the pressure was changed slowly or the temperature was changed slowly at constant pressures. The temperature was thereby controlled by a temperature controller manufactured by Lakeshore [68], which allowed the temperature to be kept constant or varied steadily with rates down to 0.1 K/min. To apply pressure we employed a liquid pressure system with Isopentane being used as the pressure liquid. A schematic drawing of our set-up can be found in Fig. 4.1. With the help of a hydro-pneumatic pump a pressure up to 400 bar is created in the pressure accumulator. Afterwards a jack with a diameter of ($\varnothing$ = 140mm) pushes with the pressure coming from the accumulator onto a plunger ($\varnothing$ = 16.1 mm) and introduces the isopentane into the pot of the press, which is connected via a copper beryllium capillary with the inner sample space of the pressure cell ($\varnothing$ = 6.5mm and length = 13.5mm). The pressure cell is made of maraging steel and can, in order to study different regions of temperature, either be placed inside a cryostat or, as for our experiments, be heated with the help of a heater inside the cell.
The valves A and B control whether the pressure is increased or decreased (to increase pressure: A = u and B = s, to decrease: A = s and B = u; with s for screw and u for unscrew). The valves H, E, I control the ratio with which the

[2] Institut des NanoSciences de Paris (INSP), UPMC (Paris VI), Paris, France

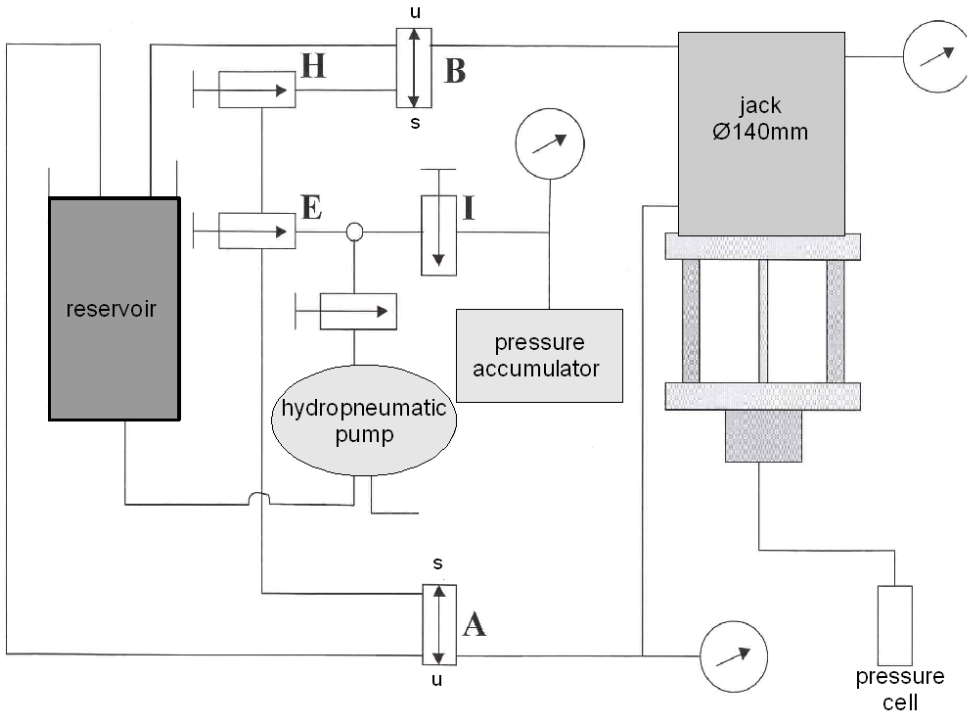

Figure 4.1: Schematic of the pressure system used to perform the experiments.

pressure from the accumulator is applied to the jack and therefore the variation of the pressure in the cell. Through this system the pressure can be altered very slowly and exactly down to a variation rate of only 5bar per minute.

The pressure applied in the cell (according to Pascal's law) corresponds here to the one at the jack multiplied by the ratio of the jack/plunger surfaces. For the presented work pressures up to 6kbar were used.

The actual pressure is measured at the bottom of the pot of the press with the resistance of a manganin wire. Placing the manganin wire in the pot of the press which stays at room temperature avoids any influences of temperature changes on the measured resistance. Thereby the sensitivity of the change of the resistance is given by:

$$S = \frac{1}{R}\frac{\Delta R}{\Delta P} = 2.4810^{-3} kbar^{-1}.$$

With this and a high resolution multimeter it is possible to detect variations of the pressure in the order of 1 bar with a resistance in the order of magnitude of 1 kΩ.

4.3 The speed of sound experiment

4.3.1 The experimental set-up

A schematic drawing of the facility used to perform the sound speed measurements in the described pressure cell is given in Fig. 4.2. A synthesizer creates

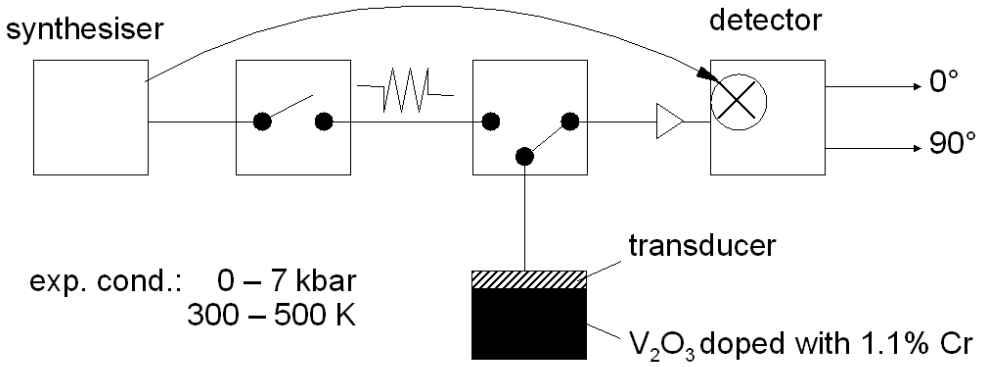

Figure 4.2: Schematic of the experimental set-up to perform the sound speed experiment.

an electrical AC signal of a tunable frequency in the range of 100 - 500 MHz, which is transmitted to the sample via several switches in the form of a rectangular pulse. This pulse excites, with the help of a piezoelectric transducer (for our experiment ZnO is used), a mechanical sound wave in the sample. For this two gold wires are attached on top of the transducer and on the ground electrode using high temperature silver paint [69]. Afterwards, the different reflections at the ends of the sample are partly transmitted to a detector via several switches where they are phase sensitively detected, displayed on the oscilloscope [70] and afterwards stored for further processing.

4.3.2 The acquired signal

An example of the calculated amplitude of the acquired signal, as displayed on the oscilloscope, containing the pulse and several echoes at a fixed temperature (493 K) and different pressures varying between 750 bar and 4150 bar can be found in Fig. 4.3. The time window for the acquired signal is 10 μs that starts when the pulse is sent. So naturally the first thing visible in the graph is the pulse followed by approximately a dozen echoes that become continuously smaller. In order to maintain a reasonable signal to noise ratio it is convincing not to use all the echoes for analysis, but to limit ourselves to the first five to six echoes. It is easy to see

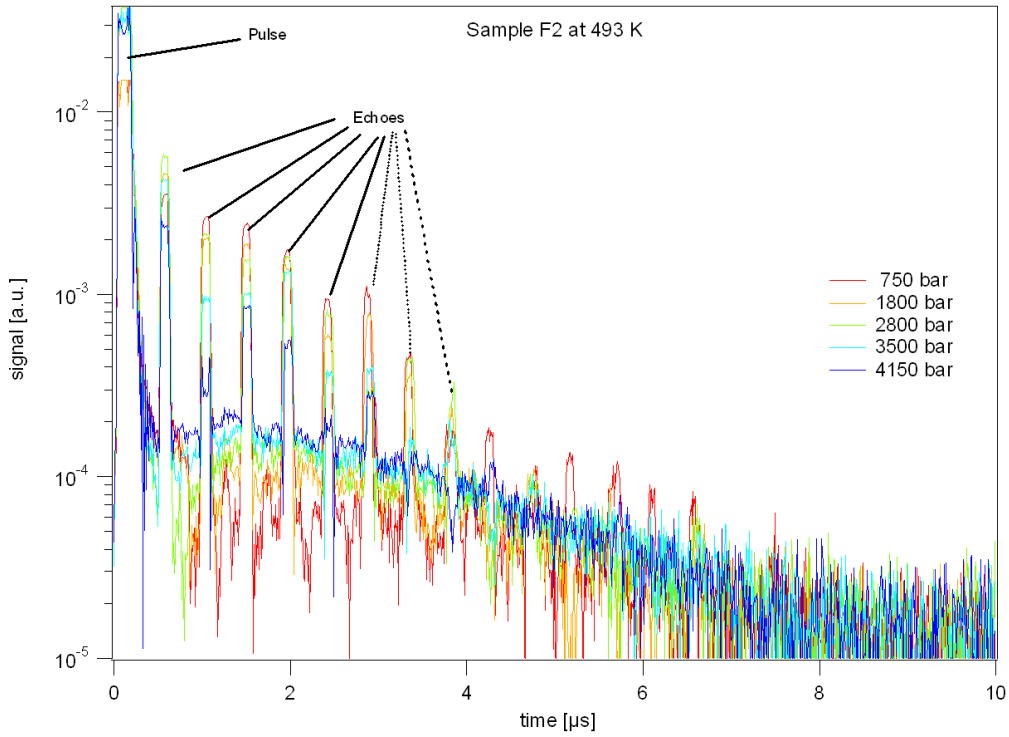

Figure 4.3: The amplitude of the signal of the two detected channels of the ultrasound experiment. After the sent pulse the spaced echoes are detected by the acoustic spectrometer.

that the signal becomes smaller with increasing pressure. One reason for this is that the density of the pressure liquid at higher pressures becomes nearer to the one of V_2O_3, resulting in higher transmission losses of the mechanical signal to the pressure liquid.
In the next step the relative phase change is calculated from the change between the echoes of different acquisitions. This is in contrast to the majority of ultrasound experiments where usually the phase of the echoes is used directly, but the condition for this is a constant phase shift in the electronics, which is not fulfilled in our experiment due to our continuous pressure sweeps.

4.3.3 The principle of the measurement

The first principle of interferometric spectroscopy is the analysis of the phase shift between the electrical reference signal $S_{ref} \propto e^{i(-\omega t)}$ used to generate the sound waves that are sent through the sample and the one of the first echoes $S_{ech} \propto e^{i(kx-\omega t)}$ detected after being reflected at the other end of the sample. Thereby the

length travelled x is given as $x = 2l$, where l is the length of the sample. The phase difference between the two signals can be expressed as:

$$\frac{\Delta\varphi}{\varphi} = \frac{\Delta l}{l} - \frac{\Delta v}{v}. \tag{4.1}$$

In the majority of cases the variation of the thermal expansion constants is two orders of magnitude smaller than the variation of the sound speed and for this the right term can be neglected. But it is still necessary to verify this before continuing with this simplification. In the following the maximal change in the sound speed due to dilatation at the transition will be estimated.
The change of the dimension of the hexagonal c-axis for the $PM \rightarrow PI$ transformation in $(V_{0.99}\ Cr_{0.01})_2O_3$ at $23°C$ is, according to Robinson [62], $\Delta c/c = -0.0043$ and therewith decreasing by less than 0.5%. In our experiment the transition will be crossed at higher temperatures near the critical temperature. We expect that Δc decreases like the jump in the order parameter and because of this the change of dimension will be clearly much less than 0.5% and the maximal effect of the dilatation of the sample at the transition can be estimated as 0.5%.
Keeping this in mind this allows us to neglect the relative change of the length $\frac{\Delta l}{l}$ and leads to this relation:

$$\frac{\Delta\varphi}{\varphi} = -\frac{\Delta v}{v}. \tag{4.2}$$

Using this we are able, after dividing the measured change in the phase by the total phase $\varphi = \frac{4\pi f l}{v}$, to give the relative change in the speed of a sound wave with frequency f for the different experiments. Hereby applies $\frac{2l}{v} = t$, where t represents the time needed by a wave of a certain speed to travel two times through a sample of length l, which corresponds to the time between two echoes. This leads to the following expression for the relative change of the sound speed during an experiment:

$$\frac{\Delta v}{v} = \frac{\Delta\varphi}{360° f t}, \tag{4.3}$$

and this allows comparison between different experiments.

4.4 Measurement of the thermoelectric power

4.4.1 The experimental set-up

This experiment was carried out in the same pressure cell as described above. Thus, the measurements took place in the same range of temperature and pressure. As the absolute value of the Seebeck coefficient is defined as

$$S = \Delta V/\Delta T, \tag{4.4}$$

it is crucial to determine the temperature gradient across the sample, ΔT, and the resulting voltage difference ΔV in order to estimate the thermoelectric power.
A rough sketch of the experiment used to do this is shown in Fig. 4.4. The rect-

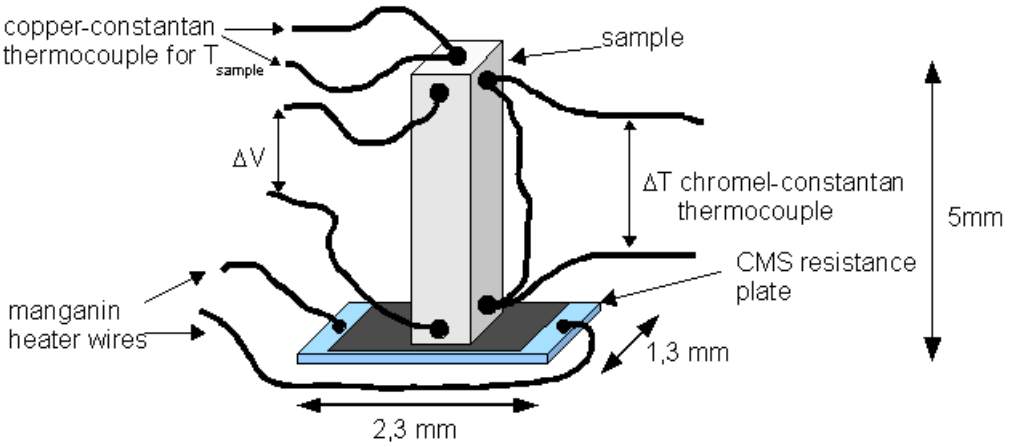

Figure 4.4: Scheme of the experiment used for measurements of the thermoelectric power and thermal conductivity.

angular sample with a small cross section compared to the length of the sample is glued on a RuO_2 resistance plate, which is fabricated using the CMS technique [71]. The heater is used to send rectangular heat pulses to the sample, while the heat gradient between the top and the bottom of the sample, which is in contact with the heater, is detected with a differential constantan-chromel-constantan thermocouple. Hence it is important to note that the wires for the measurement of ΔT are in good thermal contact with the sample, but on the other hand they have to be electrically isolated. To obtain this the wires are glued on the sample with a special electrically insulating high temperature glue [72].
The voltage ΔV is detected using two gold wires attached with high temperature silver paint [69] at the bottom and the top of the sample. Here special attention is paid to make sure the contacts for ΔV and ΔT are attached at the same level of the sample in order to measure the real value of S and not just a fraction of it. Further the absolute temperature is measured using a copper-constantan thermocouple, which is in thermal contact to the sample.

4.4.2 The acquired signal of the thermopower experiment

As already mentioned above the heat gradient along the sample is established with the help of a rectangular heating pulse. At the same time the voltage and the temperature difference between both ends of the sample are monitored on the

screen and saved for the calculation of the Seebeck coefficient S. ΔV and ΔT as they are announced on the screen can be found in Fig. 4.5. Both signals are

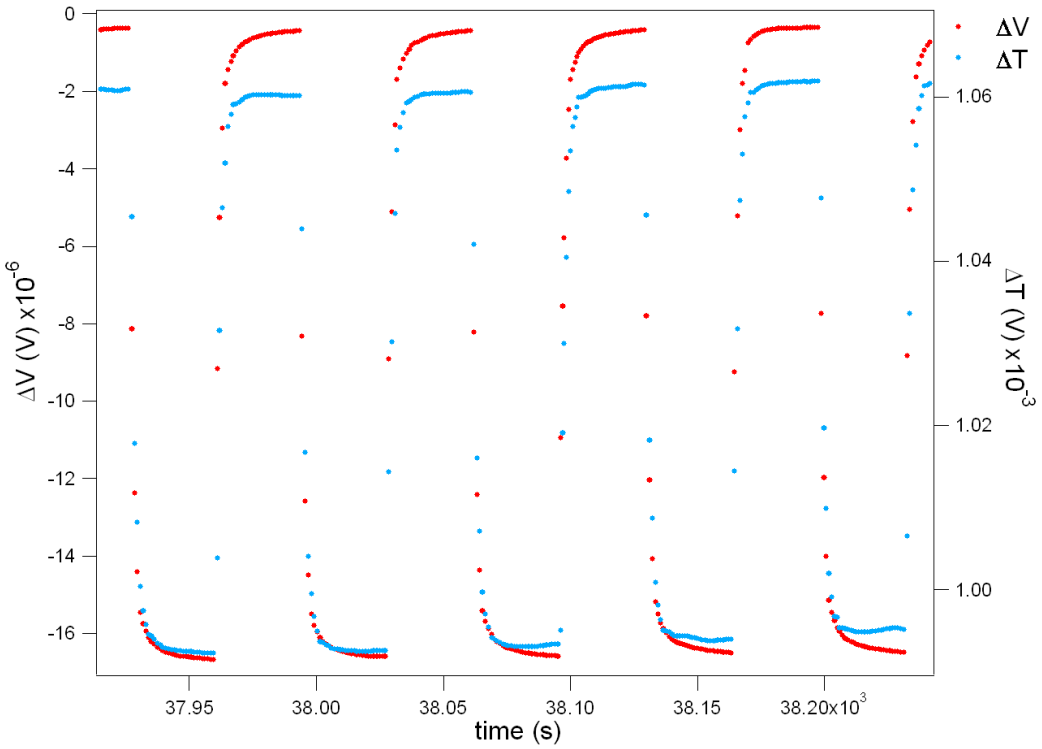

Figure 4.5: The signal as it is detected and shown on the screen. The red dots represent the voltage difference between both ends of the sample (in the order of magnitude of μV) and the blue points correspond to the voltage metered by means of the thermocouple.

shifted by an offset. The actual values can be calculated from the peak-to-peak amplitudes of this data and of course also the temperature difference from the voltage difference in the thermocouple.

4.4.3 The principle of the thermopower measurement

Thermoelectricity was first observed in 1826 by T. J. Seebeck [73]. He found that a current will flow in a closed circuit of two metals when the two junctions are at different temperatures. Nowadays, the Seebeck effect is associated with an open circuit and the resulting electrical voltage when two points of one electrical conductor are at different temperatures, as shown in Fig. 4.6.
The voltage $\Delta V = V_b - V_a$ is the thermoelectric voltage developed by this couple

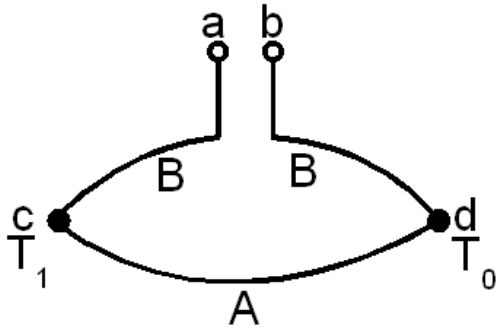

Figure 4.6: Open circuit to display the Seebeck effect. Two rods of different materials A and B are soldered together at the points c and d, which are held at the temperatures T_1 and T_2. A temperature difference ΔT results in a voltage that can be measured at the points a and b.

and the thermoelectric power is defined as:

$$S_{AB} = \lim_{\Delta T \to 0} \left(\Delta V / \Delta T \right), \tag{4.5}$$

where the temperature difference $\Delta T = T_1 - T_0$ is small with respect to the mean temperature $\Delta T \ll \left(T_1 + T_0 \right) / 2 = \bar{T}$. In our experiment the temperature gradient ΔT was held between 0.5 K and 1.5 K, while the temperature of the bath was at a minimum of 300 K. The relation $\Delta T = 1.5K \ll 300K = \left(T_0 + T_1 \right) / 2$ was well satisfied at any time.
In order to determine the Seebeck coefficient S in our experiment we used the A.C. method. Within this method the external conditions of the bath (e.g. is in our case either the temperature or the pressure) are slowly changed, while the heat current, which is used to generate the thermal gradient and the potential difference across the sample, is pulsed with a square wave. From these signals it is possible to obtain the absolute thermopower and in principle the heat conductivity at the same time (c.f. chapter 6).

4.5 Verification of the composition of the sample via NMR

Since the first sample did not undergo any kind of transition within our experimental limits, we assumed that it was not doped with the correct amount of chromium. More precisely the doping was probably too high or inhomogeneous and even at the highest accessible pressures the sample was still in the insulating state. In order to avoid these uncertainties for the subsequently prepared new batch of sam-

ples we tested if they did undergo the MIT in the anticipated temperature range with the help of the Knight shift of the ^{51}V NMR line.
After a brief introduction to the basic mechanisms of the Knight shift this verification will be presented in this section.

4.5.1 The Knight shift

The Knight shift, named after its discoverer W. D. Knight [74], is a shift in the magnetic resonance observable in metallic compounds. By writing ω_m as the resonance frequency in a metal, ω_0 as the resonance frequency in the non metallic phase, both in a constant static field, the frequency displacement $\Delta\omega$ is defined by:

$$\omega_m = \omega_0 + \Delta\omega.$$

This frequency displacement arises from hyperfine interactions of nuclear moments and spins of the conduction electrons. In the absence of an external field the electron spins do not have a preferred orientation and hence the average magnetic coupling to the nucleus is zero. The application of a static field H_0 polarises the electron spins and results in a non-vanishing coupling.
For the contact interaction (which usually dominates) the magnitude of the shift of the magnetic resonance due to the extra magnetic field ΔH is proportional to χ^s and given by the equation:

$$K = \frac{\Delta H}{H_0} = \frac{8\pi}{3} \left\langle |u_k(0)|^2 \right\rangle_{E_F} \chi_e^S. \tag{4.6}$$

$\left\langle |u_k(0)|^2 \right\rangle_{E_F}$ is the average probability density at the nucleus for all electronic states on the Fermi surface and χ_e^S the spin-susceptibility of the electrons (cp. [75]).
With this formula the basic features of the Knight shift are modelled correctly as it properly predicts the shift of the resonance frequency for a metal. For an uncorrelated metal χ_e^S is the Pauli spin-susceptibility and the fractional shift is independent of ω and temperature.
The change of the Knight shift with temperature in Cr doped V_2O_3 was already observed by Menth et al. in 1971 [76] and could be identified with the transition from the PM to the PI phase.

4.5.2 The NMR results

To be sure to have a sample that is doped roughly correctly, a temperature dependent experiment was performed upon cooling and afterwards heating in the temperature range between room temperature and 250 K. The results obtained

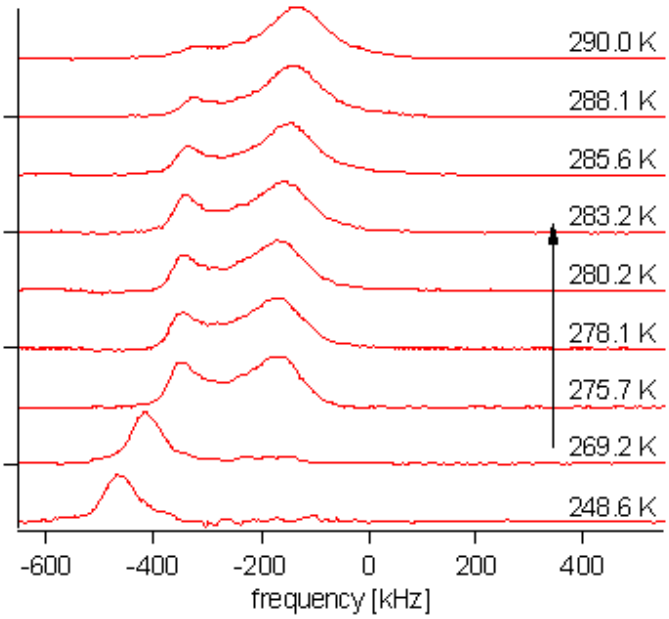

Figure 4.7: Transition from the metallic to the insulating state in the NMR spectrum upon heating the sample from 250 K to 300 K.

upon heating are shown in Fig. 4.7. At the two lowest temperatures only a single peak can be found around -400 kHz. This peak results from the metallic phase in the sample and with increasing temperatures it becomes smaller and smaller and from 275 K a second peak at about +200 kHz higher frequency appears, which corresponds to the insulating state. The size of this peak increases with increasing temperature and is at around 290 K the only visible feature in the NMR spectrum, i. e. the sample is completely in the insulating state. In the temperature region with two peaks both phases are present within the sample and the percentages of the sample in either of the phases is given by the ratio of the magnitudes of the peaks.
By comparing the transition temperature estimated in this way to the one at ambient pressure of Fig. 3.4 we deduce that our samples are doped with a similar amount of Cr as that of the reference (1.1 % of Cr).

Chapter 5

The speed of sound

5.1 Propagation of sound waves in solids

5.1.1 Tensor of deformation

A propagating wave may be defined as a localised change from the equilibrium conditions, which causes a perturbation that spreads out. These waves can be described with different parameters such as velocity, wavelength and wave vector. Thereby the definition of these parameters does not depend on the nature of the perturbation.
The propagation of this perturbation in a solid body corresponds to a deformation of this body. In mathematical terms this can be described as a change of the position vectors of the different points of the solid body. If $\underline{r}$ (with the components $x_1 = x$, $x_2 = y$, $x_3 = z$) is the position vector before the deformation and $\underline{r}$' the vector after the deformation the vector of the displacement $\underline{u}$ can be defined as:

$$u_i = x_i' - x_i, \tag{5.1}$$

where the deformation is completely defined by $\underline{u}$ as a function of the different coordinates x_i.
During the deformation the distance between the different solid points is varying and for two infinitely near points the vector between these two points before the deformation dx_i becomes $dx_i' = dx_1 + du_i$. So the distance evolves from

$$dl = \sqrt{dx_1^2 + dx_2^2 + dx_3^2}$$

before the deformation to

$$dl' = \sqrt{dx_1'^2 + dx_2'^2 + dx_3'^2}$$

afterwards, which, using the Einstein sum notation (summation over identical indications), can be written as

$$dl'^2 = \sum_i dx_i'^2 = (dx_i + du_i)^2.$$

The substitution of $du_i = \frac{\partial u_i}{\partial x_k} dx_k$ allows us to rewrite dl'^2 as

$$dl'^2 = dl^2 + 2\frac{\partial u_i}{\partial x_k} dx_i dx_k + \frac{\partial u_i}{\partial x_k}\frac{\partial u_i}{\partial x_l} dx_k dx_l,$$

which finally transforms into

$$dl'^2 = dl^2 + 2u_{ik} dx_i dx_k,$$

where the deformation tensor u_{ik} is defined as

$$u_{ik} = \frac{1}{2}\left(\frac{\partial u_i}{\partial x_k} + \frac{\partial u_k}{\partial x_i} + \frac{\partial u_l}{\partial x_i}\frac{\partial u_l}{\partial x_k}\right). \tag{5.2}$$

From the definition of this tensor it directly follows that u_{ik} is commutative (for further explanation see [77]):

$$u_{ik} = u_{ki}.$$

For every symmetric tensor at least one Cartesian system of coordinates exist in which all values of non-diagonal elements are zero (for proof and further information see e.g. [78, p. 158]). Matrices with non zero values only in diagonal elements are called diagonalised matrices and the values of these diagonal elements u_{11}, u_{22} and u_{33}) are referred to as principal values.
In practically all cases of deformation the variation of distance is small compared to the distances themselves. For this small deformation normally the vector of the displacement $\underline{u}$ and its components u_i are also small and in this cases the second order term in 5.2 is negligible. For further simplification the differentiations are written in the comma notation:

$$u_{ik} = \frac{1}{2}\left(\frac{\partial u_i}{\partial x_k} + \frac{\partial u_k}{\partial x_i}\right) \equiv \frac{1}{2}\left(u_{i,k} + u_{k,i}\right). \tag{5.3}$$

5.1.2 The elastic coefficients

Using the deformation tensor and assuming a linear stress-strain relation the elastic coefficients are defined by Hooke's law as a tensor of the fourth order:

$$s_{ik} = c_{ikjl} u_{jl}, \qquad i,k,j,l = 1,2,3, \tag{5.4}$$

whrere s_{ik} is the stress tensor. In total there are 81 different coefficients c_{ikjl}. From the symmetry of the stress and strain tensors it follows that:

$$c_{ikjl} = c_{kijl} = c_{iklj}.$$

With the condition of the existence of an elastic potential another constraint for the elastic coefficients

$$c_{ikjl} = c_{jlik},$$

allows a reduction in the number of independent elastic constants from 81 to 21 for the system with the lowest symmetry (i.e. a triclinic system). For crystals of a higher symmetry the number of independent constants becomes even fewer.
The tensor of elasticity is commonly written in matrix form, in which for each pair of indices the tensor takes one value:

tensor notation	11	22	33	23, 32	13, 31	12, 21
matrix notation	1	2	3	4	5	6

Now the complete set of equations can be written in matrix notation:

$$\begin{pmatrix} s_{11} \\ s_{22} \\ s_{33} \\ s_{23} \\ s_{31} \\ s_{12} \end{pmatrix} = \begin{pmatrix} c_{11} & c_{12} & c_{13} & c_{14} & c_{15} & c_{16} \\ c_{12} & c_{22} & c_{23} & c_{24} & c_{25} & c_{26} \\ c_{13} & c_{23} & c_{33} & c_{34} & c_{35} & c_{36} \\ c_{14} & c_{24} & c_{34} & c_{44} & c_{45} & c_{46} \\ c_{15} & c_{25} & c_{35} & c_{45} & c_{55} & c_{56} \\ c_{16} & c_{26} & c_{36} & c_{46} & c_{56} & c_{66} \end{pmatrix} \begin{pmatrix} u_{11} \\ u_{22} \\ u_{33} \\ u_{23} \\ u_{31} \\ u_{12} \end{pmatrix}, \tag{5.5}$$

with its 21 elastic constants.
For rhomboedric systems like the one studied in this work, V_2O_3, a higher symmetry decreases the number of coefficients to 6. The coefficients for a rhombohedral system can be found below in table 5.1.

Trigonal					
c_{11}	c_{12}	c_{13}	c_{14}	0	0
c_{12}	c_{11}	c_{13}	$(-c_{14})$	0	0
c_{13}	c_{13}	c_{33}	0	0	0
c_{14}	$(-c_{14})$	0	c_{44}	0	0
0	0	0	0	c_{44}	c_{14}
0	0	0	0	c_{14}	c_{66}

Table 5.1: Remaining elastic coefficients for a crystal with R-3c symmetry [79]

5.1.3 Equations of motion of sound waves

In a crystalline medium sound waves can be propagated in any direction of the crystal and in every direction there may be 3 different waves with different velocities, whose displacements are mutually perpendicular. Normally, these waves are neither purely transversal nor purely longitudinal waves, but for some special directions of each crystal, where the normal of the wave front concurs with the displacement vector of one of the three different waves we have a longitudinal or compressional wave. In this case the other two displacement vectors lie in the plane of the wave front and are two distinct transverse waves.
To calculate these directions and the resulting different velocities we start from the general equation of motion for a sound wave in 3 dimensions, which is given as:

$$c_{ijkl}u_{l,kj} = \rho\ddot{u}_i \qquad i = 1, 2, 3, \tag{5.6}$$

where ρ is the density of the material. The plane wave is propagating in the direction given by the wave vector $\underline{k}(k_1,\ k_2,\ k_3)$ with the unit vector $\underline{n}(n_1,\ n_2,\ n_3)$:

$$\underline{k} = \frac{\omega}{v}\underline{n} = \frac{2\pi}{\lambda}\underline{k}.$$

One solution for the differential equation 5.6 is a monochromatic plane wave with the following displacement vector:

$$u_l = u_{0l}e^{i(\underline{k}\underline{r}+\omega t)}, \qquad l = 1, 2, 3.$$

With this solution the projection of the equation of motion on the three axis x_i becomes:

$$c_{ijkl}u_{0l}n_k n_l = \rho v^2 u_{0i} \qquad i = 1, 2, 3. \tag{5.7}$$

The n_i are the components of the direction of propagation $\underline{n}$ and v is the sound speed along this direction. With a given direction of propagation and polarisation 3 different conditions for v are obtained, and only if all 3 conditions are fulfilled a propagation will be possible as a function of the elements of the tensor elasticity.

5.1.4 Propagation of sound waves in trigonal crystals

As already mentioned V_2O_3 does crystallise with trigonal crystal symmetry (space group R-3c, like Al_2O_3 to be more precise).
V_2O_3 has one axis of threefold symmetry (the c-axis) and three mirror planes. The matrix with the resulting elastic indices is shown in table 5.1. For a wave propagating in the direction of the c-axis [001] we get the following conditions

from equation 5.7:

$$(c_{44} - \rho v^2)u_{01} = 0 \qquad \text{transverse wave,} \tag{5.8}$$
$$(c_{44} - \rho v^2)u_{02} = 0 \qquad \text{transverse wave,} \tag{5.9}$$
$$(c_{33} - \rho v^2)u_{03} = 0 \qquad \text{longitudinal wave.} \tag{5.10}$$

According to this only longitudinal waves with the speed

$$v_l = \sqrt{c_{33}/\rho} \tag{5.11}$$

and transversal waves with the speed

$$v_t = \sqrt{c_{44}/\rho} \tag{5.12}$$

have the possibility to propagate (compare [79], Appendix A). The two different transversal waves are degenerated and can be treated as identical.

5.2 Bibliography for sound velocity and elastic constants

Since in this work the sample system will be studied by measuring ultrasonic sound waves it is convenient to review several important results obtained by this method for the sound speed and the different important elastic moduli. All measurements of the sound speed presented in this work were performed along the hexagonally indexed c-axis of the rhombohedral crystal. As shown above for this direction only c_{33} and c_{44} are crucial for the propagation of the longitudinal or respectively transversal sound waves and therefore only these two modes will be paid attention to.

In Fig. 5.1 the temperature dependence of the elastic coefficient for longitudinal waves c_{33} (among others) for pure and doped V_2O_3 with 1.5% Cr is given in the temperature range between 300 K and 640 K. The elastic constants were determined from measurements of the travel times of ultrasonic waves with 30- and 150-Mhz.

In both cases c_{33} decreases monotonically with increasing temperature but shows a remarkable change in the slope at around 550 K. The curves for both the doped and the pure sample are very similar and the absolute values are also nearly identical. Only the change of the slope might occur in the pure sample some ten degrees lower.

But in our region of interest for temperatures between 300 K and 500 K both curves can be approximated as identical and monotonically, nearly linearly decreasing with increasing temperature as predicted, for example, by the model proposed by Varshni [82]. In general this model, based on variation of the lattice

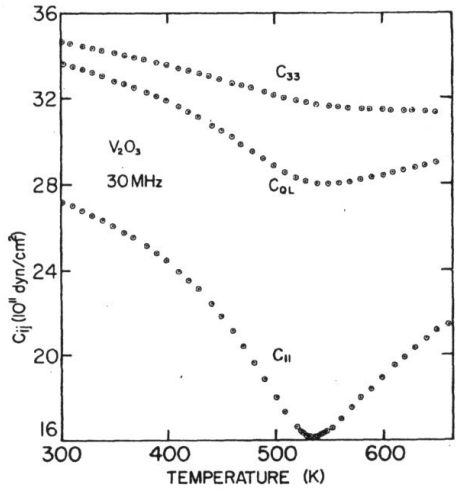

(a) Temperature dependence of c_{33} in pure V_2O_3 [80].

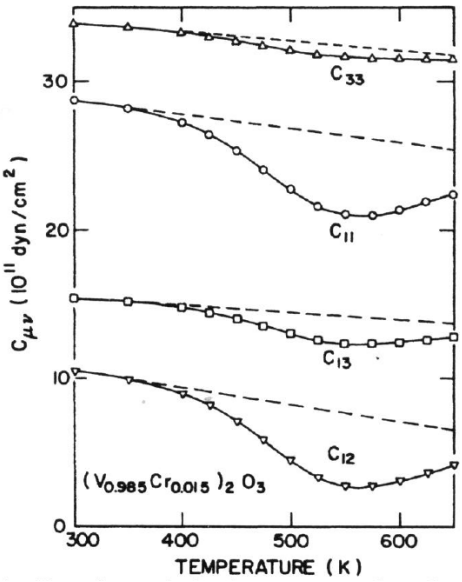

(b) Temperature dependence of c_{33} in V_2O_3 doped with 1.5% of Chromium [81]. The dashed curves represent a "background" calculated by Yang of a linear temperature dependence of the elastic contants.

Figure 5.1: Temperature dependence of c_{33} for pure and doped V_2O_3 with 1.5% Cr in the temperature range between 300 K and 640 K.

elastic energy due to anharmonicity, is only appropriate in the absence of, or far away from, phase transitions.

The temperature dependence of the shear elastic constant c_{44} for pure and V_2O_3 doped with different amounts of Cr is shown in Fig. 5.2 from [83]. It is easy to see that the curves for pure and the doped samples are quite different, while the amount of doping does not seem to have a very big impact, the characteristics for amounts of 1.5% and 3% of Cr are nearly identical.

For pure V_2O_3 the shear stiffness c_{44} increases very slightly parting from room to higher temperatures, before reaching a maximum and then decreasing and passing through a minimum above 500 K. Below room temperature c_{44} softens only slightly with temperature down to 155 K where the transition to the AFI phase with a monoclinic crystal structure occurs.

In contrast to this c_{44} shows for both Cr concentrations a drastic softening with decreasing temperature. For x = 0.03 the lowest measured temperature was 200 K to avoid damaging the sample as expected at the transition to the AFI phase around 180 K. Extrapolation of the data yields $c_{44} = 0$ at 180 K where the transition to the

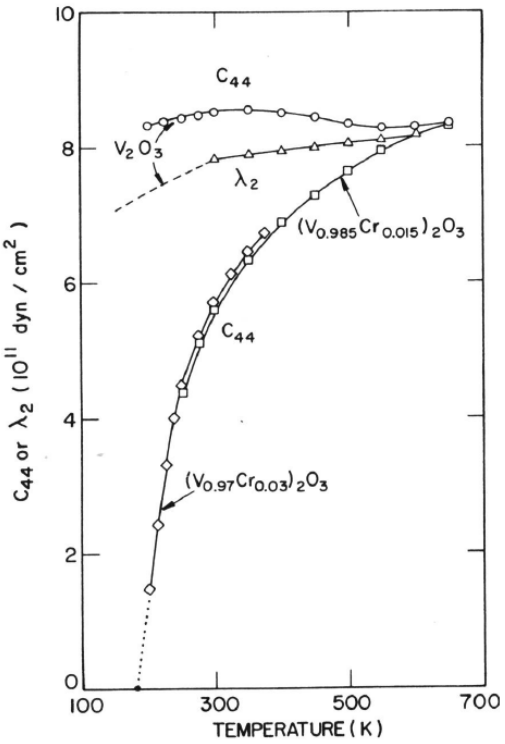

Figure 5.2: Temperature dependence of c_{44} for one pure and two differently doped samples of V_2O_3 with either 0, 1.5% or 3% of chromium [83]. The dotted part for x = 0.03 is a linear extrapolation of the curve between 200 K and 225 K. λ_2 represents the eigenvalues of the elastic constant matrix.

monoclinic phase takes place. For x = 0.015 the sample was already destroyed at 250 K at the transition to the PM phase. Because of this there is no data available for the lowest temperatures. But in the measured region the two curves are so similar that it is clear that $c_{44} = 0$ will be fulfilled at a temperature close to 180 K at the AFI phase transition, whereas the transition to the PM phase does not lead to any critical softening in the shear elastic constant c_{44}.

Yang et al. [83] explained the differences between pure and doped specimens, which is, due to the fact that all samples undergo the same symmetry change ($\bar{3}m \rightarrow 2/m$) at the low temperature transition, astonishing, as a result of the existence of anomalies in the temperature dependence of the lattice parameters and some interionic spacings [62] in the pure specimen that are absent in the doped ones.

For our pressure dependent measurements it is also of great interest how the important elastic constants evolve with pressure. Information about this can be gained from Fig. 5.3, where the evaluation of c_{33} and c_{44} between ambient pres-

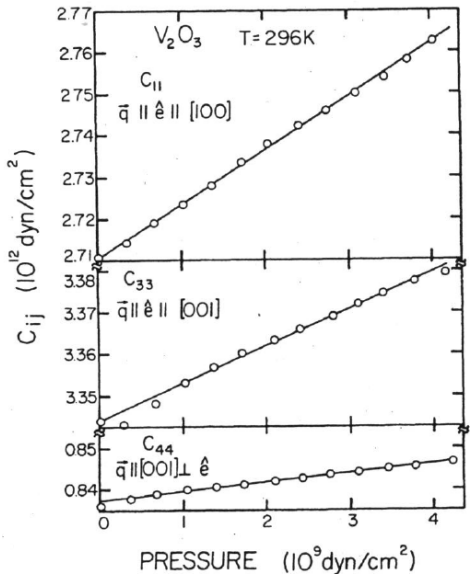

(a) Elastic constants c_{11}, c_{33} and c_{44} of pure V_2O_3 as a function of hydrostatic pressure obtained with ultrasonic modes with propagation and polarization directions given by $\vec{q}$ and $\hat{e}$ [84].

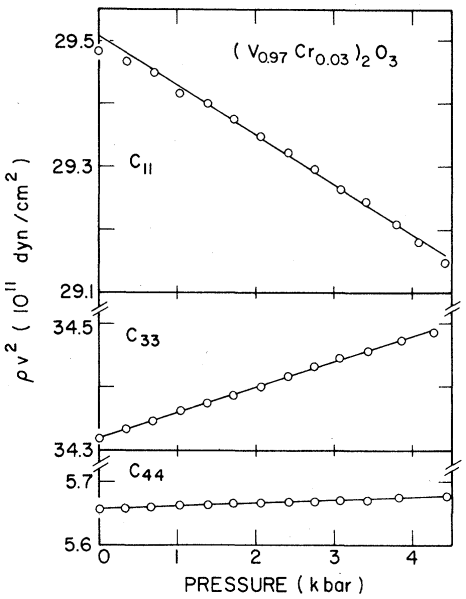

(b) Elastic constants c_{11}, c_{33} and c_{44} of $(V_{0.97}\ Cr_{0.03})_2O_3$ as a function of hydrostatic pressure [85]

Figure 5.3: Pressure dependence of c_{33} and c_{44} up to 4 kbar at room temperature. The solid lines represent the linear, least-squares fits to the data points.

sure and 4 kbar at room temperature is illustrated for pure [84] and 3% Cr doped [85] V_2O_3. The results shown were achieved by measuring the travel times of 30-MHz ultrasonic waves as a function of hydrostatic pressure.

In the case of pure V_2O_3 both elastic constants of interest show a positive linear pressure dependence over the full experimental interval. For the doped specimen the characteristics of the curves are generally the same. c_{33} and c_{44} both show a positive and linear dependence with pressure and for c_{33} even the absolute value is hardly changed. The effect on c_{44} is a bit bigger and the absolute value changes by 25%.

Finally, to compare the magnitudes of the different effects on the elastic constants in table 5.2 the absolute values of the interesting elastic constants and their variations with pressure are given. Although the absolute value of the longitudinal elastic constant c_{33} hardly changes upon doping, the pressure dependence for the doped specimen is more than three times smaller. As a result of this the relative pressure dependence becomes much smaller in doped samples.

For the transversal shear constant c_{44} the absolute value is nearly reduced to 50%

	x	c_{33}	c_{44}
c_{xx} (10^5 bar)	0	33.4	8.4
	0.015	33.9	5.6
$(\delta c/\delta p)_T$	0	8.9	2.1
	0.015	2.8	1.0

Table 5.2: The adiabatic elastic constants and their pressure derivatives at room temperature for $(V_{1-x}\ Cr_x)_2O_3$ for x = 0 [84] and x = 0.015 [85] in the pressure range up to 4 kbar.

of that of the pure upon a doping of 1.5% of Cr and roughly the same occurs for the pressure dependence of these values and consequently the relative pressure dependence of c_{44} is nearly unaltered by doping with small amounts of Cr.
While the relative dependences of the two elastic modes are, in pure V_2O_3, quite alike, the relative pressure dependence of the longitudinal mode as a result of an addition of Cr becomes much smaller and is in the doped specimen only half as big as the one of the transversal.

5.3 Measurements on pure V_2O_3

In this section measurements on pure V_2O_3 will be discussed. They were performed at temperatures between room temperature and 493K with applied hydrostatic pressures up to 6 kbar. In this temperature region V_2O_3 shows only metallic behaviour and no anomalies are expected.
A temperature dependent measurement at fixed pressure is displayed in Fig. 5.4. In this experiment the temperature was increased with a rate of 2 K/min at fixed

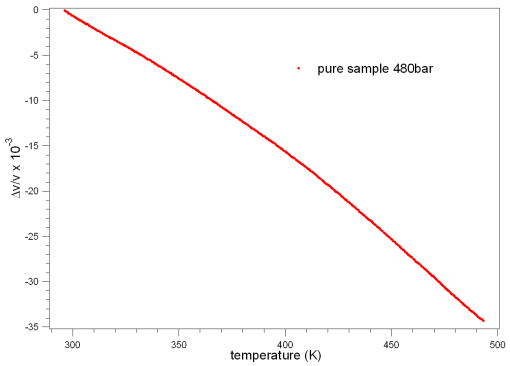

Figure 5.4: Temperature dependence of the relative sound speed for pure V_2O_3 in the temperature region between 290 and 495 K and at 480 bar.

pressure of around 480 bar. For this measurement only echoes of longitudinal ultrasonic waves were taken into account and the relative normalised change of the speed of sound $\Delta v/v$ for this mode decreases over the whole investigated temperature range, in total nearly 3.5%. This can be compared with 5.1 a), where the elastic constant c_{33}, given in the same temperature region, can with the help of equation 5.11 be related to the sound speed.
In the next step several pressure dependent measurements at different fixed temperatures were taken. One exemplary curve can be found in Fig. 5.5 which was

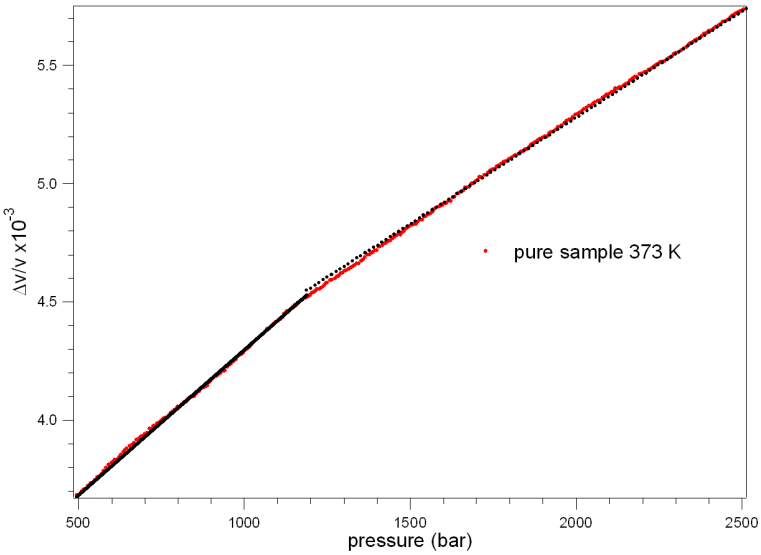

Figure 5.5: Pressure dependence of the relative sound speed for pure V_2O_3 at 373 K in the pressure range between 500 bar and 6000 bar.

performed at 373 K at pressures between 500 bar and 2500 bar. In this case $\Delta v/v$ increases monotonously with increasing pressure and two regions of linear behaviour with two different slopes can be identified. The first region starts from 500 bar and goes until approximately 1200 bar and the second from there until 2500 bar. The slope in the first region is clearly higher. Since pure V_2O_3 is close to the critical line (c.p. Fig. 3.2) it could be assumed that in the first region the normal increase of $\Delta v/v$ with pressure (compare Fig. 5.3 a)) is superposed with the effect of the metal-insulator transition. In the second regime at higher pressure this effect vanishes resulting in a smaller linear slope only coming from the normal pressure dependence of the elastic constants (compare again Fig. 5.3(a)). These measurements were performed at different fixed temperatures and the different results are shown and compared in Fig. 5.6. For higher temperatures the influence of the metal-insulator transition is expected to be visible in a broader region (e.g. even at higher pressures) and so the measurements for higher temper-

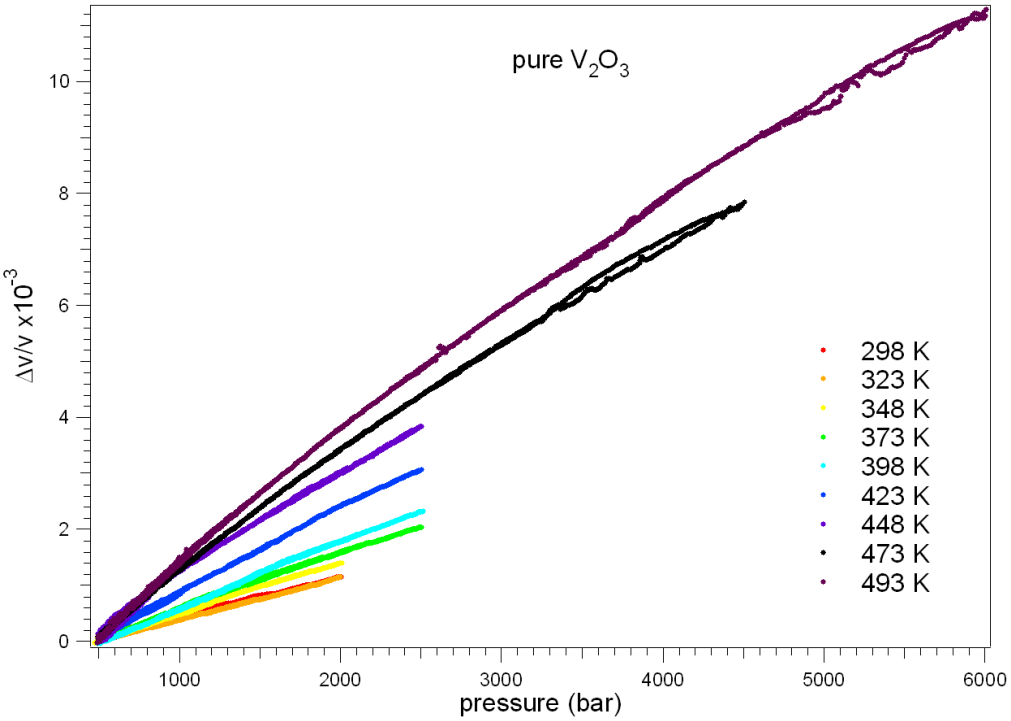

Figure 5.6: Pressure dependence of the relative sound speed for pure V_2O_3 at different fixed temperatures in the pressure range between 500 bar and 6000 bar. The experiments were performed in both directions with increasing and decreasing pressure. In order to be able to compare the different curves they are normalised to the same starting point $\Delta v/v = 0$ at 500 bar.

atures were taken in larger pressure intervals. In order to simplify the comparison of the data at different temperatures, all curves were normalised to a common point with $\Delta v/v = 0$ at 500 bar.

The two curves for the lowest two temperatures 298 K and 323 K are nearly identical. They can be identified with the pure effect of pressure on the elastic constants. From the estimation of the region with the same slope for different higher temperatures it can be estimated to which pressures the sound velocity is affected by the previous metal-insulator transition for the different temperatures. For the two lowest temperatures this “critical” pressure is less than 500 bar, for 348 K it is 1250 bar, for 373 K around 2000 bar, for 398 K it is already difficult to identify any similar slope below 2400 bar and for higher pressures it cannot be found. It becomes clear that the region affected by the metal-insulator transition is very broad, especially at high T.

5.4 Measurements on Cr doped V_2O_3

In this section the main part of the speed of sound experiments will be presented. In order to be able to cross the transition at fixed temperatures by changing the pressure within our experimental limits we used (according to the phase diagram in Fig. 3.2) samples of V_2O_3 doped with a nominal amount of 1.1 % of chromium.

5.4.1 Temperature dependent measurements

In the very first test of our experimental set-up, an experiment was taken out without the pressure cell and upon cooling at ambient pressure. The temperature was changed from room temperature down to 230 K while both, the longitudinal and the transverse mode of the sound velocity were examined. The results of this trial can be found in Fig. 5.7. In this first test measurement the temperature control was

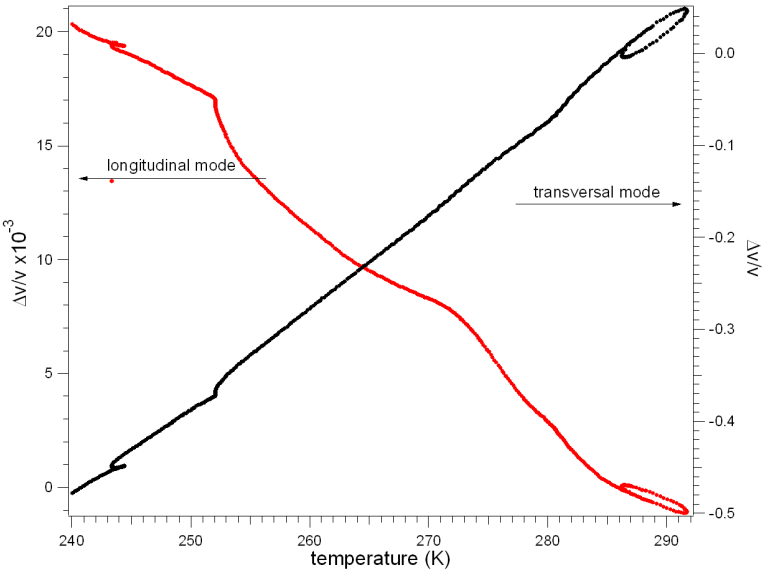

Figure 5.7: Observation of the longitudinal and transversal modes of the speed of sound at ambient pressure upon cooling from room temperature to approximately 240 K.

not very satisfactory. The curves show some loops, which are due to this insufficiency. Nonetheless, it is easy to see that the two modes behave quite differently. The relative change of the sound velocity determined using the longitudinal mode increases with decreasing temperature, while the speed of sound of the transversal mode decreases with temperature and the relative change of the sound velocity is for this mode around 20 times bigger than for the longitudinal one . These two

results are in good agreement with the ones in the literature (compare Fig. 5.1 for the longitudinal and Fig. 5.2 for the transversal mode).

Another temperature dependent measurement, this time in the pressure cell and at fixed pressure can be found in 5.8. In this experiment the temperature was

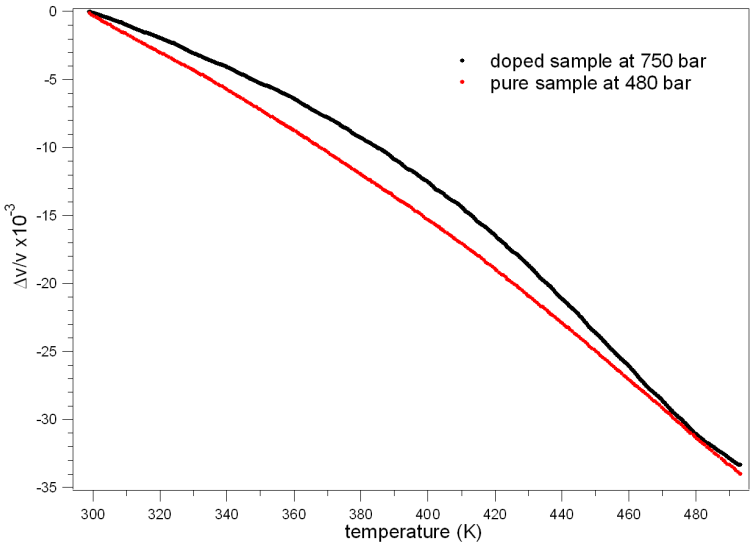

Figure 5.8: Temperature dependence of the relative sound velocity for chromium doped V_2O_3 in the temperature region between 295 and 495 K and at 750 bar. For comparison also the pure curve at 480 bar was added.

lowered with a rate of 1 K/min at fixed pressure of around 750 bar and only echoes of longitudinal ultrasonic waves were taken into account to calculate the change of the sound velocity. As a result the relative normalised change of the speed of sound $\Delta v/v$ for this mode decreases over the whole investigated temperature range, in total nearly 3.5%. The data of the pure specimen of Fig. 5.4 was added to facilitate the comparison between the two curves. Both curves were normalised to start at 298 K at $\Delta v/v = 0$ and end at 493 K at nearly the same value of $\Delta v/v = -3.3\%$. In contrast to this the decrease in the doped sample in the beginning is smaller than the one in the pure specimen. This results in a difference of $\approx 0.2\%$ at around 380 K and afterwards the decrease of the doped sample increases and at the highest accessible temperature the two curves are at identical values. The similarities between the two curves can be understood, because as shown in Fig. 5.1 the behaviour of the elastic constant c_{33} for both specimens is very similar. The difference between the two curves is not so easy to explain and it can only be speculated about the reasons.

5.4.2 Experiments at low temperatures

In this section several experiments on $(V_{0.989}\ Cr_{0.011})_2O_3$ at temperatures below the critical point will be reviewed. At temperatures below T_C the metal-insulator transition is a first order transition and as a consequence of this irreversible damage is to be expected by the crossing of the transition. To prevent this, the measurements were made just in the pressure range where the sample is still in the insulating region and far enough away from the transition.
Measurements were carried out at room temperature and every 25 K up to 448 K just below T_c and are displayed in Fig. 5.9. The different experiments were

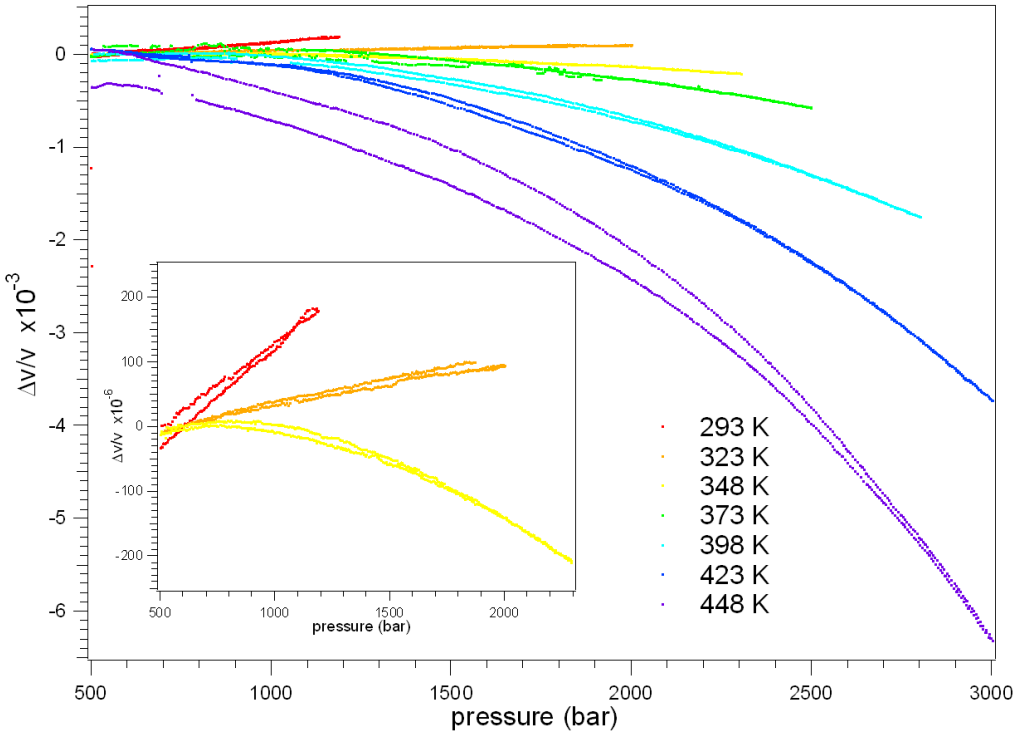

Figure 5.9: Pressure dependence of the relative sound speed for Cr doped V_2O_3 at different fixed temperatures below T_C in the pressure range of the insulating phase. Inset: zoom on the behaviour of the three lowest temperatures.

performed in different pressure ranges well below the transition up to 3000 bar for the highest temperatures. It is to note that especially the lowest temperatures behave quite different. While for 293 K and 323 K $\Delta v/v$ increases with p as it is to expect in absence of any critical behaviour (c.p. Fig. 5.3) the effect of the metal-insulator transition becomes more and more visible for higher temperatures and $\Delta v/v$ becomes negative. The decrease of the speed of sound commences

with increasing temperatures at lower pressures and the overall decrease becomes larger. Finally, the relative change is for 448 K with more than 0.6% the largest. In order to emphasize the differences at low temperatures the inset of 5.9 shows a zoom on just the curves at 293 K, 323 K and 348 K. For the lowest temperature $\Delta v/v$ increases linearly with pressure over the whole investigated pressure range up to 1200 bar, for 323 K the increase is already much weaker and only linear in the low pressure regions, at higher pressure between 1500 bar and 2000 bar the slope decreases. Finally for 348 K, only in the first few hundred bars a very slight increase in $\Delta v/v$ could be suspected, but already below 1000 bar the ratio begins to decrease continuously until 2500 bar. To understand and interpret the striking differences at the three temperatures it is required to note that at room temperature the normal pressure dependence of the elastic constants (cf. Fig. 5.3) is a linear increase over the whole pressure range. Even though the transition pressure at constant Cr concentration (as it is the case here, because for all measurements the same sample was used) is shifted to higher pressures for higher temperatures, this effect is superposed by the fact that for higher temperatures the effect of the transition, which results in a parabolic decrease with a minimum at p_C, becomes much broader. As a result of this the linear increase is only valid for lower pressures for 323 K and for 348 K $\Delta v/v$ increases only at the very beginning visibly and afterwards a decrease of the order of magnitude of the increase at room temperature can be noticed.

5.4.3 Influence of the transition on the transversal mode

As mentioned above there are two different modes of propagation possible in the direction of the hexagonal c-axis. After considering the development of the longitudinal mode above, in this chapter the influence of the PM-PI transition on the transversal mode will be estimated. The transversal mode could not be observed for all samples, for some the echoes of this mode were very small, for some not visible at all and only for a marginal amount of samples they were reasonably bigger than the noise, which allowed information about the relative change of the speed of sound of v_t to be extracted.
It is to note that due to the crystal structure of ZnO, if the layer is sputtered sufficiently slowly onto the sample, the main piezoelectric axis is parallel to the c-axis. Hence the transversal mode should not be excited. Though it is only possible to observe the transverse mode due to imperfections in the ZnO layer.
As the position of the echoes varies with pressure and especially with temperature, even for samples with reasonably large echoes of transverse sound waves, it was not always possible to extract the wanted information at any temperature. The transverse waves needed the double time to travel trough the sample, e.g. they were travelling with half the speed of the longitudinal waves. This can be under-

stood from the values of Tab. 5.2, which show that roughly $c_{33} \approx 4c_{44}$. According to Eq. 5.11 and 5.12 follows:

$$v_l = \sqrt{c_{33}/\rho} \approx \sqrt{4c_{44}/\rho} \approx 2v_t.$$

It was possible to calculate the relative change of the speed of sound of the transverse mode in the insulating region at temperatures between 323 K and 473 K. For 493 K the transverse echoes were overlapping with the longitudinal ones for all the echoes with a reasonable signal-to-noise ratio and no phase change could be calculated.
In order to evaluate the influence of the PM-PI transition in Fig. 5.10 the relative changes of the sound speed of the transversal mode for different temperatures where it was possible to observe it are shown.

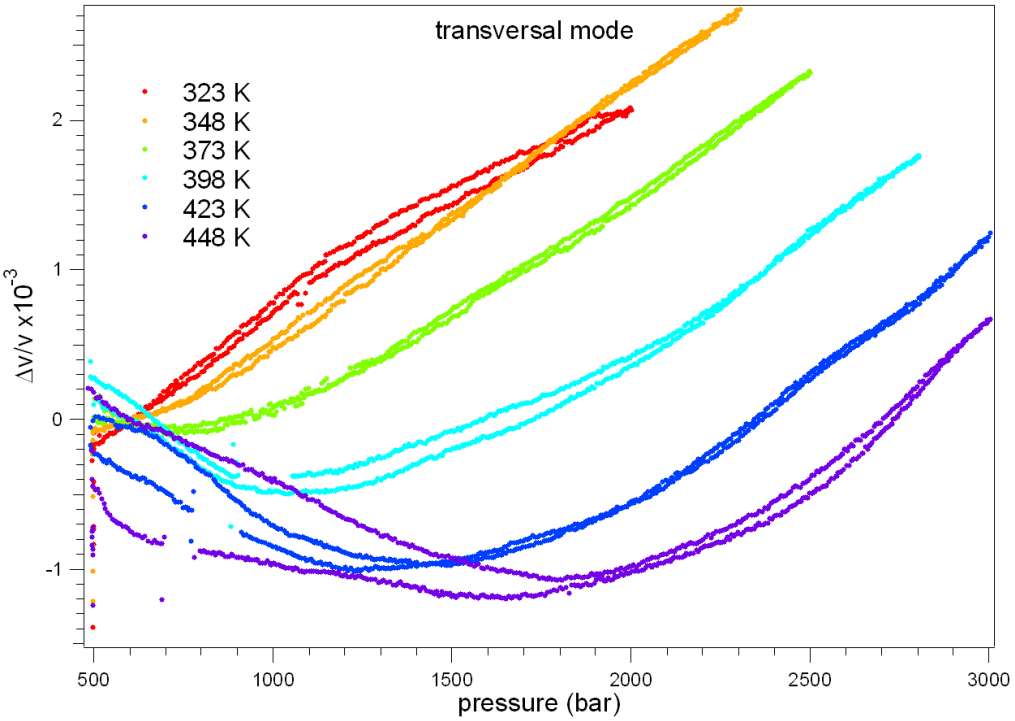

Figure 5.10: Pressure dependence of the relative sound speed of transverse sound waves for Cr doped V_2O_3 at different fixed temperatures below T_C in the pressure range of the insulating phase.

For the two lowest temperatures both curves are quite similar and the two slopes are nearly identical. For higher temperatures an anomaly can be noticed at low pressures. This anomaly expresses itself in a plateau at 373 K and is at higher temperatures emphasised to a dip whose minimum is shifted to higher pressures

and deeper with increasing temperature. While the low pressure regime is quite different for all temperatures the region of higher pressure is very similar. The slope for all temperatures is virtually the same. Thus it seems quite sure that the PM-PI transition does not affect the transversal mode. In analogy with the anomaly at low temperatures it could be speculated that it comes from the structural transition at lower T.

5.4.4 Pressure sweeps from the insulating to the metallic phase above T_c

In this section the experiments, which were carried out over the whole accessible pressure interval at temperatures above T_c will be presented and discussed.
Although the primary aim of this thesis is to study the evolution of the speed of sound across the critical line it proved quite difficult to be carried out. One reason was that by crossing the transition below T_c the samples were damaged irreversibly. Even at temperatures significantly higher than T_c the samples were often damaged by micro cracks due to the rapid volume change, which prevented the sound waves from travelling through the sample without being distorted. Hence the signal became smaller with every measurement and only a very limited number of measurements could be performed with the same sample. Another problem was that the doping in the batch of the samples did not seem to be very homogeneous and therefore the results obtained with different samples were not always comparable. Further, in one other measurement there were apparently problems with the temperature measured by the thermocouple and these results also could not be used.
Despite these experimental difficulties in Fig. 5.11(b) a number of consistent results for the relative change of the speed of sound with pressure at temperatures from 458 K to 493 K are presented. For comparison the low pressure results at lower temperatures between 323 K and 448 K as already presented in Fig. 5.9 are also added and all measurements are starting from the common point $\Delta v/v = 0$ at 1000 bar.
At temperatures where a scan in the full pressure range was taken the relative sound velocity decreases with increasing pressure until a minimum around 4000 bar. After this minimum, $\Delta v/v$ increases symmetrically to the decrease below p_c up to the highest accessible pressures for our experiment. It is easy to recognise that the total amount of the decrease of the signal is the largest for 458 K ($\approx T_c$) and then decreases monotonically with increasing temperature. For 458 K a discontinuity or jump in the acquired signal can be seen on the high pressure side of the transition. This jump is too big to be due to the change of the lattice parameter at the transition and is probably an artefact of the calculation of the phase, which

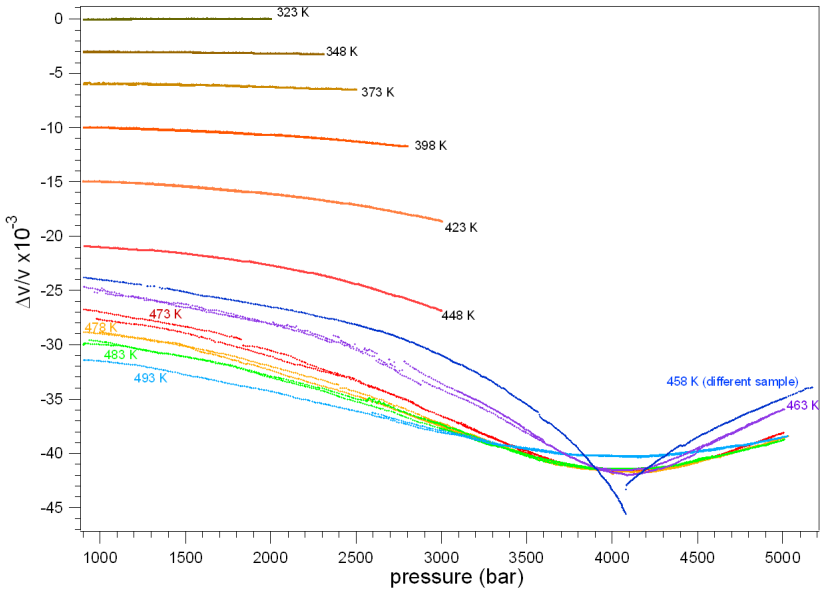

(a) In this graph all curves are normalised to 323 K and 1000 bar.

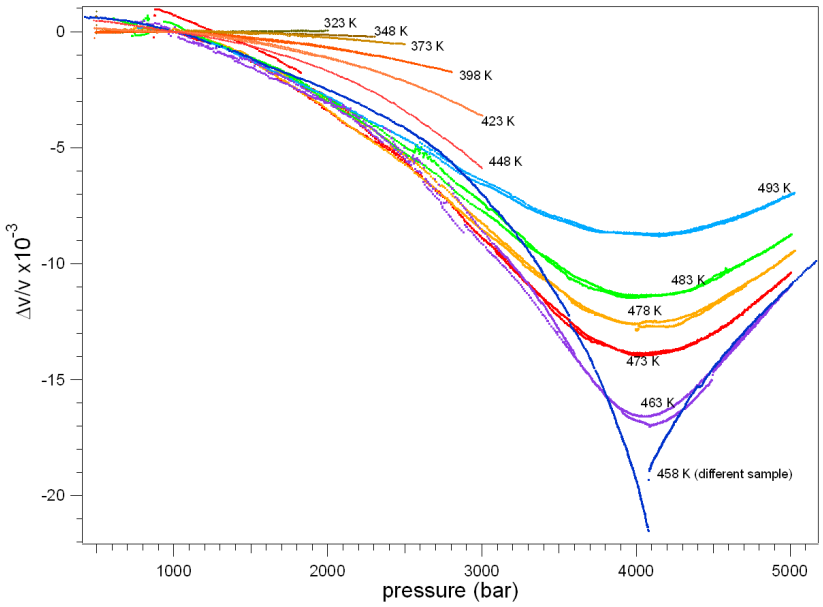

(b) To be able to compare the different measurements all graphs were normalised to start with a relative change of the sound velocity of 0 at 1000 bar.

Figure 5.11: Pressure dependence of the relative sound velocity in the full accessible pressure range for V_2O_3 doped with 1.1% of Cr in the temperature range between 323 K and 493 K.

changes very fast at the transition. The maximal amplitude of the decrease of the relative speed of sound is with $\Delta v/v > 2\%$, which is relatively large and clearly exceeds the effect of the expansion of the lattice at the transition. In contrast to this, the width of the critical region seems to increase with increasing temperature, i.e. the critical behaviour starts at lower pressures for higher T. Below T_c this is very easy to see, but above T_c a zoom of the first pressure region is needed. Another observation is that the actual transition pressure, i.e. the minimum of $\Delta v/v$, stays roughly at constant pressure. Although the minimum for the broad curves at $T > T_c$ is somehow difficult to determine, this feature can be identified with a crossover line above the critical point.

Naturally, these results have to be compared to the theoretical predictions made by DMFT and are shown in Fig. 2.9. In the theoretical predictions $\Delta v/v$ vanishes completely at the critical point and even nearly 10 K above the critical temperature it decreases more than 20 %, while the maximum change observed by us is only of around 2 %. This indicates that the values used for the calculation might have to be adjusted to meet the experimental results. Further the results of Hassan's calculations [3] show a pronounced asymmetry, while our findings seem to be perfectly symetric at least above T_c. Because of a lack of experimental data of the transition at temperatures below T_c no comparisons of this behaviour can be drawn. The only curve at a temperature well above T_c shows a much more rounded characeristic at the minimum of $\Delta v/v$ (the transiton point), but it is still asymetric. This is in qualitative agreement with our observations, although our curves show now sign of asymetry. In another comparison to Fig. 2.9 the width of the critical region of the calculations can be compared to our results. Their curve, for instance at $T = 1.016T_c$, corresponds roughly to our curve at 463 K. The half width of the calculated critital decrease of the sound velocity (defined as the width where the decrease is at 10 % of the maximum decrease) of this curve is, using their eleastic bulk modulus of $B_0 \approx 2000\ kbar$, approximately 10 kbar. The width, defined in the same way, of our curve is only 3000 bar. The difference of a factor three, shows the qualitative agreement of the calculation to our experiment, but confirms also that the excact values of the calculation should not be taken too seriously.

In order to get a more quantitative impression of the transition and the crossover points in Tab. 5.3 the corresponding pressures to the estimated positions of the

temperature (K)	458 K	463 K	473 K	478 K	483 K	493 K
pressure (bar)	4079	4086	4049	4054	4065	4150
$amp_{min}\ \Delta v/v\ (10^{-3})$	21.54	16.79	13.92	12.64	11.40	8.78

Table 5.3: Pressures corresponding to the minima of the sound velocity with their amplitude for the different temperatures.

minima of the relative sound speed at the different temperatures will be given with their amplitudes. When the values for the different senses of the measurement for diverse temperatures were not identical the mean of the two curves is given. For the pressures of the transition it is to note that especially for the higher temperatures it becomes more difficult to identify distinct transition pressure as the shape of the curves becomes very rounded.
This can explain why no clear trend for the transition pressures can be identified and the transition pressure stays roughly constant.
Now the critical point can be estimated with the help of Fig. 5.11(b). As the curve for 458 K has a shape that quite differs from the ones at higher temperatures and also the amplitude of the decrease is the largest we assume the curve at 458 K to be below or at the critical temperature. The next temperature is already above T_c which we assign to $T_c = 458\ K \pm 5\ K$. The relative high uncertainty is due to the lack of data point in between those two temperatures. In principle, the critical pressure can be estimated very precisely from the position of the minimum at 458 K, but the large uncertainty in T_c yields $p_c = 4080\ bar \pm 40\ bar$.
Another way to compare the different graphs is displayed in 5.11(a). First, the data was normalised to start at 1000 bar with a relative change of the sound velocity of zero and afterwards the different graphs were shifted by the change of $\Delta v/v$ of the temperature as deduced from Fig. 5.8.
It is to note that all the different curves between 463 K and 483 K have their minimum at the same point, despite starting from different values of $\Delta v/v$ at 1000 bar. The biggest change in $\Delta v/v$ can be found for the curve nearest to the critical temperature at 458 K.

5.5 Analysis of the data

In this section we want to take a closer look at the coupling of the order parameter to the different ultrasonic modes and at the critical behaviour of the sound velocity at the Mott critical endpoint.

5.5.1 Coupling of the order parameter to the different ultrasonic modes

The influence of the transition on the transversal mode has been estimated in Fig. 5.10, where no sign of a critical behaviour of this mode could be found while approaching the transition.
We try to analyse these findings in the context of the Landau theory of phase transitions [86]. The general framework to study mainly structural phase transitions by means of ultrasonic experiments was developed by W. Rehwald [87].

Phase transitions can be described by an order parameter that characterises the amount of change during the transition. In the mean field free energy F_c, the effect of a transition on the elastic constants, is introduced by a term coupling the strain ϵ and the order parameter m. Hence, this term is responsible for spontaneous strain that appears in connection with the ordering process and also describes the effect of an external strain on the order parameter. Usually, the coupling term is written in terms of increasing powers of m_i and ϵ_j:

$$F_c(m_i, \epsilon_j) = \beta_{ij} m_i \epsilon_j + \gamma_{ijk} m_i m_k \epsilon_j + \delta_{ijk} m_i \epsilon_j \epsilon_k + \dots . \tag{5.13}$$

The coefficients that are different from zero are determined by symmetry and ϵ can be a scalar or a vectorial quantity or a tensor, depending on the strain it represents. In general the possible combinations can be obtained by means of group theory considerations. Since here the situation is simple due to, as we will see shortly, a scalar order parameter, we can use simple intuitive reasoning. For example, for a longitudinal sound wave ϵ is a scalar quantity as the sound wave propagates through compression. For transversal sound waves and their polarisation vector it is a vector.
Equation 5.13 is also the link through which the order parameter becomes observable in ultrasound experiments via the elastic constants:

$$c_{mn} = \frac{\partial^2 F}{\partial \epsilon_m \partial \epsilon_n}$$

and their connection to the speed of sound.
Usually, the lowest order term of Eq. 5.13 plays the dominating role and in Fig. 5.12 the three simplest cases with respect to the elastic constants are shown. Case (a) shows linear coupling in order parameter and strain $F_c = \beta m \epsilon$, (b) shows linear coupling in strain but quadratic in the order parameter $F_c = \gamma m^2 \epsilon$ and finally (c), which illustrates the case of linear coupling in the order parameter but quadratic in the strain $F_c = \delta m \epsilon^2$.
A comparison of the shape of the different cases in Fig. 5.12 to our results (i.e. Fig. 5.11) across the transition strongly suggests that strain and order parameter are coupled linearly.
For a phase transition without symmetry breaking the order parameter m is expected to be a scalar. As the scalar order parameter cannot be coupled linearly to the vectorial ϵ of the transversal mode, this coupling has to be at least of second order, while the scalar order parameter and the scalar ϵ of the longitudinal sound wave are coupled linearly and this is the dominating term. From this it is understandable why for the high temperature MIT the critical behaviour of the longitudinal mode is clearly dominating.

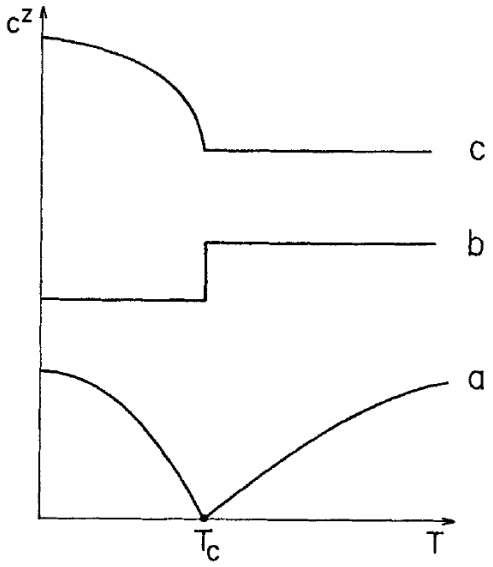

Figure 5.12: General behaviour of the elastic moduli at a continuous phase transition for three different types of coupling between order parameter and strain [87].

Approaching the low temperature transition to the AFI phase, which is combined with a symmetry breaking the situation is different. In this case the order parameter is related to a structural phase transition and cannot be a scalar because it lowers the crystal symmetry. Hence, the critical behaviour at this transition should be much better observable in the linear coupled transversal modes. This is in agreement with our findings of Fig. 5.7 where the relative change in the speed of sound of the transversal mode is 20 times bigger than the one of the longitudinal sound waves.
These considerations confirm that at the high temperature Mott transition in V_2O_3 no symmetry breaking exists.

5.5.2 Critical behaviour at the Mott transition

As already pointed out by Castellani et al. [88] it is possible to assign an analogy between the MIT and the liquid-gas transition. Basically, we can consider the double occupation (or holes) density in each phase as an order parameter in this framework. The insulating state corresponds to a gas with a low density of double occupied sites and the metallic phase corresponds to a liquid with a high density of double occupied (and non occupied) sites. This analogy was given theoretical confirmation by Kotliar et al. [89, 90] using the Landau theory derived

from DMFT. They were able to derive an order parameter description of the Mott transition near the critical point in the $U - T$ plane.

Whilst from the theoretical point of view this double occupation density is often used as an indicator of the transition, this quantity proves, nonetheless, to be experimentally only accessible with difficulties. But the density of states at the Fermi energy can also be used as an indicator of the transition, implying that the density of states is characterised by a quasi-particle peak in the Landau theory and by a gap in the insulating phase. This was verified by Kotliar et al. [91] by a thermodynamic approach, where they were able to show that the density of states at the Fermi energy in 5.13(b) behaves in a singular way at the transition just like the double occupation density 5.13(a) with mean field critical exponents as a result of their approximations. Limelette et al. [5] identified in a first order approximation

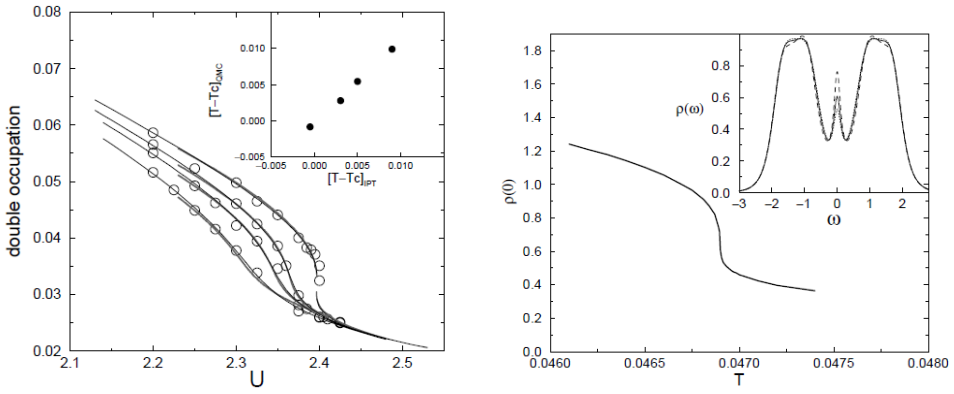

(a) Double occupation as a function of U for different temperatures.

(b) The density of states at the Fermi energy $\rho(0)$ as a function of temperature in the critical region ($U = 2.46316 \approx U_c$).

Figure 5.13: Critical behaviour of the double occupation density and the density of states at the Fermi level in the context of the dynamical mean-field theory of the Hubbard model.

the DC conductivity as proportional to the density of states of the Fermi level and used it as an order parameter for the Mott transition in $(V_{0.989}\ Cr_{0.011})_2O_3$. By using this they were able to derive the values of the critical exponents β, δ and γ in accord with the expected mean field values, which are, together with the ones of the numerical solved 3D Ising model, shown in Tab. 5.4.

	δ	β	γ
Ising 3D	4.814	0.327	1.239
Mean field	3	0.5	1

Table 5.4: Theoretical critical exponents from mean field theory and the 3D Ising model.

5.5.2.1 The scaling functions

In the vicinity of the critical point, scaling implies that the whole data set can be mapped onto a universal form of the equation of state [92]:

$$m = h^{1/\delta} f_{\pm}\left(\frac{h}{|t|^{\gamma\delta/(\delta-1)}}\right), \tag{5.14}$$

where γ and δ are critical exponents associated with the order parameter and susceptibility respectively. $h = \frac{|p-p_c|}{p_c}$ is the reduced pressure and $t = \frac{|T-T_c|}{T_c}$ the reduced temperature. $f_{\pm}$ are universal scaling functions above and below T_c. At the critical temperature the order parameter diverges as:

$$m = h^{1/\delta}. \tag{5.15}$$

As it was shown in chapter 2 the sound velocity is proportional to the electronic susceptibility χ_{el} and according to this it can be scaled as the derivative of the order parameter with respect to the field:

$$\chi = \frac{dm}{dh} = \frac{1}{\delta} h^{\frac{1}{\delta}-1} f\left(\frac{h}{t^{\beta\delta}}\right) + h^{\frac{1}{\delta}} t^{-\beta\delta} f'\left(\frac{h}{t^{\beta\delta}}\right) \tag{5.16}$$

$$= h^{\frac{1}{\delta}-1}\left(\frac{1}{\delta} f\left(\frac{h}{t^{\beta\delta}}\right) + \frac{h}{t^{\beta\delta}} f'\left(\frac{h}{t^{\beta\delta}}\right)\right) \tag{5.17}$$

$$= h^{\frac{1}{\delta}-1}\left(\frac{1}{\delta} f\left(x\right) + x f'\left(x\right)\right). \tag{5.18}$$

The expression inside the brackets is now replaced by a second function $f_2(x)$ of the same argument $x = \frac{h}{t^{\beta\delta}}$ and we get the following expression for the susceptibility:

$$\chi \propto h^{\frac{1}{\delta}-1} f_2\left(\frac{h}{t^{\beta\delta}}\right). \tag{5.19}$$

The asymptotic behaviour of f_2 is:

$$\lim_{x\to\infty} f_2(x) \propto constant,$$

which leads to the relation for the critical behaviour with pressure:

$$\chi_{t=0} \propto h^{\frac{1-\delta}{\delta}}. \tag{5.20}$$

From the asymptotic behaviour:

$$\lim_{x\to 0} f_2(x) \propto x^{1-\frac{1}{\delta}},$$

it follows, using the relation between the critical exponents:

$$\gamma = \beta(\delta - 1), \tag{5.21}$$

for the temperature dependence of the critical behaviour:

$$\chi \propto t^{1/\gamma}. \tag{5.22}$$

5.5.2.2 Pressure dependence of the critical behaviour of the sound velocity

In this spirit we want to take a look at the critical behaviour of the speed of sound near the critical temperature and try to find a scaling in accordance to Eq. 5.20. In order to have the purely critical part of the sound velocity we subtracted the value measured in the experiment v_m from the background value of the sound velocity indefinitely far from the transition v_0. The critical part of the sound velocity $v_c = v_0 - v_m$ is plotted against the reduced pressure $h = (p - p_c)/p_c)$ and can be found in Fig. 5.14. It was not possible to fit the critical behaviour of the pressure with a power law in a reasonable large region. For comparison a curve with the attended mean field exponent of $\beta = 3$ is plotted, which is only relatively far away from the critical pressure in agreement with our data. The departure of our data from this power law is understandable as we did not observe a divergence to infinity, but just to finite values, at p_c.

5.5.2.3 Temperature dependent critical behaviour

As it was already introduced in chapter 2 within the compressible Hubbard model [1, 2] the first order Mott transition occurs due to the instability where κ_{tot} equals zero. This arises due to the divergence of κ_{el} when $T \to T_c^{el}$.
In this case it can be defined:

$$v \propto \sqrt{\kappa_{lat} - \kappa_{el}} \propto \sqrt{1 - \frac{\kappa_{el}}{\kappa_{lat}}}.$$

From Eq. 5.22 we obtain the critical behaviour with respect to the temperature:

$$\kappa_{el} \propto \chi_{el} \propto t_{el}^{-\gamma},$$

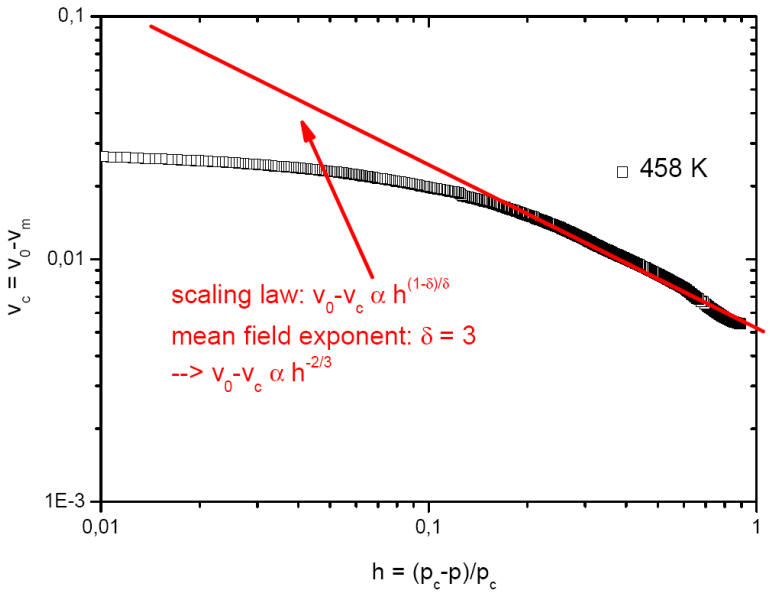

Figure 5.14: Comparison of the critical behaviour of the sound velocity at 458 K with the expected mean field scaling law.

where $t_{el} = |\frac{T-T_c^{el}}{T_c^{el}}|$ and T_c^{el} is the purely electronic transition temperature. If we take the expected mean field exponent $\gamma = 1$ as, for example, obtained by resistivity measurements in Cr doped V_2O_3 [5] and further regard the part of the stiffness arising from the lattice as constant $\kappa_{lat} = b$, this equation simplifies to:

$$v \propto \sqrt{1 - \frac{b}{t_{el}}}.$$

This is the change of the speed of sound due to the compressibility divergence. If we want to normalise this with respect to the absolute speed of sound, we get:

$$\frac{\Delta v}{v} = \sqrt{1 - \frac{b}{t_{el}}} - 1. \tag{5.23}$$

In this function there are only two parameters. b remained as a free fit parameter and t_{el} was adjusted to reproduce our data. The highest T_c^{el} that allowed to reproduce our data was 440 K. Now, the results obtained from Eq. 5.23 are compared to the amplitudes of the minima of the speed of sound of our experiments and are displayed in Fig. 5.15. The agreement between the results of the calculation and the experimental results is quite good, but we had to assume that $\Delta T = T_c - T_c^{el}$ is quite large. T_c was estimated in the experiment to be 458 K and our result of $T_c^{el} \leq 440\ K$ results in a minimum distance of nearly 4%. The difference ΔT

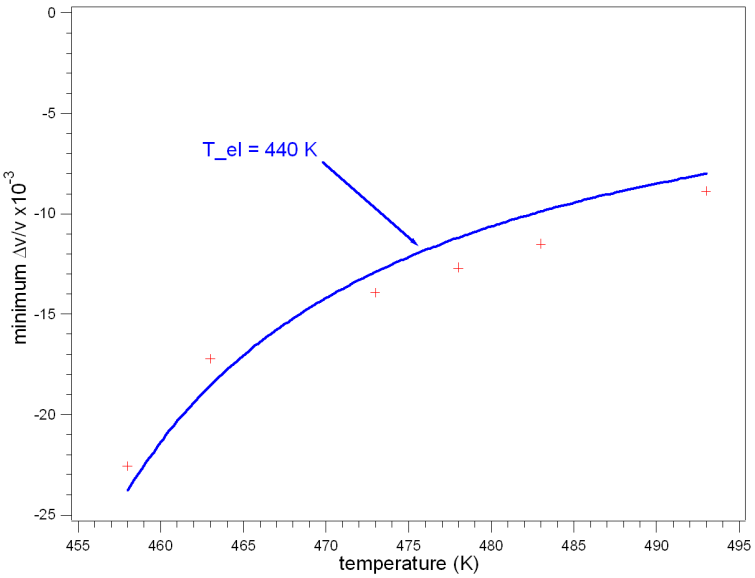

Figure 5.15: Critical behaviour of the amplitude of the minimum of the speed of sound in pressure dependent experiments above T_c.

estimated by Hassan et al. [3] was only $\approx 1.4\%$. Thus the order of magnitude is confirmed by our results, but our results propose that the effect due to the coupling to the lattice might be slightly bigger. Furthermore, it is to say that the function was obtained by using the mean field exponent 1, but due to our small number of data points slightly different exponents are not excluded and also possible.

5.5.2.4 Simulations

In the spirit of Hassan [3] we did some numerical simulations for the order parameter m and the susceptibility χ, using the critical exponents given by the mean field theory. The scaling function for the order parameter was taken as determined from the DC electrical conductivity by Limelette et al. [5]. In the simulation the reduced temperature t was varied between 0.02 and 0.1 above T_c (we did not really approach T_c because within Hassan's model the sound velocity vanishes at T_c) and the reduced pressure h was varied from -1 to +1.
In Fig. 5.16(a) the simulation for the order parameter can be found. For small relative changes of $\Delta v/v$, the profile of the speed of sound basically corresponds the negative susceptibility χ. From the calculated order parameter of Fig. 5.16(a) the susceptibility was calculated using $\chi = h^{\frac{1}{\delta}-1}\left(\frac{1}{\delta}f(x) + xf'(x)\right)$ now. The results can be found in Fig. 5.16(b), which is in qualitative agreement with the relative change in the sound speed which could be observed by us. The height in the anomaly decreases quickly with increasing temperature while the width of the

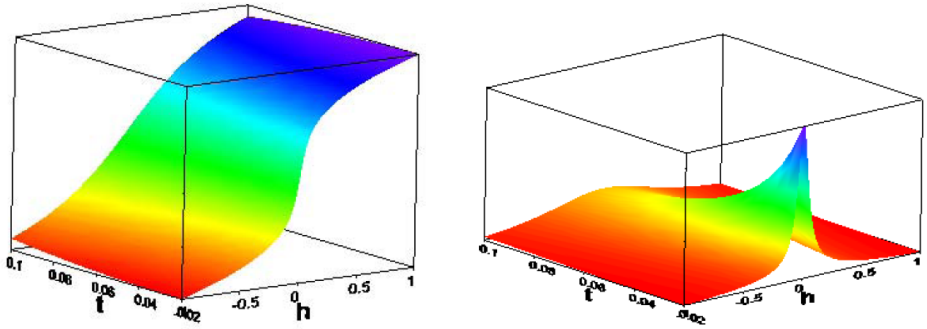

(a) Simulation for the order parameter m (b) Simulation for the susceptibility χ

Figure 5.16: Simulation of the evolution of the order parameter m and the susceptibility χ with the reduced temperature t and the reduced pressure h.

critical phenomenon increases.
In the next step the sound speed was calculated and is displayed in Fig. 5.17 to

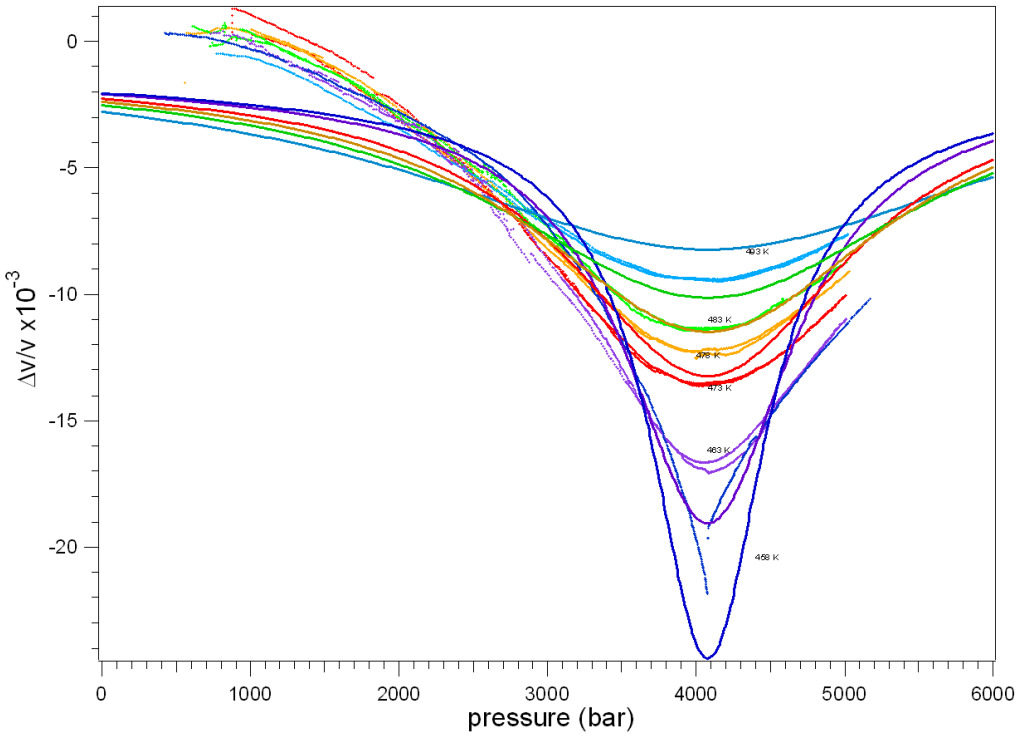

Figure 5.17: Comparison of the critical behaviour of the sound velocity above T_c with the simulations.

allow comparison between the results of our simulations and the data from the

experiments. The simulations are constructed in the way that they reach zero in infinite distance from the transition. In general our experimental data is quite good reproduced by these simulations, but some clear differences have to be mentioned. For example the critical decrease of the speed of sound at the lowest temperature is in the simulations larger and for the highest temperature smaller as indicated in our experiments.
Reasons for the discrepancy between the simulations and our experimental results could be that we could not estimate the critical exponents by ourselves, but we had to use the exponents obtained from the electrical conductivity.
One could imagine that further measurements, as for example a temperature dependent measurement at p_c, could allow us to determine γ by ourselves. But due to experimental difficulties and the very limited time of this thesis, it could not be successfully carried out until now. In the near future this will be tried again and, if successful, will perhaps allow us to obtain a more realistic simulation of the speed of sound.

5.6 Conclusion

Within this work we were able to successfully construct, test and use a new experimental set-up for ultrasonic measurements at high temperatures at continuously variable pressures up to 6000 bar. Although the main experimental task of this thesis is difficult due to the extreme sensitivity of this method to smallest cracks in the sample, it was possible to obtain a more or less complete overview of the development of the sound velocity accompanying this transition. At least, a qualitative analysis could be taken out and showed good agreements to the data in the literature.
In a measurement of pure V_2O_3, which at all accessible temperatures is in the metallic phase, we could show a clearly different behaviour with pressure for different temperatures and conclude from this the increasing width of the critical region when the temperature was increased towards T_c.
The same effect could also be found in measurements of chromium doped V_2O_3 at different temperatures. However, the data for low temperatures did not show any sign of a critical behaviour and were in qualitative agreement with the results of the literature [85]. With increasing temperatures the depart from the behaviour in the literature started gradually at lower pressure and the critical effect became bigger.
Afterwards, we were able to show that the transversal mode of the speed of sound does not show any critical behaviour when approaching the transition with pressure. But on the other hand it is much more sensitive in temperature dependent experiments, which is probably an effect of the coupling of this mode to the

low temperature transition to an AFI phase, which is accompanied by a structural change. This is also in good agreement with the behaviour reported in the literature [83, 81]. From this we were able to conclude self-consistently in the framework of the Landau theory that the order parameter is a scalar value and though in the high temperature of V_2O_3 no symmetry breaking occurs.
Within the experiments at temperatures around and above $T_c$we could qualitatively confirm the predictions of Hassan et al. [3], who calculated the disappearance of the sound velocity at the critical point. We were able to observe a change in the relative sound velocity of more than 2 %, which is for this hard material suprisingly high. Further we could show the increase of the width of the critical region with temperature above T_c while the amplitude of the dip decreases.
Further we were able to approximate the amplitudes of the minima of relative change of the sound velocity with a function derived from the critical behaviour of the electronic response function with temperature. Using the mean field exponent $\gamma = 1$ it was possible to reproduce the experimental data by using a divergence temperature T_c^{el} of the electronic contribution to the effective stiffness of 440 K or less. We were able to show that the relative shift of the transition temperature due to coupling to the lattice is with $\Delta T_c/T_c \approx 3.5\%$ in the order of magnitdue of the theoretical predictions. Nonetheless, our value is a bit higher.
Numerical simulations of the order parameter and the susceptibility allowed us to describe our findings qualitatively.

Chapter 6

The thermoelectric power

6.1 Classical definition of the Seebeck coefficient

Regardless to the fact that the thermopower of a couple (compare chapter 4) implies the difference in the response of two distinct metals to a temperature gradient, it is possible to define the absolute thermopower S as a physical property of a material, by the relation:

$$E = S\nabla T, \tag{6.1}$$

where E is the electrical field in the material and ∇T a temperature gradient. Since E and ∇T are vector quantities, S is generally a tensor. This equation represents the fact that the carriers in the hot end of the sample have a higher kinetic energy than the ones on the cold end. This higher energy causes the "hot" carriers to be more distributed within the sample, which causes a departure from the equilibrium as the carrier density on the cold end increases until an electrical field leads to an equal flow of "cold" carries towards the hot end.
In order to clarify this situation and gain information about the sign of S a sketch of the classical explanation of thermal diffusion is given in Fig. 6.1. In this example electrons are used as carriers, which results in the electrical field and the temperature gradient having the same direction. From the relation $E = -\nabla U$ follows that:

$$-\nabla U = S\nabla T, \tag{6.2}$$

which means that for electron as carriers the sign of the measured thermopower will be negative.
The equation of the charge current can be written as [93]:

$$j = L_{11}E + L_{12}\left(-\nabla T\right), \tag{6.3}$$

where j is the electrical current density and L_{ij} are 3×3 tensors.

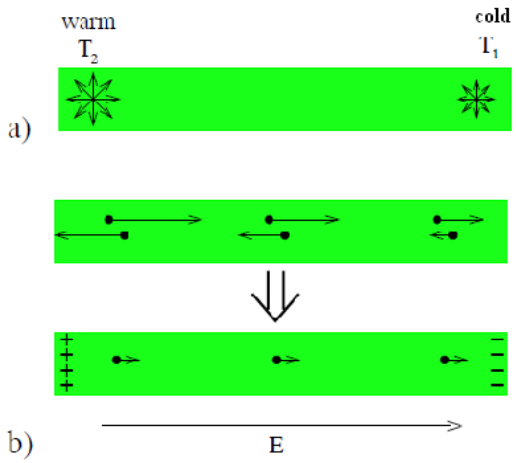

Figure 6.1: Sketch of the classical explanation of thermal diffusion. In this sketch the carriers are electrons. a) The absolute value of the average velocity of electrons in the warm end of the sample is higher. b) One dimensional model: The electrons coming from the hot end move faster than the ones coming from the cold end in every segment. The addition of the velocity vectors illustrates that this results in an effective diffusion towards the cold end. In this way an electric field arises that disrupts the diffusion current.

In the case of the absence of an electrical current $j = 0$ follows with Eq. 6.1:

$$S = \frac{L_{12}}{L_{11}}. \tag{6.4}$$

For an uncorrelated degenerate Fermi gas, the thermopower can be related to the transport coefficients and in the relaxation time approximation ([94, 95]) it can be written as:

$$S = \frac{K_1}{eTK_0}, \tag{6.5}$$

and the electrical conductivity is given by:

$$\sigma = e^2 K_0. \tag{6.6}$$

The generalised transport coefficients K_n are defined as:

$$K_n = -\frac{1}{3}\int 2\tau_k v_k v_k \left(-\frac{\partial f_0}{\partial \epsilon}\right)|_{\epsilon=\mu} (\epsilon(k) - \mu)^n \, d^3k, \tag{6.7}$$

where τ_k is the momentum dependent scattering time, v_k the velocity, ϵ_k the energy, f_0 the Fermi-Dirac distribution function, and μ is the chemical potential.

For strongly correlated systems the electronic contribution can be expressed with equivalent expressions involving integrals over the spectral densities [96].
If the energy-dependent scattering is neglected we can roughly approximate the behaviour of the thermopower in the metallic region with the thermopower of a free electron [97]:

$$S = -\frac{\pi^2 k_B}{6e}\frac{T}{T_F}. \tag{6.8}$$

The actual sign in this equations depends on the dominant carrier type.
In the non conducting phase the thermopower can be described in terms of a semiconductor. For a conventional broad band semiconductor the thermoelectric power according to Mott et al. [98] is given by:

$$S = \frac{k_B}{e}\left(\frac{E_c - E_F}{kT} + \frac{5}{2} + r\right), \tag{6.9}$$

where $r = d(ln\tau)/d(lnE)$ and τ is the time of relaxation and $E_c - E_F$ is the activation energy to the conduction band. According to this formula the thermopower should decrease linearly with increasing temperature.
The absolute values of semiconductors are usually larger by a factor of 100 than the ones of metals. This can be understood from Eq. 6.5 and Eq. 6.6, which show that a high electrical conductivity leads to a smaller Seebeck coefficient. On the other hand the transport coefficient K_1 represents the asymmetry between electrons and holes. Hence K_1 will be larger for a semiconductor where the Fermi level always lies in the gap than in a metal where the Fermi level is within the conduction band an thus asymmetries are mostly averaged out.

6.2 Thermopower of V_2O_3 in the literature

In order to compare our results with existing data for the Seebeck coefficient S, we will firstly review some important results in this field.
Kuwamoto et al. [99] performed a temperature dependent measurement of the Seebeck coefficient of $(V_{1-x}\ Cr_x)_2O_3$ alloys with different Cr concentrations. Their results are shown in Fig. 6.2, where the Seebeck coefficient (in this figure abbreviated by α) was estimated for doping concentrations of x = 0, 0.006, 0.010, 0.015 and 0.030 in the temperature range between 200K and 500K. The different doping concentrations lead to 3 different characteristic curves. For pure V_2O_3 (x = 0) the Seebeck coefficient changes very little over the whole observed temperature range and its value is of the order of $+10$ μV/K. For the highest chromium concentration, x = 0.030, S is decreasing over the whole temperature range (with increasing temperature). Its value decreases from approximately 450

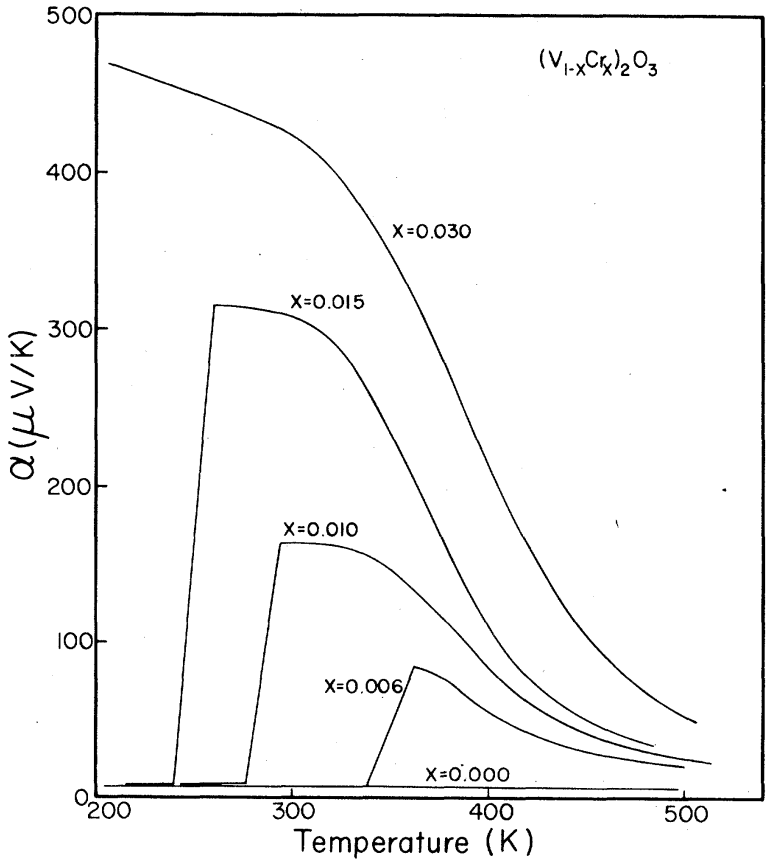

Figure 6.2: Seebeck coefficient (here α) versus temperature for several different doped $(V_{1-x}\ Cr_x)_2O_3$ alloys [99].

μV/K at 200K to less than 50 μV/K at 500 K. For intermediate doping concentrations ($0.006 \leq x \leq 0.015$) and at low temperature (200 K), the Seebeck coefficient has the same value as for pure V_2O_3. As the temperature is raised, S rapidly increases (nearly to 200 μV/K for x = 0.01), before it decreases again to a value of some $+10$ μV/K above 500 K.

It is to note that the Seebeck coefficient is positive in all doping concentrations and temperatures. This indicates that the dominant carrier type in $(V_{1-x}\ Cr_x)_2O_3$ are holes.

These observations confirmed earlier studies by Sinha et al., who also reported a small positive Seebeck coefficient at high temperatures near +15 to +20 μV/K for a small amount of Cr doping (x < 0.030) [100].

In Fig. 6.2 the behaviour of the metallic phase (e.g. pure V_2O_3) is only approximated with a straight line. In Fig. 6.3 an experiment done by Austin et al. [101] on pure V_2O_3 shows the thermopower in the temperature range between 50 K and

800 K. In this graph S is plotted against the inverse temperature $1/T$ (on the top

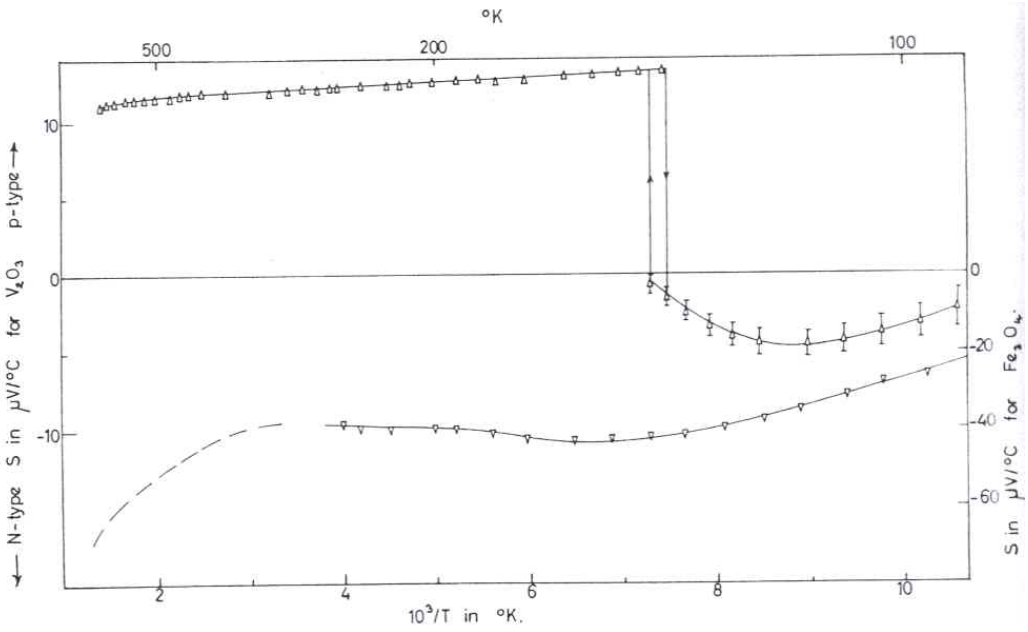

Figure 6.3: Thermopower in V_2O_3 ($\triangle$, upper line) versus inverse temperature, left scale. The temperature gradient is perpendicular to the hexagonal c-axis. Right scale: Thermopower of Fe_3O_4 (∇, lower line) [101].

scale the corresponding temperatures are given). At low temperatures the transition to the AFI phase takes place. This is of no interest to us and so only the results above the transition will be taken into account. In the metallic phase S has values of 11-13 μV/K. S increases over the whole temperature range monotonically with decreasing temperature, but its total value is only changing very little.
These are the only results for this sample system; no pressure dependent measurements of V_2O_3 Seebeck coefficient are available.

6.3 The heat conductivity

According to the $Wiedemann - Franz\ law$[1], the ratio between thermal conductivity κ and electrical conductivity σ is nearly proportional to the temperature T

[1]The Wiedemann-Franz law is only a good approximation, if energy is conserved in a good approximation. This requires that the energy change of each electron in a collusion is small compared with k_BT. Subsequently, the Wiedemann-Franz law is generally well obayed at high and low temperatures. In the intermediate temperature range from roughly ten to a few hundred K, where inelastic elastic collusions can produce energy losses of the order of k_BT, the approximation fails.

in a metal. This empirical law was found by G. H. Wiedemann and R. Franz in 1853 [102]:

$$\frac{\kappa}{\sigma} = LT, \tag{6.10}$$

where L is a constant and is referred to as the Lorenz number. Subsequently, it should also be possible to observe a change in the thermal conductivity at the MIT. As the temperature gradient in the sample and the voltage difference between both ends of the sample are accumulated at all times for our measurement of the Seebeck coefficient we also tried to calculate the thermal conductivity from the acquired data.
The possibility to extract information about the thermal conductivity from the data obtained during the measurement of the thermoelectric power is also discussed in this section. First we discuss under which conditions this is theoretically possible, then the experimental data is shown, and finally the resulting conclusions will be drawn.

6.3.1 Simultaneous measurement of electric thermopower and heat conductivity

In this section we will point out why and under which circumstances it is possible to measure the electrical thermopower and the heat conductivity at the same time. We consider the sample as a thermal conductor between the bath at temperature T_0 and the heater at temperature T_1. A heater current $I(t)$ is applied and the amount of heat per unit time $\dot{Q}$ accumulated at the heat source can be written as the difference between the power dissipated by the heater and the heat conducted by the sample:

$$\dot{Q} = C(T_1)\dot{T}_1 = R(T_1)I^2(t) - K(T_1 - T_0), \tag{6.11}$$

where $C(T_1)$ is the heat capacity of the heat source, $R(T_1)$ is the resistance of the heater and $K(T)$ is the thermal conductance of the sample.
When the temperature of the bath is held constant and a constant current I_0 flows through the heater, the steady state will be reached after a sufficiently long time; this means $\dot{T}_1 = 0$ and in this case the following expression for the thermal conductance can be obtained from 6.11:

$$K(\bar{T}) = \frac{R(T_1)I_0^2}{T_1 - T_0}. \tag{6.12}$$

If the temperature of the bath is changed slowly, the system will no longer return to a steady state and the temperature at the heat source T_1 will be an oscillating function of time.In this case equation 6.11 has to be solved.

As this equation is not linear in general and it proves very difficult to solve it analytically, several approximations are introduced to linearise it.
Due to the small temperature gradient ΔT, T_0 and T_1 are similar and if C(T), R(T) and K(T) are smooth functions of T, using T_0 instead of T_1 as arguments of this functions, will only result in a small error. If the drift of the bath is slow compared to the time scale used to modulate the current it is possible to consider T_0 as constant for the smaller time scale. Equation 6.11 can be solved with a time independent T_0 and the time dependence restored afterwards. This approach is called *the adiabatic approximation.* With these assumptions 6.11 becomes a linear equation with constant coefficients:

$$\dot{T}_1 - \dot{T}_0 = \frac{R}{C} I_0^2 - \frac{K}{C}(T_1 - T_0) - \dot{T}_0, \tag{6.13}$$

where $\dot{T}_0$ had beensubtracted from both sides of the equation.
If the temperature of the bath varies at a constant rate the higher order derivatives of T_0 can be neglected and $\Delta T(t)$ is replaced in the following manner. A smooth curve is drawn through the maxima of the oscillations and another through the minima. The amplitude of this curve can then be defined as the difference of these two envelope curves. The maxima occur at $t = n\tau$ with n even and the minima with odd n and τ corresponds to a half-period of the pulsed heater current. For the peak-to-peak amplitude of the signal we get:

$$\begin{aligned} \Delta T_{pp} &= \frac{RI_0^2}{K}\left(\frac{1 - e^{-(K/C)t}}{1 + e^{-(K/C)t}} - 1 + \frac{1 + e^{-(K/C)t}}{1 + e^{-(K/C)t}}\right) \\ &= \frac{RI_0^2}{K}\tanh\left(\frac{K\tau}{2C}\right). \end{aligned}$$

This equation relates the measured signal, e.g. the amplitude of the temperature gradient, to the thermal conductance K. This can be transposed to the following form:

$$K = \frac{RI_0^2}{\Delta T_{pp}}\tanh\left(\frac{K\tau}{2C}\right). \tag{6.14}$$

If all the other parameters are known as functions of temperature, this equation can be easily solved by numerical iteration. Since τ and I_0 are controlled parameters they can be chosen at will and the resistance of the heater $R(T)$ is a function of temperature, which in our experimental set-up is measured all the time. The heat capacitance of the heater should also be known as a function of temperature.
In the limit of $K\tau/2C \gg 1$, i.e. for τ much bigger than the relaxation time of the system C/K, it can be approximated $\tanh(K\tau/2C) \approx 1$ and the amplitude of the signal is independent of τ and C. In this steady state limit the thermal conductance

K is independent of C and is given by:

$$K = \frac{RI_0^2}{\Delta T_{pp}}. \tag{6.15}$$

To obtain the thermal conductivity κ of the sample, the conductance given by equation 6.15 has to be multiplied by the geometric factor of the sample, the cross-section A divided by the length l:

$$\kappa = K\frac{l}{A}. \tag{6.16}$$

When we now introduce $P_{heater} = RI_0^2$ we get for the thermal conductivity:

$$\kappa = \frac{P_{heater}}{\Delta T_{pp}}\frac{l}{A}. \tag{6.17}$$

For a more detailed description see [103].
To summarise, the required conditions to perform a simultaneous measurement of thermoelectric power and heat conductivity are:

a) the temperature gradient ΔT in the sample has to be small with respect to the mean value of the temperatures at both ends of the sample $\bar{T}$;

b) $C(T)$, $R(T)$, and $K(T)$ have to be a smooth function of T;

c) the bath temperature T_0 should drift slowly with respect to the time scale the current is modulated;

d) the half period of the pulsed current has to be much greater than the system relaxation time C/K.

As already mentioned above, the temperature gradient ΔT in our experiment was held between 0.5 K and 1.5 K and the temperature of the bath was at minimum 300 K, so that the relation $\Delta T = 1.5K \ll 300K = (T_0 + T_1)/2$ was well satisfied and condition a) was fulfilled at any time. Furthermore, the speed of the drift of the bath temperature T_0 was controlled by us and set to a sufficiently low drift speed that assured that also the condition c) was fulfilled. In Fig. 4.5 it is easy to see that the temperature gradient ΔT and the voltage difference ΔV are both well satisfied within the heat pulse. This allows us to conclude that the half period of the pulse is much much bigger than the systems relaxation time and subsequently also condition d) is fulfilled.
Finally, the validity of point b) has to be tested.

6.3.2 Experimental results

In order to test if we can see a change in the thermal conductivity at the MIT, in this paragraph we will take a look at the experiment where the biggest change at the transition occurred, i.e. where the MIT was crossed at the lowest temperature. In Fig. 6.4 the transition was crossed at low temperatures, i.e. 338 K. At this relatively low temperature the transition should have a very discontinuous character and a change in the thermal conductivity should be observed easily. This was the only experiment at such low temperatures as we suspected harm to the sample by crossing the transition at low temperatures. This fortunately did not occur as we verified afterwards. From this we concluded that the thermopower measurement is less prone to small cracks in the sample.
In Fig. 6.4(a) S is plotted against pressure. The transition occurred at $\approx 2300\ bar$ and S fell quite violently from approximately $180\ \mu V/K$ before the transition to less than $20\ \mu V/K$ after the transition, within few bars.
The evolution of the peak-to-peak difference of the measured voltage difference with pressure can be found in 6.4(b). At the transition at approximately 2220 bar ΔV_{pp} becomes almost ten times smaller (from $\Delta V_{pp} \approx 100\mu V$ to $\Delta V_{pp} \approx 10\mu V$) while the sample transits to the metallic phase. This factor is nearly the same as the change in the thermopower S.
In Fig. 6.4(c) the characteristics of the amplitude of the peak-to-peak temperature difference between both ends of the sample can be found. And indeed the difference changes by more than 10 % (from 0.58 K before the transition to 0.50 K after the transition). In other words, the temperature difference became smaller when the sample crossed from the insulating to the metallic state. This is expected as the thermal conductivity in a metal is larger. On the other hand the relative variation of ΔT_{pp} at the transition is small compared to the one of ΔV_{pp}.
To compare these findings with the actual power of the heater used to establish this temperature gradient, in Fig. 6.4(d) the variation of the dissipated power at the heater is plotted against the pressure. P_{heater} shows a big charge at the transition and its value falls from $5.8\ mW$ to $5.2\ mW$ while crossing the transition. An explanation for this could be that the sample attached to the heater acts as a thermal contact between the temperature of the bath T_0 and the heater T_h. The sample in the insulating state represents a thermal resistance between the two, while the metallic sample allows a good thermal transfer between the two. This good thermal transfer will adjust the temperature of the heater to the one of the bath, which is a bit lower. The resistance of the metallic heater is decreased resulting in a lower dissipated heater energy when the sample is in the metallic state.
Finally the thermal conductivity was calculated via Eq. 6.17 using $l = 5\ mm$ and $A = 0.2\ mm^2$ for the dimensions of our sample and the results are shown in Fig. 6.4(e). It is easy to see that apart from the noise only a very small trend or change

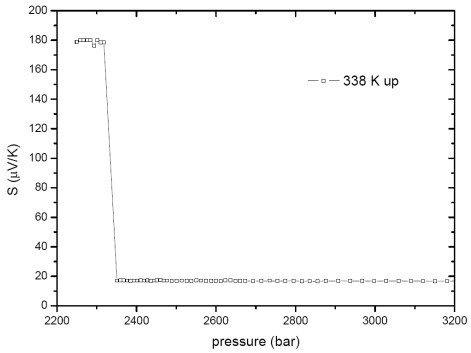

(a) Seebeck coefficient at 338 K plotted against pressure

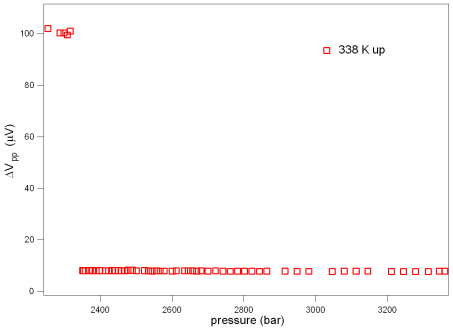

(b) Voltage difference V_{pp} between both ends of the sample vs pressure

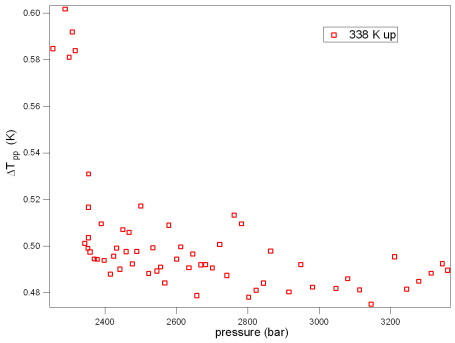

(c) Temperature gradient T_{pp} between both ends of the sample vs pressure

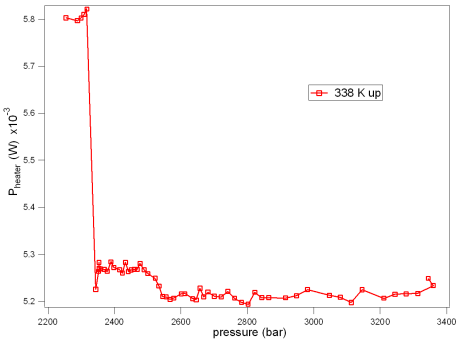

(d) Dissipated energy at the heater

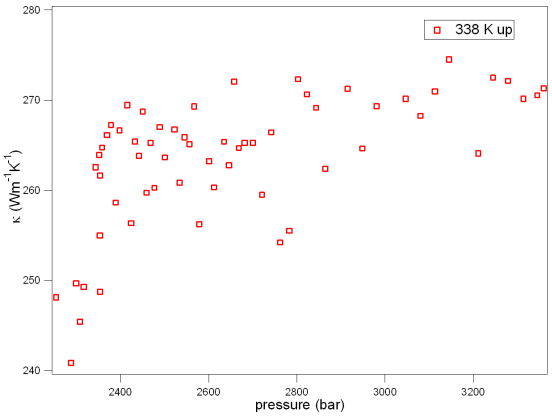

(e) Calculated thermal conductivity at 338 K against pressure

Figure 6.4: Comparison of S, the peak-to-peak voltage difference, the temperature gradient along the sample, the energy dissipated at the heater and the resulting conductivity κ at 438 K in the pressure range between 2200 and 3400 bar.

in κ can be identified with the MIT. The values of $\kappa \approx 250\ Wm^{-1}K^{-1}$ in the insulating state and $\kappa \approx 270\ Wm^{-1}K^{-1}$ in the metallic state are much too high compared to the value in the literature for pure V_2O_3 ($\kappa \approx 6\ Wm^{-1}K^{-1}$ at 400 K [104]).
These differences now have to be explained. A first point is that in order to be able to apply pressure our experimental set-up is situated in a pressure cell that is filled with the pressure liquid (in our case Isopentane). The situation is illustrated in Fig. 6.5. It becomes clear that because our heater is in thermal contact with the

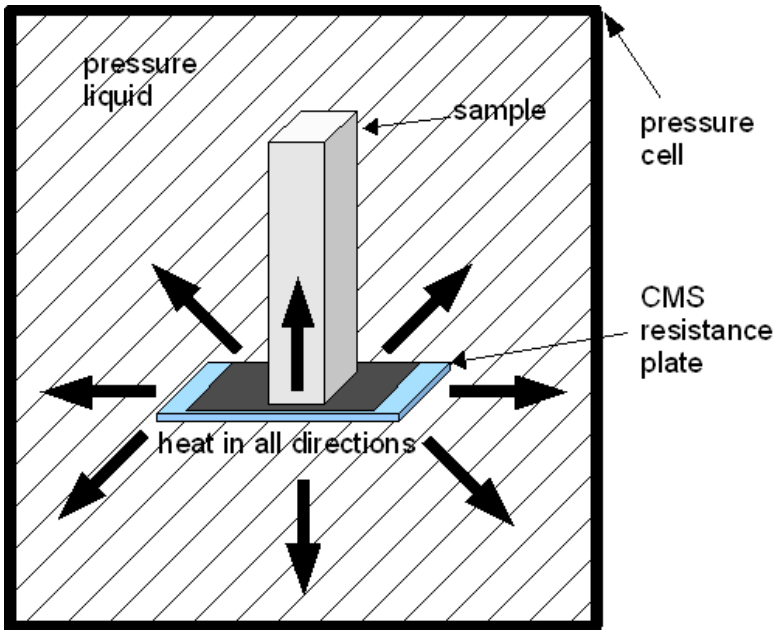

Figure 6.5: Scheme of the distribution of the heat energy from the heating resistance in the pressure cell used for measurements of the thermoelectric power and thermal conductivity.

pressure liquid, most of the energy of the heater will heat the isopentane and not the sample. The thermal conductivity of isopentane is given in the literature as $\kappa \approx 0.1 Wm^{-1}K^{-1}$ at 300 K [105]. In principle our measured thermal conductivity should be a mixture of that of our sample and that of the oil: $\kappa_{eff} = \alpha\kappa_{sample} + \beta\kappa_{oil}$, where α and β are the ratios of the cross sections of these two. Consequently the resulting κ_{eff} should be between 6.0 and 0.1, from which our result lies even further.
It becomes clear that another more systematic error led to the wrong results. The problem is that we do not know what percentage of the dissipated energy arrives at the sample (via the sample and via the isopentane), but it is possible to back calculate, from the ratio of our result to the value in the literature, to the amount

of energy sent trough the sample. In our case an effective heater power of only about 2% of the nominal value would lead to approximately correct results.
The jump in the heater power at the transition (compare Fig. 6.4(d)) is another item in conflict with the theoretical assumptions, because directly at the transition $R(T)$ is not a smooth function of T as demanded in point b).
Ultimately attempts to measure the thermal conductivity and the electric thermopower at the same time failed. We did see a jump in κ at the transition, but we could not estimate a correct value for the thermal conductivity. But most of the requirements to be able to measure thermal conductivity and the thermoelectric power simultaneously were quite well fulfilled and our failure is due to the unknown heater energy which finally arrives in the sample. The problem is to measure κ in a pressure cell with a pressure liquid. In principle it is possible to recalculate from the values of a measured sample with a known heat conductivity the percentage of the heat going into the sample, but for this pressure and temperature dependent measurements with a well characterised sample would be needed.

6.4 Results for the Seebeck coefficient

In this section the results of the thermopower experiments will be presented. Starting with two experiments upon cooling from room temperature under a low vacuum on the different samples in order to be able to estimate the influence of the differences due to slightly different preparations of the sample.
Afterwards, different temperature dependent experiments in the pressure regions where the sample is insulating will be presented. This will allow us to gain information about the behaviour of the sample system in the insulating phase.
Subsequently, temperature experiments in the metallic pressure region will be shown that will allow us to gain information about the evolution of the Fermi energy. Thereon, data where the transition was crossed upon heating will be presented.
Finally several pressure dependent experiments below and above the critical temperature will be used to complete the picture of the evolution of the thermoelectric power S at the Mott transition in V_2O_3.

6.4.1 Temperature dependent experiments

In this section several experiments will be presented in which the pressure was kept constant and the temperature was changed slowly. The temperature was changed using the temperature controller at a constant rate of 0.1 K/min.

6.4.1.1 Cooling at ambient pressure

In order to test our experimental set-up at the very beginning we tested our sample not inside the pressure cell, but in a nitrogen dewar. For this experiment the sample was put under a low vacuum ($\approx 10^{-2}\ bar$). This was done in order to avoid to reach thermal equilibrium too fast and to keep the cooling rate of the temperature of the sample sufficiently low.
We tested this for two different samples and the findings are plotted in Fig. 6.6. With both samples we started at room temperature and then went down with tem-

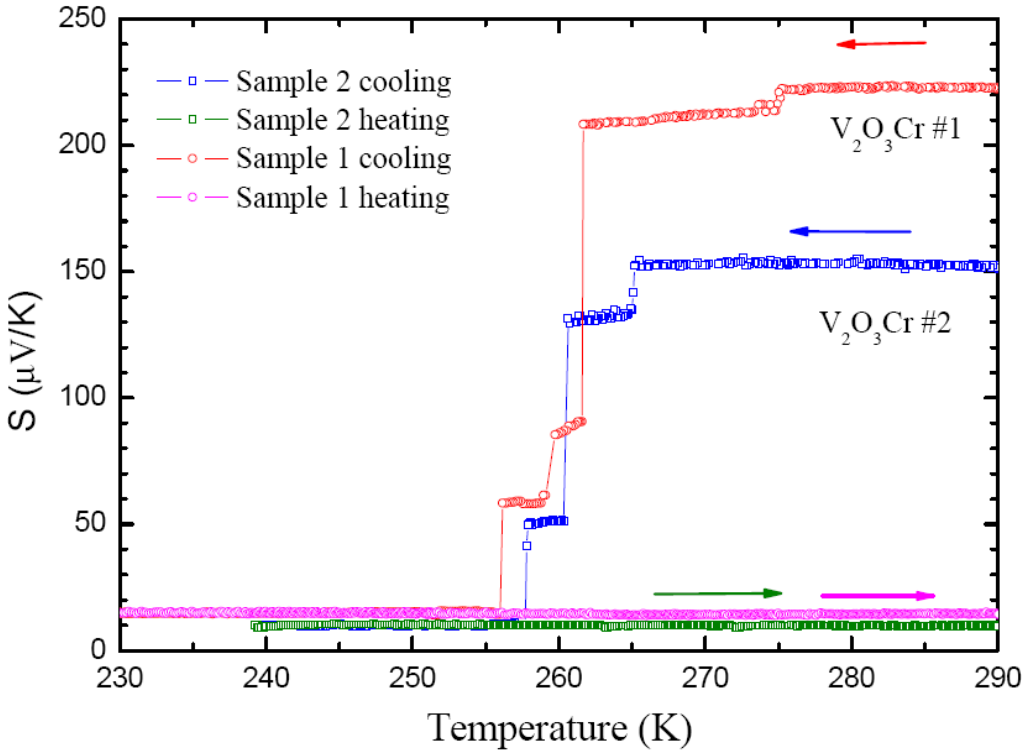

Figure 6.6: The Seebeck coefficient in vacuum in the temperature range between 290 K and 230 K for two different samples is shown.

perature to 230 K and 240 K. The values of S in the insulating phase (250 $\mu V/K$ for sample 1 and 150 $\mu V/K$ for sample 2) are quite different for both samples.
Another difference between the two samples is the temperature where the transition takes place. Between the start and the end of the transition there is a difference of nearly 5 K for the two specimens. Both samples cross the transition in several steps before the bulk samples become metallic. This is quite typical for a first order phase transition where "time effects" dominate.
Afterwards both samples were heated back to room temperature and also in the

absolute values of S in the metallic phase a small difference can be seen, but both samples show nearly constant values between 10 $\mu V/K$ and 15 $\mu V/K$ respectively.
After dismounting the experiment both samples, as expected, showed big cracks and could not be used for further measurements.
It is to mention that the measured Seebeck coefficient is positive at all temperatures, which confirms the existing results in the literature [99, 100, 101] and indicates holes as the dominant carrier type.
Coming back to the different values of S for the two specimens in Fig. 6.6, some possible explanations for the variation have to be mentioned. For example the contacts of the thermocouple used to measure the temperature gradient within the sample have to be electrically insulated, but to deliver the right values for ΔT they have to be at the same time in thermal equilibrium with the sample. Achieving this proved to be quite difficult and might be responsible for the differences. Another crucial point in the sample preparation is that the contacts used to estimate ΔT and ΔV have to be at the same level of the sample. If two contacts are a bit nearer together the resulting ratio of the two values, i.e. S, will also be wrong.
Thus it is important to note that all the experiments presented in the following sections were realised with the same sample and highest attention was paid to avoid the systematic errors listed above. But even if there was a small systematic error, only the absolute values of S would be slightly wrong by a constant factor. The obtained results are still comparable to each other, because all measurements were performed with the same set-up and the same sample and subsequently would have the same small systematic error.

6.4.1.2 The insulating low pressure region

Again to protect the sample from irreversible damage it was our aim to cross the MIT only at higher temperatures. So naturally the first experiments were performed upon heating the sample at pressures below p_c.
In Fig. 6.7 the results of the temperature dependent experiments in the range between 290 K and 493 K for several different pressures in the insulating region of the phase diagram can be found.
The first two experiments at 500 bar and 1000 bar were carried out only up to 473 K and from 400 K these two measurements were very noisy due to the change in the heater resistivity with temperature. For the later experiments a higher heater current was used to establish the thermal gradient along the sample and no problem with noise is visible.
At low temperatures in all three experiments going down to room temperature a saturation with decreasing temperature in S is visible. This behaviour is expected due to the second transition at low temperatures. The apparent decrease in S for

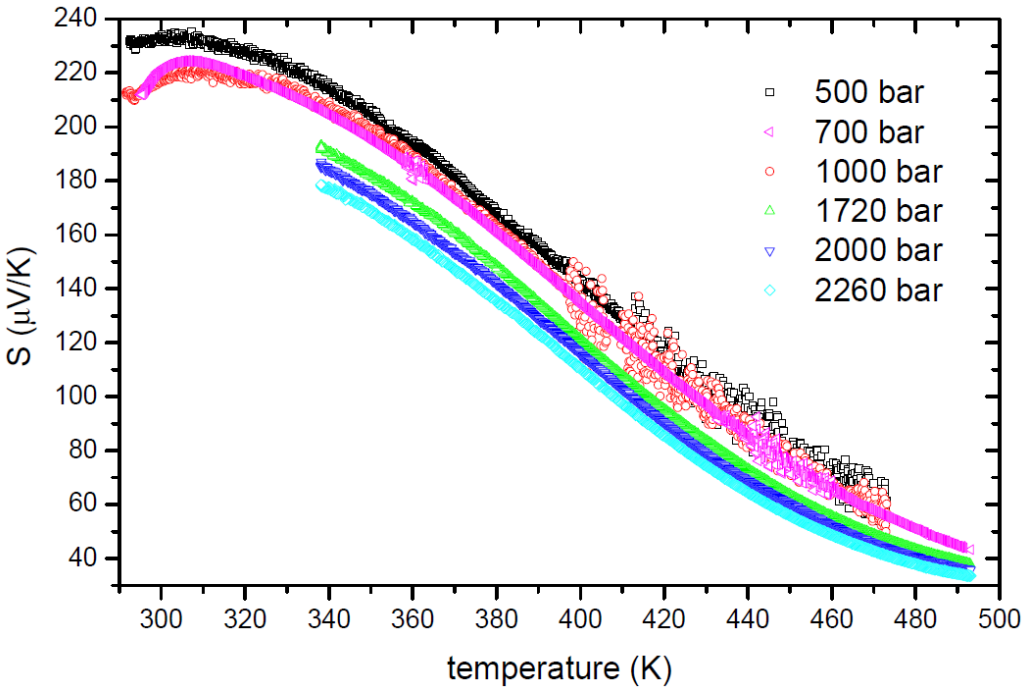

Figure 6.7: The Seebeck coefficient in the insulating state at various pressures between 500 bar and 2260 bar in the temperature region between 290 K and 493 K.

500 bar and 700 bar is probably the signature of the upcoming phase transition, where small already metallic fractions inside the sample with a much smaller Seebeck coefficient lead to a weakly decreasing global value of S.

Afterwards the curves are parallel for all three experiments and decreasing with pressure. Over a large temperature range between 340 K and 440 K the decrease seems to be nearly linear before the drop becomes much smaller for the highest measured temperatures. In total the value of S decreases from approx. 220 $\mu V/K$ at 300 K to 40 $\mu V/K$ at 493 K. This behaviour can be compared to Fig. 6.2. The nominal doping of our samples is 1.1 $\%$ and because of this our results should be comparable to the graph for x = 0.010 of Fig. 6.2. Indeed our curves are very evocative of the one given in the literature. The values of S are in good agreement with the ones found by Kuwamoto [99] for this doping and the curves are of the same shape. In total it can be said that our results are in good agreement with the ones already presented in the literature.

Three more experiments at higher pressures are added to the graph that allow the analysis of the evolution of S near to the transition pressure. Because crossing the MIT at low temperatures should be avoided the measurements were only done

down to 338 K. The curves are very similar to those at lower pressures with values a bit lower and decreasing with increasing pressure. This is also expected from Fig. 6.2, because higher pressure corresponds to a lower amount of chromium doping. At higher temperatures all graphs seem to come closer to each other, which is also in good agreement with the existing results.
Altogether, the results of our measurements in the insulating phase confirm very well the ones available in the literature [99].

6.4.1.3 The metallic high pressure region

A number of temperature dependent experiments in the metallic region of higher pressures in the same temperature region (290 K to 493 K) were carried out. This was done to study the behaviour of S in the metallic phase in the pressure range between 3333 bar and 5750 bar.
The different curves can be found in Fig. 6.8. Again there is a quite particular be-

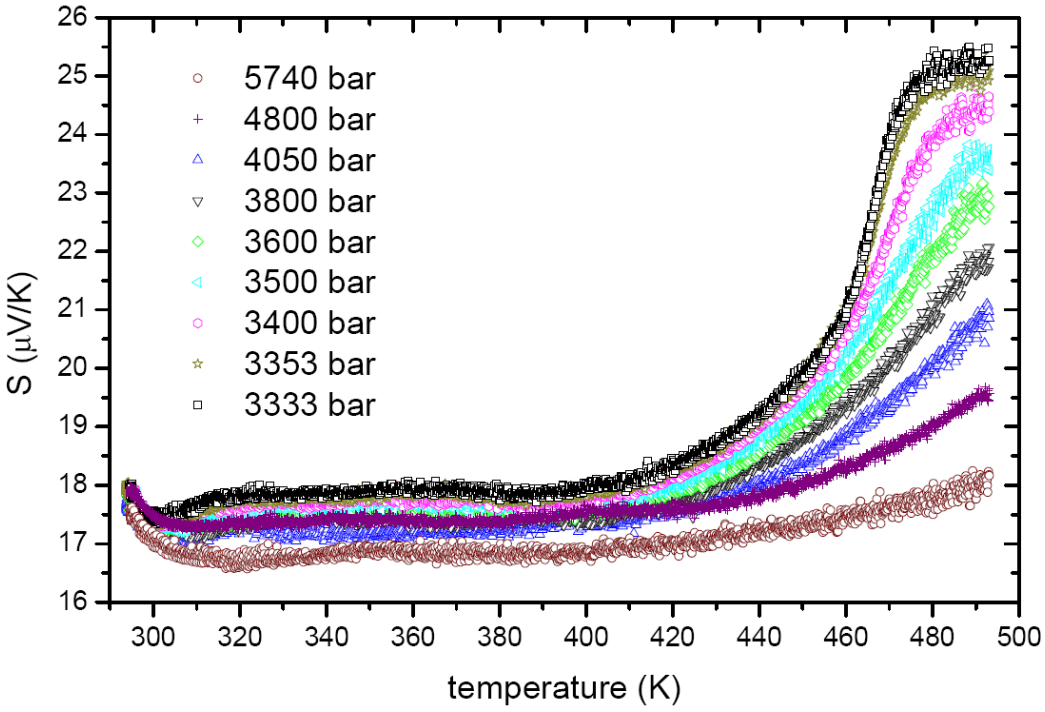

Figure 6.8: The Seebeck coefficient between 3320 bar and 5740 bar in the temperature region between 290 K and 493 K.

haviour at lower temperatures visible in all measurements. But in contrast to Fig. 6.6 we see a rise in S at the lowest T. Due to the lack of an upcoming transition to an insulating phase in this pressure region until much lower temperatures (180 K),

this cannot be taken into account to explain these characteristics and they could be assigned experimental uncertainties.
It is astonishing to see that after the anomaly at low temperatures over more than the first 100 K the curves are almost parallel straight lines at all pressures with values for the Seebeck coefficient between 17 and 18 $\mu V/K$. Only at around 420 K the values of S do begin to rise significantly with temperature and it becomes possible to identify differences between the curves of different pressures.
In general the further the sample is in the metallic region the more S stays nearly constant at small values. For the highest pressure 5740 bar S rises very little and even for 4800 bar, although S is increasing monotonically, at 493 K it reaches only $S = 19\mu V/K$.
From 3600 bar and lower pressures, a monotonic change with temperature arises. Saturation of S at the highest temperature takes place and finally at 3320 bar it is even possible to identify a maximum in the Seebeck coefficient followed by a flat, nearly constant region.
It is very difficult to compare these results to the available data in the literature because no data of Cr doped V_2O_3 is available in the metallic phase. If we compare our findings to the results obtained in pure V_2O_3, we see in Fig. 6.2 only a flat line over the whole temperature range and in Fig. 6.3 a monotonic decrease in S with temperature that cannot be found in our data. But the increase we see at higher temperatures can be clearly attributed to the critical region of the MIT. This together with the fact that the experiment at the highest pressure shows only a very small increase of S at the highest temperatures and still is far from being in the pure metallic phase, allows speculation that a behaviour as indicated in the literature in the metallic phase would be at least also possible for our sample at higher pressures ($\approx 8000\ bar$).

6.4.1.4 Measurements in the mixed region

In this section we will take a look at the measurement in the pressure region where the MIT was crossed upon heating or cooling. At temperatures below T_c the transition is of first order and hysteresis is awaited. Therefore all measurements were performed as a cycle, e.g. S was determined during heating and cooling. Because of our very accurate estimation of the pressure in the cell we became aware that during the experiments it was somehow influenced by external conditions. Naturally the pressure in the cell changed a bit when the temperature was changed, but in some experiments the pressure increased with decreasing temperature. Because of this it was somehow difficult to control the exact pressures of the cycle and though they are not always identical, much care was taken to keep these differences as small as possible. The given pressures for the different curves correspond to the actual pressure near the critical temperature ($T_c \approx 458\ K$).

In Fig. 6.9 our results for various pressures between 3350 bar and 3100 bar in the

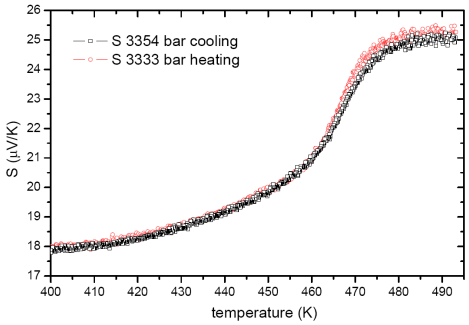

(a) 3333 bar and 3354 bar

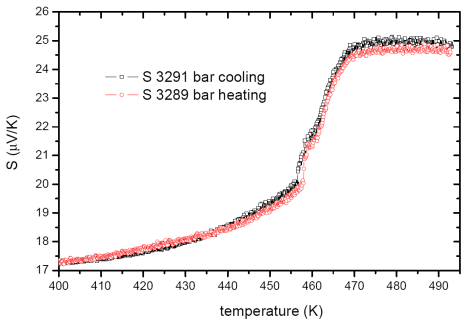

(b) 3289 bar and 3291 bar

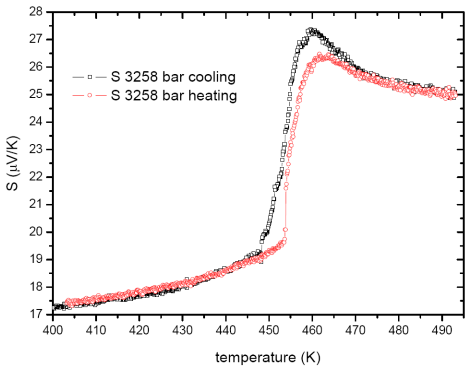

(c) 3258 bar

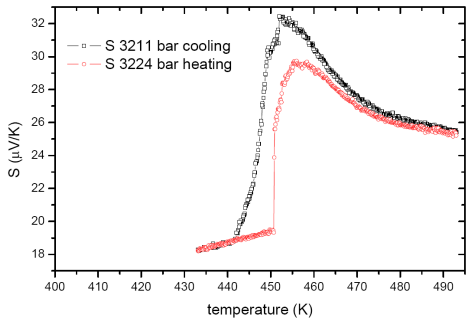

(d) 3211 bar and 3224 bar

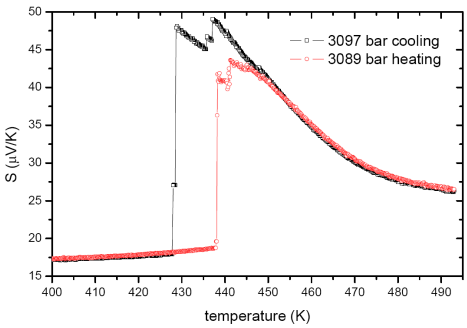

(e) 3089 bar and 3097 bar

Figure 6.9: Temperature dependent measurements between 400 K and 493 K at various pressures in the range between 3350 bar and 3100 bar. To verify if any sign of a hysteresis could be found the measurement was taken out upon heating and cooling.

region where the MIT was crossed by a change of the temperature are shown in the temperature range between 400 K and 493 K.

In Fig. 6.9(a) the results from just above the transition that were already presented in 6.8 are shown in greater detail in the high temperature region. S is increasing monotonically over the whole temperature region. At the highest temperature the slope becomes very small and S nearly saturates. The change of the slope which can easily be seen between 450 K and 480 K will be analysed below. The trends of both graphs are very similar although there is a slight difference in the pressure between the two graphs. The differences in the trends of the graphs can probably not be attributed to a hysteresis and result from the pressure difference. Furthermore the transition takes place at higher temperatures during cooling and cannot be interpreted as hysteresis. The sample is still in the pressure range slightly above p_c.
Afterwards the pressure was lowered a little bit to approach the critical pressure. In Fig. 6.9(b) S is shown for 3291 bar and 3289 bar in the same temperature region. From 400 K to 455 K both curves are nearly identically increasing with temperature. Afterwards the slope changes and S increases from 20 $\mu V/K$ at 455 K to 25 $\mu V/K$ at 470 K and stays nearly constant from there to 493 K. At higher temperatures a very small hysteresis can be diagnosed based on the small difference of the curves, but due to this small difference we are probably very near to the critical pressure p_c. Further evidence that we see a small hysteresis is that the temperatures for the MIT are higher upon heating as it is expected.
By lowering the pressure by about 30 bar the progression of the curves changes drastically. In Fig. 6.9(c) the Seebeck coefficient upon heating and cooling at 3258 bar is plotted. Even if the difference in pressure compared to Fig. 6.9(b) is only very small the differences are quite big. While the low temperature part is still similar to the one of the graph before, S reaches a maximum and starts to decrease at the highest temperatures to values of around 25 $\mu V/K$. This decrease indicates that the transition line to the insulating phase is crossed and the sample is in the insulating phase, where S decreases with increasing temperature. Here the hysteresis cannot be overlooked in the temperature range between approximately 445 K and 470 K. Upon heating S starts to increase at more than 5 K higher temperatures. The maximum value is reached some degrees higher and the maximum value itself is with 26.5 $\mu V/K$ also approximately 5% smaller then in the cooling part of the experiment (27.5 $\mu V/K$).
Subsequently in Fig. 6.9(d) the pressure is again lowered by ≈40 bar to 3211 bar respectively 3224 bar. In order to simplify the comparison of the different experiments, the temperature scale is kept constant. A first distinctive feature is the linear increase of S in the temperature region below the transition compared to the more rounded curves at higher pressures. Next the hysteresis becomes more accentuated as the difference between initiation of the transition, the difference of the temperature where the maximum values are reached, and the difference of the total values of these maxima (33 $\mu V/K$ respectively 30 $\mu V/K$) are bigger

than in the previous graph. After reaching the maximum S decreases in both measurements to a final value of around 25 $\mu V/K$.
Finally, the results for the lowest pressure where the MIT was crossed in temperature dependent measurements at 3100 bar are shown in Fig. 6.9(e). Experiments crossing the transition line at lower pressures were not carried out to minimize the risk of breaking our sample. The temperature range in which the transition is crossed has become very narrow at this pressure and only very few data points actually lie in this area. This and the fact that the difference between the measurement upon heating and cooling have again increased support the insight that the transition at this pressure is strictly of first order. Especially in the experiment where T was lowered it seems also that the transition takes place in two steps. First at 435 K S decreases by nearly 10%. It increases afterwards by nearly the same amount linearly to nearly 50 $\mu V/K$ when the temperature is lowered to 428 K before the actual decrease to the value of the metallic phase. An explanation for this behaviour could be that in the first step only some parts of the sample pass to the metallic phase and the bulk transition occurs at the lower temperature. At temperatures much higher than the transition temperature both curves fall together again and reach their final value of about 25.5 $\mu V/K$ at 493 K.
In summary, the biggest changes in the different graphs in this relatively narrow region of pressure (the difference between the first and the last graph is merely 250 bar) are the change of the form of the different curves, the appearance of strong hysteresis and the difference in the maximum value of S that increases by nearly 100 %. In the metallic phase below the transition all curves are quite similar although the value of S is decreasing with pressure. Furthermore the different magnitudes of S at 493 K are all similar, which shows that S at this temperature does not change so fast with pressure.
In order to be able to compare the different curves of the temperature dependent measurements around the critical point, in Fig. 6.10 all the available data are presented in one graph.
The most striking feature of this graph is the similarities between the experiments at different pressures but in the same direction of temperature change. Except for 3333 bar, in all curves upon heating at least a small jump in S, whose magnitude increases dramatically with decreasing pressure, can be seen. The values of S upon heating stay nearly constant until a critical temperature is reached and then jump instantaneously to a much higher value. When the temperature continues to rise, S increases continuously until the bulk sample is in the insulating state.
In contrast to this the curves recorded upon cooling seem to be much more continuous, with the exception of the one at the lowest pressure 3097 bar. The shape of all curves is similar and very different from the ones of the heating cycles. Also it proves difficult to assign a clear inset temperature of the transition . At all times the change is much more smooth and ends with a continuous transition to

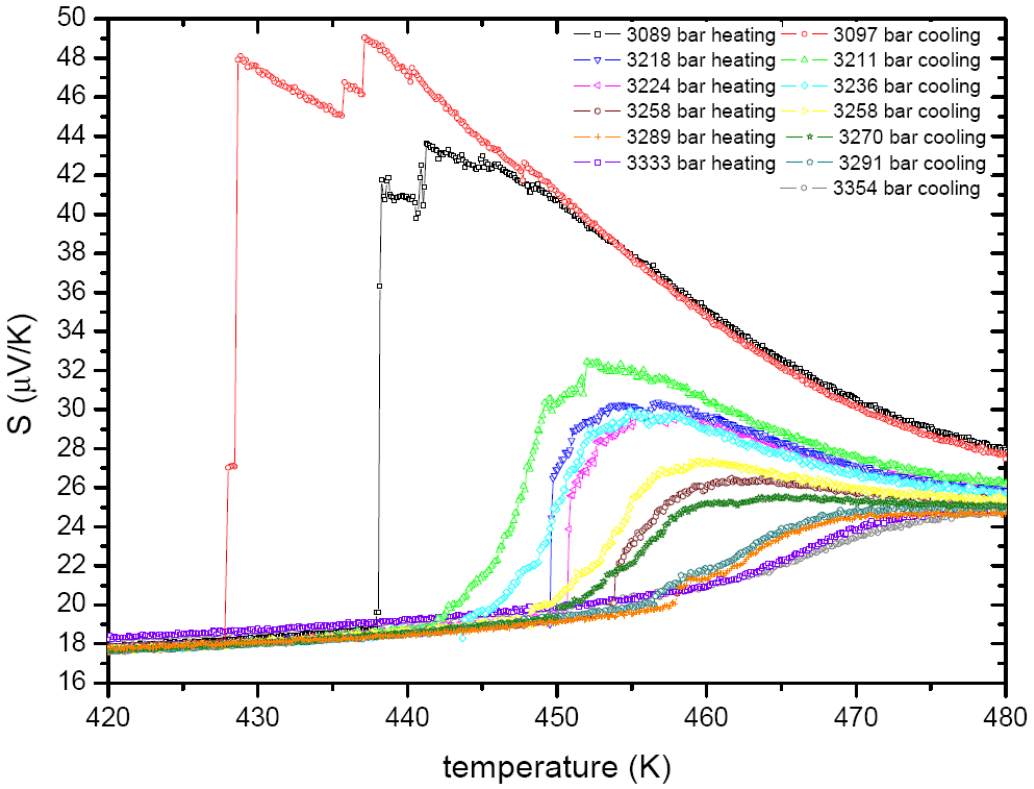

Figure 6.10: The Seebeck coefficient at several pressures between 3089 bar and 3354 bar in the temperature range between 420 K and 480 K. To get information about differences between curves upon heating and cooling it was tried to measure at the same pressure in both directions.

the metallic phase. Also the absolute values are larger than the ones of the heating cycles at similar pressures. This is a result of the hysteresis as upon cooling the transition is crossed at lower temperatures.

The figures at the lowest pressure (around 3090 bar) are very similarly along both directions and the same is true for the two at the highest pressures (around 3340 bar). In order to explain why the curves of the heating cycles in the intermediate region seem much more discontinuous than those upon cooling the following reasons could be used. When changing from a metallic to an insulating state (as upon heating) the Fermi Energy (ϵ_F) is trapped in the quasi particle peak as long as the peak exists. When the quasi particle peak disappears the sample becomes insulating. In the insulating state it is difficult to define where the Fermi energy is exactly and its position is dependent on impurities. This can explain why the thermoelectric power upon heating stays nearly constant as long as the sample is in the metallic region and then evolves continuously in the insulating state. On the

other hand ϵ_F can move freely in the insulating region. Upon cooling down $n(\epsilon)$ varies continuously and self consistently and so does S until the sample is in the metallic phase.

6.4.2 Pressure dependent experiments

In the next step several pressure dependent experiments where the Seebeck coefficient was determined at different temperatures below and above T_c were taken. This was done to gain insights in the pressure dependence of the critical behaviour of S. For this the pressure was changed only very slowly, especially near p_c where the rate did not exceed 5 bar/min.
In Fig. 6.11 our findings for various different temperatures between 493 K and 443 K in the pressure range between 2500 bar and 5000 bar for 493 K and 473 K and from 2700 bar to 3700 bar for temperatures below that are shown. At all temperatures below 493 K the pressure was changed in a complete cycle to examine if any signs of hysteresis could be found.
The first measurement done at 493 K in the pressure range between 2500 bar and 5000 bar can be found in Fig. 6.11(a). From the beginning at $p = 2500\ bar$ and $S = 31\ \mu V/K$ until around 3250 bar and $S = 25\ \mu V/K$ the thermoelectric power is decreasing linearly with increasing pressure. In the following a change of the slope can be identified and from 4000 bar a second region of linear decrease until 5000 bar is visible, where S decreases from $\approx 21\ \mu V/K$ to $\approx 18\ \mu V/K$. As 493 K is clearly above the critical temperature $T_c \approx 458K$ this smooth change in S was expected and shows well the second order of the MIT at this temperature.
The next temperature in Fig. 6.11(b) shows the data collected at 473 K. Both curves are nearly identical and only in the pressure range from 3100 bar to 3400 bar a difference between the two is visible. Amongst heating and cooling there might be the relic of a small hysteresis in the order of magnitude of 10 bar, but the overall form of the curves is similar to those of Fig. 6.11(a). We see two nearly linear intervals and a zone where the slope changes slowly in the middle.
Ten Kelvin lower at 463 K in Fig. 6.11(c) the two linear intervals are becoming more pronounced and the change of the value of S is bigger (at 3200 bar S = 30 $\mu V/K$ and at 3400 bar S = 20 $\mu V/K$), but still continuous.
In the next graph Fig. 6.11(d) at 458 K, just below T_c as estimated in the preceding work by Limelette et al. [5] the continuous character of the transition has changed towards a first order transition, although the difference between the two curves is still very small.
Subsequently in Fig. 6.11(e), showing the results for 453 K, the linear intervals are hardly changed besides the slightly higher values at low pressures, but the area of the transition is shifted to lower pressures and the pressure differences of the

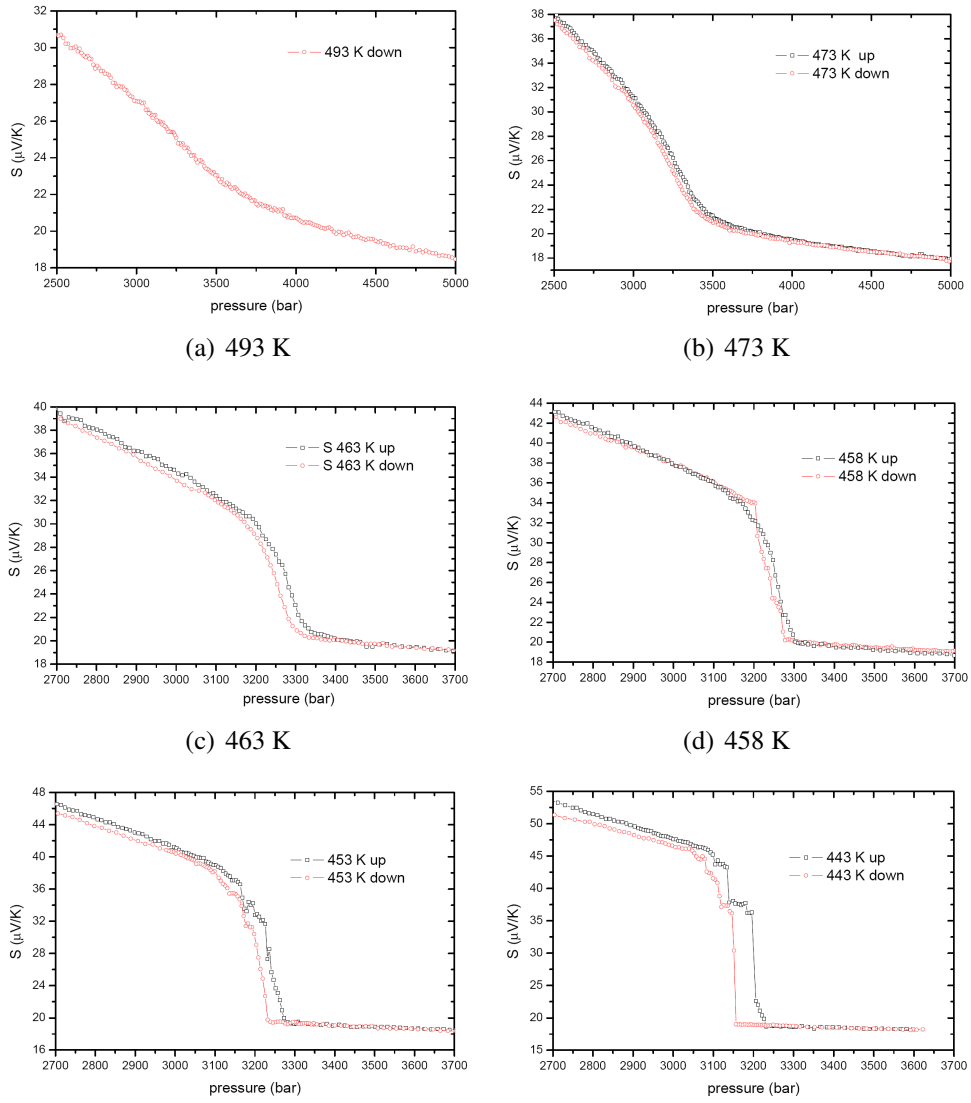

Figure 6.11: Pressure dependent measurements between 2500 bar and 5000 bar at various different temperatures in the range between 473 K and 443 K. To verify if any sign of a hysteresis could be found the measurement was taken out upon heating and cooling.

beginning and the end of the transition between the two experiments are clearly separated in the order of magnitude of 50 bar.

Finally the results for the lowest temperatures 443 K are plotted in Fig. 6.11(f). In this figure the hysteresis is already nearly 100 bars between the two directions of pressure change and due to the rapid crossing of the transition S could be measured only at few points in the transition area.

In total it can be said that the shape of the different curves changes dramatically with temperature and this displays the change in the order of the transition. While for 493 K and 473 K the change of S with pressure is clearly continuous it becomes steadily more and more volatile for the lower temperatures showing that the second order transition becomes of first order. Another evidence is that at the lowest temperatures the two curves obtained by changing the pressure in opposite directions show a large hysteresis. This is in contrast to the nearly superimposed curves for the temperatures above 458 K.

To achieve a better understanding of the differences between the curves at the different temperatures all curves obtained at constant temperature while the pressure was altered are shown in the pressure range between 2500 bar and 4000 bar in Fig. 6.12. The most interesting feature in this figure is that all continuous curves join each other in one point just below 3300 bar and $S \approx 26\ \mu V/K$ and this will allow us to define the critical pressure to 3300 bar.

Finally, in order to give an overview over the acquired data and a better view in the critical region in Fig. 6.13 a 3 dimensional plot of the thermoelectric power in the pressure range between 2500 bar to 4000 bar and from 440 K to 470 K is presented. This figure was created from the information obtained by experiments at fixed temperature with variable pressure. It is easy to see that the thermopower in the metallic phase at the highest pressure increases just slightly with temperature in the shown region while S in the insulating phase at 2500 bar decreases nearly by 50% in the plotted temperature range. At fixed temperature also two different behaviours can be identified for the shown extremes of T. At 468 K S decreases in a continous manner with pressure when going from the insulating to the metallic phase, emphasising the second order nature of the transition at this temperature. At the lowest plotted temperature the jump in S at the transition can be clearly seen. S decreases by more than 5% within only a few bars. Here the transition is as mentioned before of first order. At intermediate temperatures the behavior changes gradually from the one extreme towards the other. We can also follow the evolution of the pressure of the transition. At low temperatures the sample is still in the metallic state at 3250 bar whilst at higher T the behaviour at this pressure is still very similar to the one in the insulating compound.

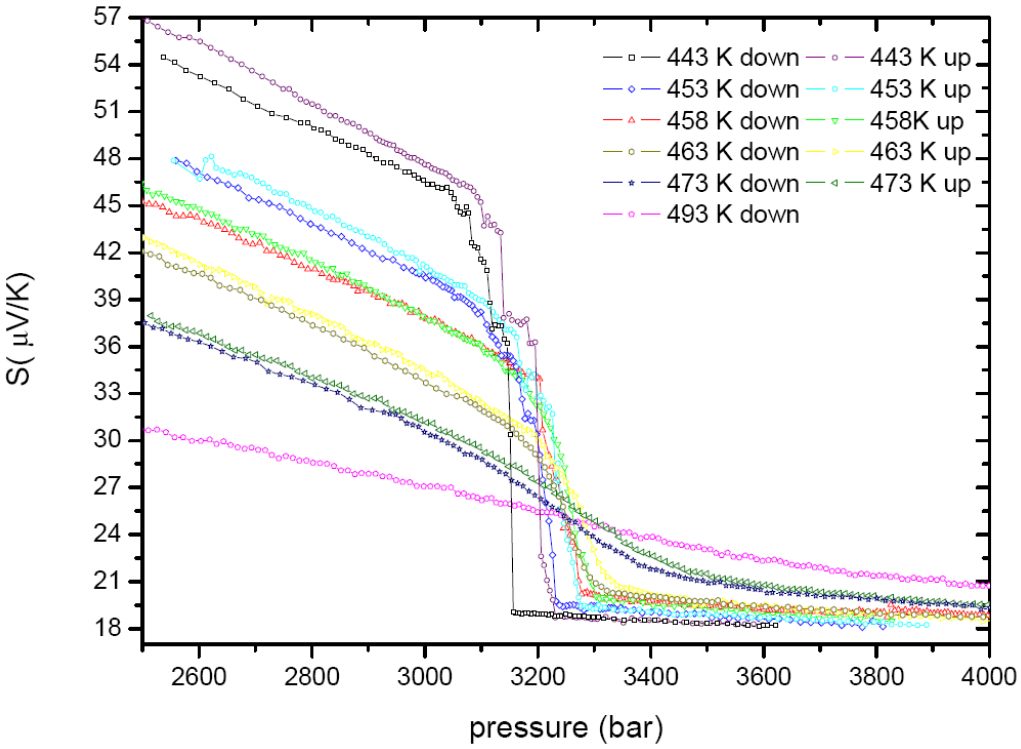

Figure 6.12: The Seebeck coefficient at several temperatures between 443 K and 493 K in the pressure range between 2500 bar and 4000 bar.

6.4.3 Summary

We were able to show that already small differences in the sample preparation can lead to notable differences in the total value of the measured signal. Consequently, we concluded to perform all experiments using the same sample, which has, naturally, always the same positions of the contacts. For this reason extra attention was paid not to break the sample by crossing the first order transition line at too low temperatures.

In the insulating phase the thermopower curves versus temperature are more or less not affected by changes of the pressure. The total value diminishes slightly when approaching higher pressures, but the slope of dS/dT stays nearly constant. Contrary to the metallic phase where the behaviour from the highest pressure, where S stays nearly constant, changes dramatically when the pressure is lowered. This is a consequence of the fact that in this region a crossover line is crossed when temperature is increased.

In the experiments at constant pressure in the intermediate region we were able to observe a large hysteresis, which increased with decreasing pressure. Further, we

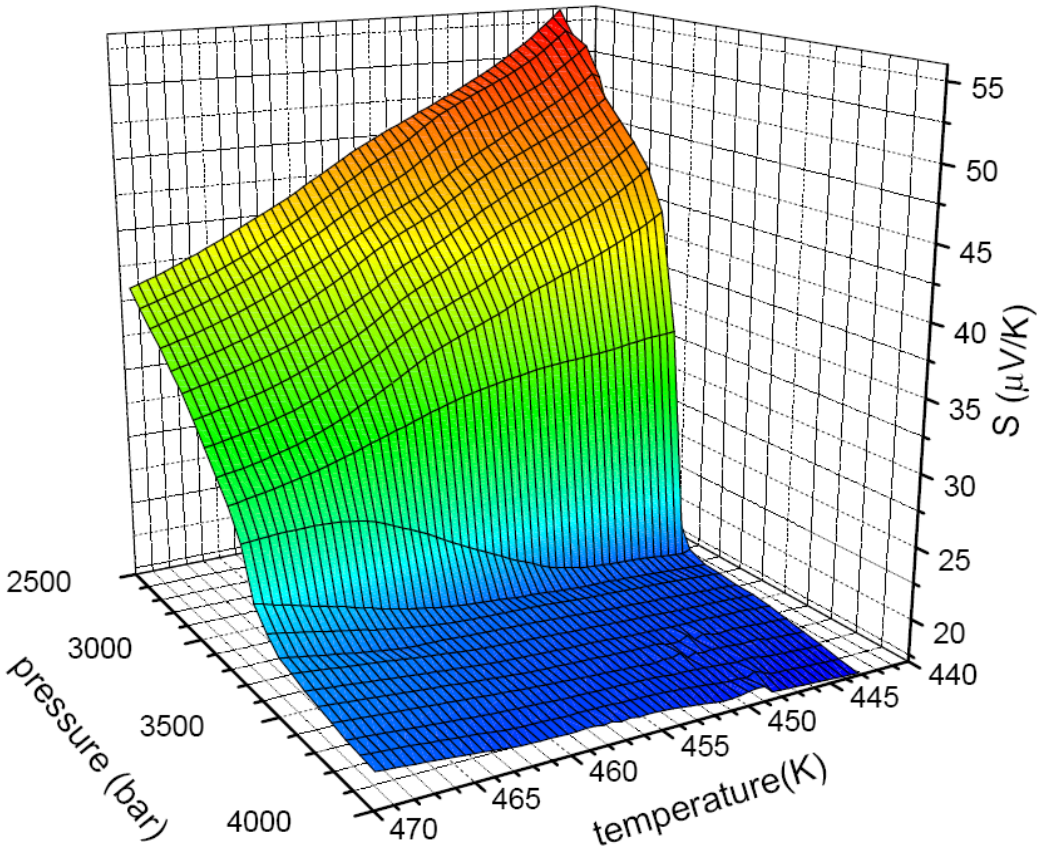

Figure 6.13: 3 dimensional plot of the Seebeck coefficient in the critical region between 440 K and 470 K and 2500 bar and 4000 bar.

could identify different transition temperatures at different fixed pressures and get information about the critical point.

Finally, several experiments where the pressure was changed at fixed temperatures above and below T_c allow us to define transition pressures at fixed temperatures and give additional information about the critical point. The inflection points of the curves above T_c define a second crossover line.

6.5 Analysis of the data

6.5.1 The phase diagram

6.5.1.1 The critical point

In order to estimate the critical temperature and pressure, where the transition becomes continuous, we take a look again at Fig. 6.10. The highest pressure where a small discontinuity is visible is 3289 bar. In addition a small hysteresis of $\approx 2K$ exists between the curves at 3289 bar and 3291 bar. At this point the transition is still of first order and we are slightly below the critical point.
This corresponds to the critical pressure as estimated from Fig. 6.12 to $p_c \approx 3300\ bar$.
The critical point was estimated to $p_c = 3300\ bar \pm 5\ bar$ and $T_c = 460\ K \pm 2\ K$ and can now be compared to the results from chapter 5, where the critical pressure was estimated to 4080 bar and the critical temperature to $T_c = 458\ K \pm 5\ K$ and the critical pressure to $p_c = 4080\ bar \pm 40\ bar$. The critical pressure is different in the two cases and we conclude that although the samples for the two different experiments originate from the same batch, the doping is quite likely not identical. A small difference in the doping of 0.1% would already result in a pressure shift of approximately 500 bar. The critical temperature is idetical within the experimental errors for both experiments.
The values for the critical point can be compared to the values of Limelette et al. [5], who used samples doped with nominally the same amount of chromium as ours. The values of Limelette are $p_c = 3738\ bar$ and $T_c = 457.5\ K$, given without any errors. p_c lies in between our two values and shows the liability of the critical pressure to small differences in the amount of doping. Our critical temperature lies a bit higher, but is not too far from the value of Limelette.

6.5.1.2 The crossover

Adjacent to the critical point, the first order transition lines are continued by a crossover line which is defined by the maximum of the derivative of S with respect to the temperature at fixed pressures of Fig. 6.8. The values for the crossover estimated like this can be found in Tab. 6.1.

pressure (bar)	3332	3352	3420	3527	3630
$T_{crossover}$ (K)	466	468	470	475	485

Table 6.1: Crossover line above the critical point defined by the maximum of the derivative of S with respect to the temperature.

A second crossover line can be determined by calculation of the inflection points of the pressure dependent measurements at fixed temperatures above T_c, which are shown in Fig. 6.12. The values of the second crossover can be found in Tab. 6.2.

pressure (bar)	3277	3297	3299
$T_{crossover^*}$ (K)	463	473	493

Table 6.2: Crossover line above the critical point defined by the inflection points of the pressure dependent experiments above T_C.

The two lines connecting these points and the critical point, define two crossover lines at high temperatures, which separate a purely insulating region at low temperatures and low pressures, a purely metallic region at low temperatures and high pressures and an intermediate crossover sector at high temperatures and intermediate pressures, which is expected by the theory of a critical point (see for example [106]).

6.5.1.3 The experimental phase diagram

In order to be able to follow the evolution of the phase transition with pressure and temperature an experimentally established phase diagram can be found in Fig. 6.14. The points for the crossover were taken from Tab. 6.1 and Tab. 6.2 and were estimated as described above. The points from the two transition lines were estimated from 6.10 and identified with the departure from the flat metallic behaviour.
This phase diagram can now be compared to the one in Fig. 3.4 Limelette et al. [5]. Qualitatively the two agree quite well, although our experimental window is smaller. The temperature of the critical point of [5] is within our error range. Differences in the pressure range can be explained with uncertainties of the exact amount of doping. 0.1 % difference in Cr already results in a difference of $\approx 400\ bar$. We were also able to establish two crossover lines for the limits of the insulating and the metallic behaviour.

6.5.2 Properties of the Mott insulating state

To be able to describe the behaviour of the Seebeck coefficient in the insulating state, the Mott insulator can be described as a semiconductor. According to Eq. 6.9 the thermoelectric power for a semiconductor contains two components:

$$S = \frac{k_B}{e}\frac{\Delta}{k_B T} + A, \tag{6.18}$$

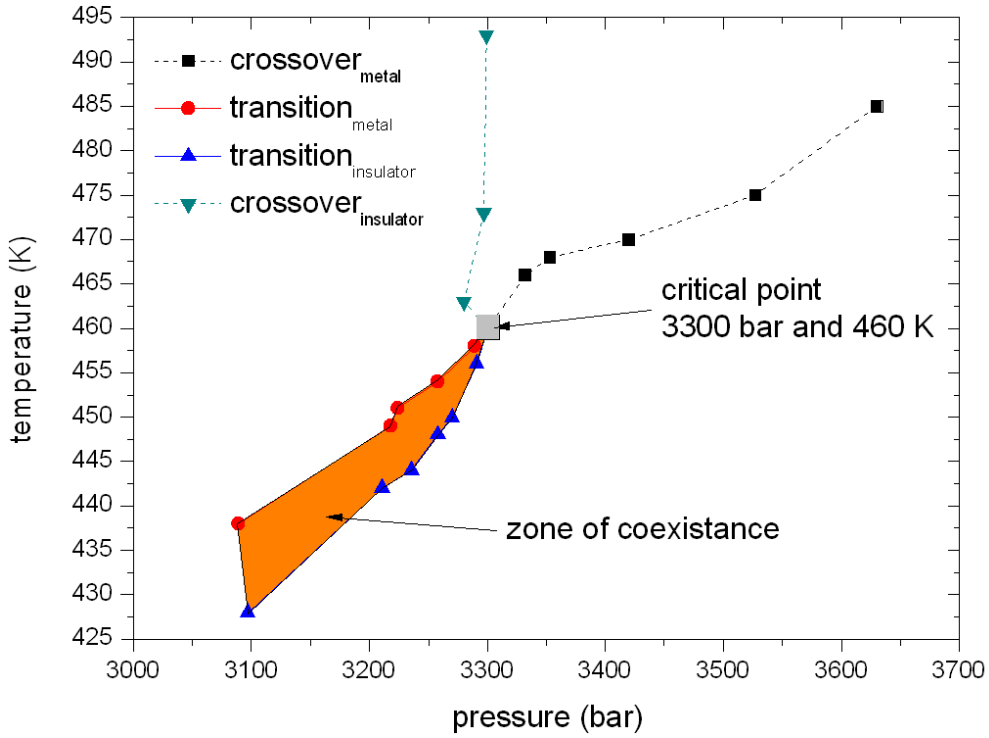

Figure 6.14: Experimental phase diagram deduced from the results of the thermopower experiments.

where the temperature independent part A depends on the nature of the electron scattering process and $\Delta = E_c - E_F$ corresponds to the activation energy from the Fermi energy to the conduction band.
In analogy to this equation it should, in principle, be possible to estimate the activation energy from a plot of S vs the reciprocal temperature, where Δ (in K) can be calculated with the help of the slope B of an ordinary linear fit $y = A + Bx$ by using this relation:

$$\Delta = \frac{e}{k_B} B. \tag{6.19}$$

In order to verify this, in 6.15 the Seebeck coefficient in the insulating region is plotted against the inverse temperature. It is easy to see that S is increasing linearly only in a limited area in the middle of the temperature range. This is not surprising as for a Mott-Hubbard insulator the band gap is normally a function of temperature and is filled with increasing temperature by transferred incoherent spectral weight [107].
Nonetheless we tried to estimate the largest possible temperature range showing a linear behaviour for the different pressure and calculated the fit parameter B

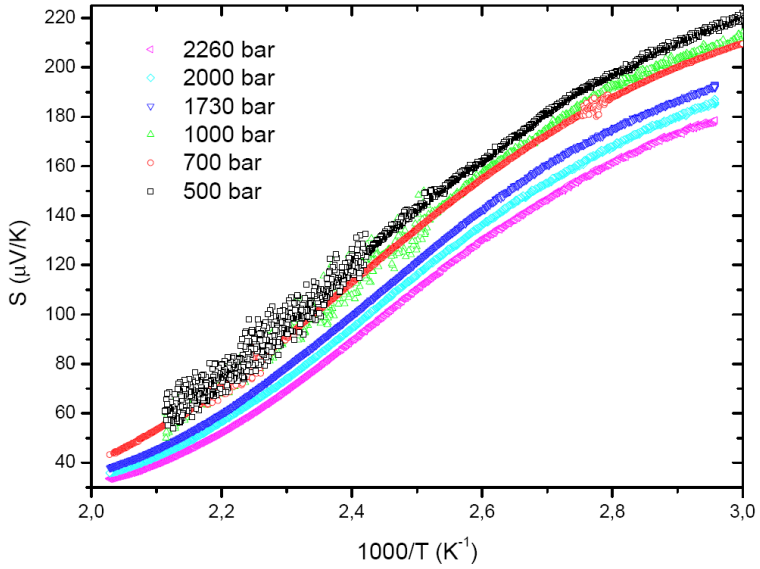

Figure 6.15: The Seebeck coefficient in the insulating state at various pressures between 500 bar and 2260 bar plotted against the inverse temperature between 500 K and 333 K.

and the resulting activation energies in meV and K. Due to the relatively small linear region the uncertainties in these values are big and no difference between the different pressures exceeds these uncertainties. The results are presented in Tab. 6.3. These qualitative results are now compared to the ones existing in the

B (10^{-3})	Δ (meV)	Δ (K)
200	200	2300

Table 6.3: Activation energy in the insulating state.

literature to get an idea if we are at least in the right order of magnitude with our finding.

Limelette et al. determined $E_g = 2 \times \Delta = 1480\ K$ by transport measurements [4] and another value is $\Delta = 120\ meV$ as the results of photo emission experiments [108]. Our value is larger by a factor of 3 or respectively 2, but in the right order of magnitude.

6.5.3 Properties of the metallic phase

Using the free electron model allows to write the total thermopower S for metallic compounds at high temperatures:

$$S = BT + AT^{-1} + C(T), \tag{6.20}$$

where BT represents the theoretical diffusion term in the relaxation time approximation, which for high temperatures and $T \ll T_F$ for free electrons is defined as (cp. Eq 6.8):

$$S^d = BT = \frac{\pi^2}{6}\frac{k_B}{e}\frac{T}{T_F}, \tag{6.21}$$

which is the term defined from the band structure. The second term AT^{-1} represents the phonon drag. The term depending on the relaxation time is neglected as we assume in a rough approximation that the relaxation time is constant in our T, p-range in the metallic state near the critical point.
Now both sides of the equation are multiplied with T and we get:

$$ST = BT^2 + A. \tag{6.22}$$

Subsequently, a plot of ST vs T^2 should result in a straight line whose intercept is A and whose slope is B. In order to have as less influence as possible from the crossover regime, the data of the experiment at the highest pressure, namely 5740 bar, is plotted in Fig. 6.16. Over the whole temperature range the resulting fit is in very good agreement with the data and only at the above described low temperature a small departure from the linear behaviour of ST vs T^2 can be observed. This linear behaviour confirms the validity of the approximation to neglect the relaxation term.
Next this procedure was executed at various different pressures and the obtained results together with the ones from the fit at 5740 bar can be found in Tab. 6.4. The variable A of the phonon part of the thermoelectric power stays constant over the whole range of different pressures at a value of about 2.9 mV, while B coming from the diffusion term slightly decreases approaching the transition and the resulting Fermi energy decreases from 2.99 eV at 5740 bar to 2.72 eV at 3290 bar.
Now with A determined the formula Equ. 6.22 can be inverted to:

$$\frac{ST - A}{T^2} = B(T),$$

which leads to the following temperature dependent expression for the Fermi temperature:

$$T_F = \pi^2\frac{k_b}{e}\frac{1}{B(T)} = \pi^2\frac{k_b}{e}\frac{T^2}{ST - A}. \tag{6.23}$$

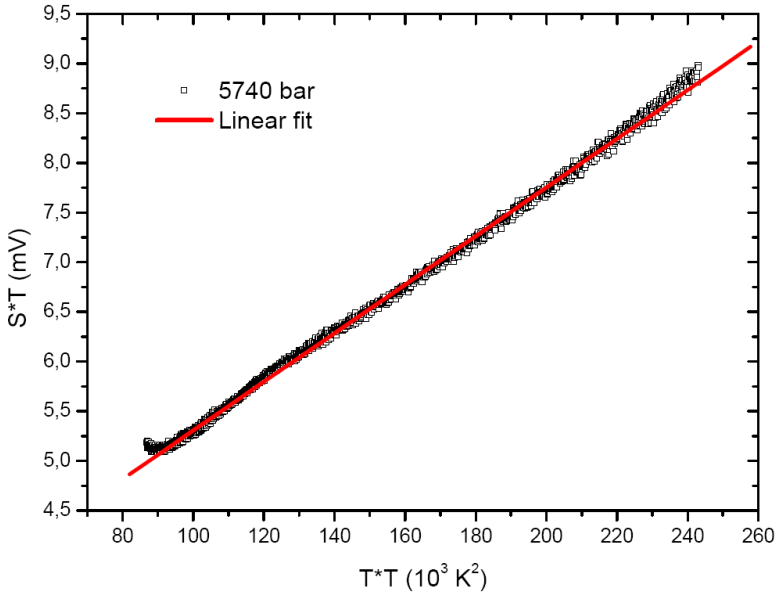

Figure 6.16: ST plotted versus T^2 in the metallic region at 5740 bar in the temperature range between 300 K and 490 K.

p (bar)	T^2 $(10^3 K^{-1})$	A (mV)	B $(10^{-3}\mu V K^{-2})$	T_F (K)	E_F (eV)
5740	92 - 243	2.86	2.45	5780	0.50
4800	93 - 220	2.93	2.56	5530	0.48
4050	92 - 200	2.81	2.61	5430	0.47
3800	91 - 190	2.92	2.58	5500	0.47
3600	91 - 187	2.92	2.61	5430	0.47
3500	91 - 185	2.91	2.63	5380	0.47
3400	91 - 183	2.92	2.65	5350	0.46
3290	92 - 190	2.64	2.68	5270	0.45

Table 6.4: This table shows the regions in the metallic phase where ST vs T^2 could be fitted with a linear fit, the obtained fit parameters A and B, and finally the resulting Fermi temperature and the Fermi energy. It has to be noted that at lower pressures where only a smaller part could be fitted the uncertainties in the obtained values become much larger.

With the help of this formula it is now possible to calculate T_F as a function of temperature at various fixed pressures. The results of this calculation can be found in Fig. 6.17 where the Fermi energy is plotted for the metallic phase between 380 K and 480 K and 3300 bar and 4100 bar. All these observations demonstrate a fall-down of T_F on the approach of the critical point as expected due to the

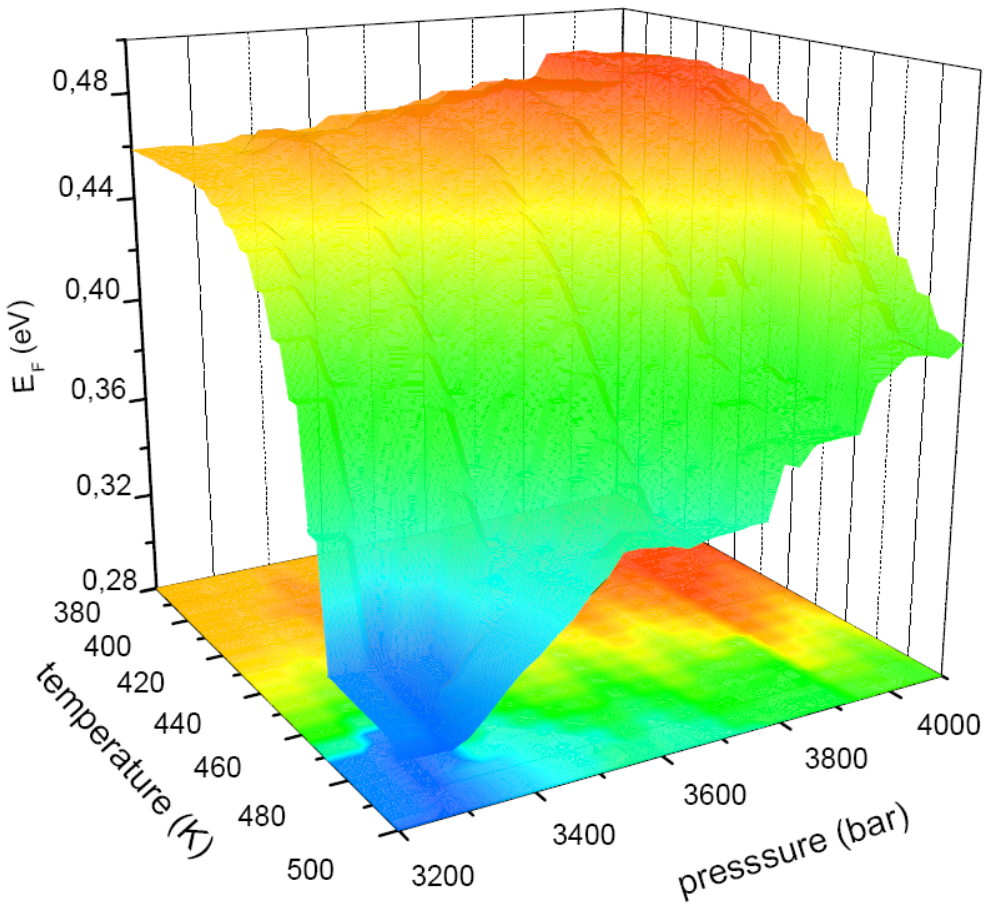

Figure 6.17: The Fermi energy calculated as described in the text as a function of temperature and pressure in the free electron approximation.

disappearance of the quasi-particle peak.

The fitting procedure appears to remain surprisingly correct as the condition $T \ll T_F$ remains fulfilled in the full (p,T)-range. Moreover the value of T_F seems to be in the right order of magnitude and the behaviour is qualitatively correct. Taking into account the rough approximations taken in this paragraph we can conclude that the Fermi energy seems to collapse at the critical point and a more suitable model is needed to analyze the data around this point. The total value of the absolute Fermi energy far from the transition is in the order of $E_F \approx 0.5\ eV$. This value can be compared to results from band structure calculations, where E_F is given as the half bandwidth of the conduction band. Due to the complicated band structure of V_20_3 with multiple bands crossing the Fermi level only a rough estimation of the value of E_F can be given. Band structure calculations by Mattheiss

[63] (by LDA) and Held et al. [109] (by LDA+DMFT) yield an $E_F \approx 1.0eV$, which is only about a factor of 2 larger than our estimated value. Due to our rough approximations this can be regarded as a very good agreement.

6.5.4 The transport coefficients

Following Eq. 6.5 the thermopower S is proportional to the ratio of the transport coefficients K_1 and K_0 multiplied by T^{-1}. Eq. 6.6 yields that the electric conductivity σ is proportional to K_0 and from $\sigma = \rho^{-1}$ it follows:

$$\rho \propto K_0^{-1}.$$

From resistivity data in the literature and our thermopower results it is now possible to estimate the behaviour of the transport coefficient K_1.

$$K_1 \propto \frac{ST}{R} \tag{6.24}$$

This coefficient is according to its definition in Eq. 6.7:

$$K_1 = -\frac{1}{3}\int 2\tau_k v_k v_k \left(-\frac{\partial f_0}{\partial \epsilon}\right)|_{\epsilon=\mu}\left(\epsilon(k)-\mu\right) d^3k,$$

sensitive to the asymmetry between electrons and holes and vanishes when perfect symmetry is existing. Therefore a single-site Hubbard model (such as used for DMFT) is insufficient. An estimation of K_1 allows to get information about the shape of the quasi-particle peak, which is responsible for the conduction.
Using this relation K_1 was qualitatively calculated for two different pressures in dependence of the temperature and at two different temperatures in dependence of the pressure.
The resistivity data was taken from Limelette [4, 5] and can be found in Fig. 6.18. It is important to note that as the critical pressure of Limelette et al. and ours are not the same, for the resistivity data $\approx 450\ bar$ higher pressures were used. The first displayed curve is at a pressure just above the critical point 3333 bar and the second one further in the metallic region at 4050 bar, where the transition line is not crossed.
With the help of this data is was possible to calculate K_1 and the results are displayed in Fig. 6.19(a) the variation of K_1 against temperature.
From room temperature up to 390 K both curves stay nearly constant and at similar values. The curve at 4050 bar decreases continuously towards its minimum at 490 K, where it is at nearly half of the value of 350 K. The curve of 3333 bar decreases steeper and reaches a minimum little above 450 K, which probably corresponds

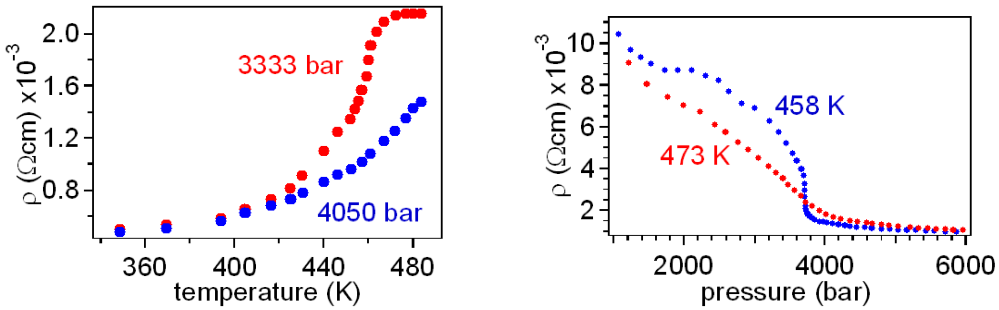

(a) ρ vs. T at 4050 bar and 3333 bar

(b) ρ vs. T at 458 K and 473 K

Figure 6.18: Resistivity data taken from the literature [4, 5].

to the transition temperature. The increase at the highest temperatures is probably an artefact of the calculation.

This behaviour can be qualitatively explained. In the metallic phase the quasi-particle peak is well defined and stays unchanged until 390 K. Under the influence of the transition when approaching the insulating or the crossover region, this peak starts to broaden and the asymmetries are more and more averaged out.

In Fig. 6.19(b) K_1 is displayed vs pressure at two different temperatures. In the curve at 473 K a continuous increase of K_1 with temperature can be observed. This reflects that the quasi-particle peak becomes more and more well defined and asymmetries are less and less averaged out, which leads to an increase of K_1 and doubles its value from 2500 bar to 5000 bar.

The curve at 458 K near T_c shows already a discontinuous change of first order of K_1, where the shape of the quasi-particle peak changes abruptly at p_c and the quasi-particle becomes suddenly more thin and well defined, the life time of the quasi-particles increases. The value of K_1 in the metallic phase is approximately the double of the value in the insulating phase.

In conclusion it can be said that for both sub figures in Fig. 6.19 the total change in K_1 is small compared to the change of the conductivity, which changes about three to five times more in the critical region. Thus we conclude that the evolution of the particle-hole symmetry does not play a crucial role in the transition.

6.5.5 Scaling of the critical behaviour

The basic ideas of the scaling of the metal-insulator transition have already been reviewed in the previous chapter. Due to the lack of a theory for the critical behaviour of the thermopower we remind ourselves of Eq. 6.24 that brings the ther-

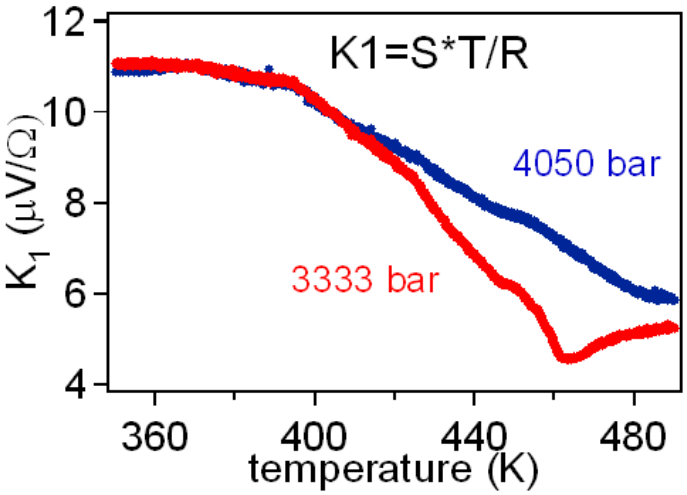

(a) K_1 vs. T at 4050 bar and 3333 bar

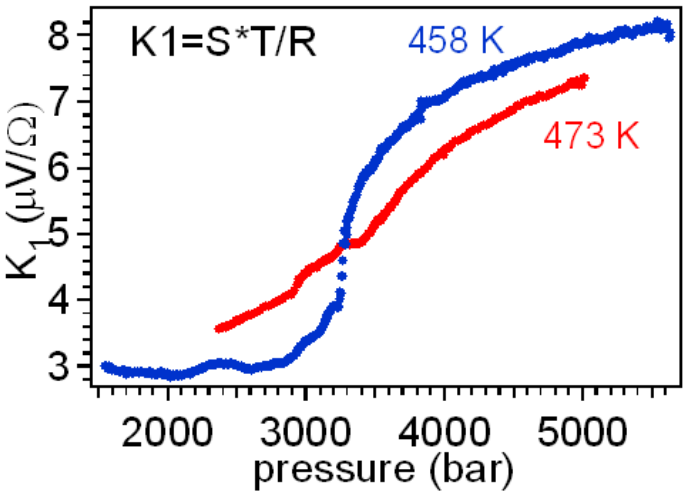

(b) K_1 vs. T at 458 K and 473 K

Figure 6.19: The transport coefficient K_1 calculated from our thermopower data and resistivity data in the literature [4, 5].

mopower in relation to the resistivity and the conductivity and can be written as:

$$\frac{1}{S} \propto \frac{\sigma T}{K_1}. \tag{6.25}$$

If we now take in a rough approximation K_1, as shown in Fig. 6.19, as constant in the vicinity of the transition compared to the huge change of the conductivity and also approximate that T is constant very near to the transition we can conclude that the critical behaviour of the inverse thermopower should be governed by the critical behaviour of the electrical conductivity:

$$\frac{1}{S} \propto \sigma. \tag{6.26}$$

This assumption allows us to compare the critical behaviour of the Seebeck coefficients to the scaling laws employed by Limelette et al. [5] for the electrical conductivity.
Limelette et al. were able to show that the derivative of the conductivity with respect to pressure, by taking the derivative at the inflection point of $\sigma(P)$, is in analogy to the magnetic susceptibility as a function of the reduced temperature $t = |\frac{T_c - T}{T_c}|$:

$$\left(\frac{dm}{dp}\right)_{p=p_c}(T) \propto \frac{1}{t^\gamma}. \tag{6.27}$$

The critical exponent γ was estimated to $\gamma = 1$ as attended from the mean field theory.
This susceptibility characterises the fluctuations associated with the order parameter and by this it is valid at temperatures below and above T_c. Due to the low data density during the transition at temperatures below T_c it is only possible for us to calculate the inflection point at temperatures $T > T_c$. The calculated slopes at the inflection points are plotted in Fig. 6.20 and compared to a function with the attended mean field value $\gamma = 1$ from electrical conductivity. Despite the fact that only four data points are at hand, the function with the exponent $\gamma = 1$ is satisfactorily consistent with our data.
The temperature dependence of the order parameter was in analogy to the liquid-gas transition identified with:

$$\sigma - \sigma_c = t^\beta, \tag{6.28}$$

where σ is the conductivity in the metallic phase below the transition and σ_c is the critical value of the conductivity. This yielded the mean field exponent $\beta = 0.5$
In order to compare this to the critical behaviour of S, in Fig. 6.21(a) a measurement at 3291 bar while the temperature was swept is displayed, where $\frac{1}{S^\star} = \frac{1}{S} - \frac{1}{S_c}$

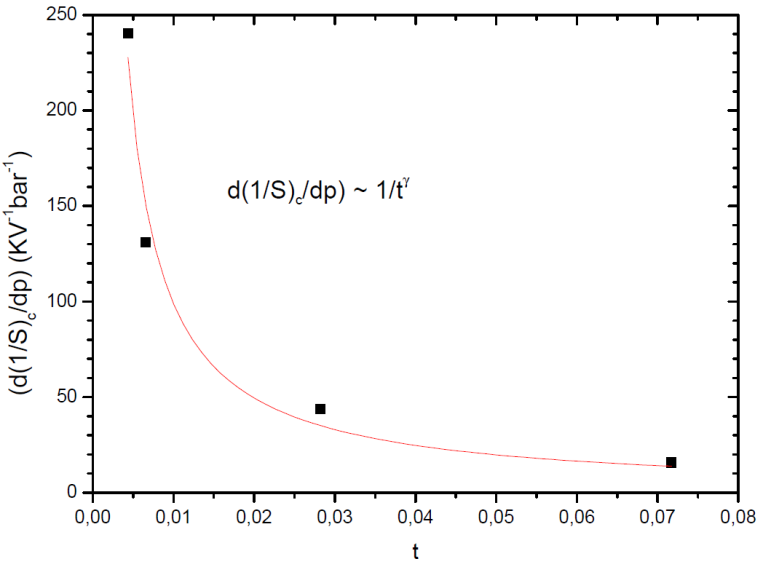

Figure 6.20: Fit of the critical behaviour with the temperature just above p_c.

is plotted against t. For comparison the power law with the mean field value $t^{0.5}$ is also plotted. This function reproduces our data for $t < 0.05$ quite well.
Finally, at the critical temperature $T = T_c$ Limelette et al. [4, 5] could show that

$$\sigma - \sigma_c = h^{1/\delta}, \tag{6.29}$$

where h corresponds to the reduced pressure $h = |\frac{p_c - p}{p_c}|$. Their analysis yielded the mean field value $\delta = 3$.
In Fig. 6.21(b) the pressure dependence of $\frac{1}{S} - \frac{1}{S_c} \propto \sigma - \sigma_c$ is plotted as a function of pressure together with $h^{1/3}$, which is for $t < 0.05$ in good agreement with our data.
The good agreement of the critical exponents found in conductivity experiments [4, 5] with our data near to the critical point implies that our assumptions of K_1 and T being nearly constant compared to the large change of the electrical conductivity in a small range of temperature and pressure is justified. The critical behaviour of S near the critical point is governed by the critical behaviour of σ. Nonetheless, these assumptions become false far from the transition, where the scaling functions from the conductivity do not reproduce our data anymore.

6.6 Conclusion

In a first experiment we tried to extract the thermal conductivity from the data acquired for the calculation of the Seebeck coefficient. A jump in the thermal

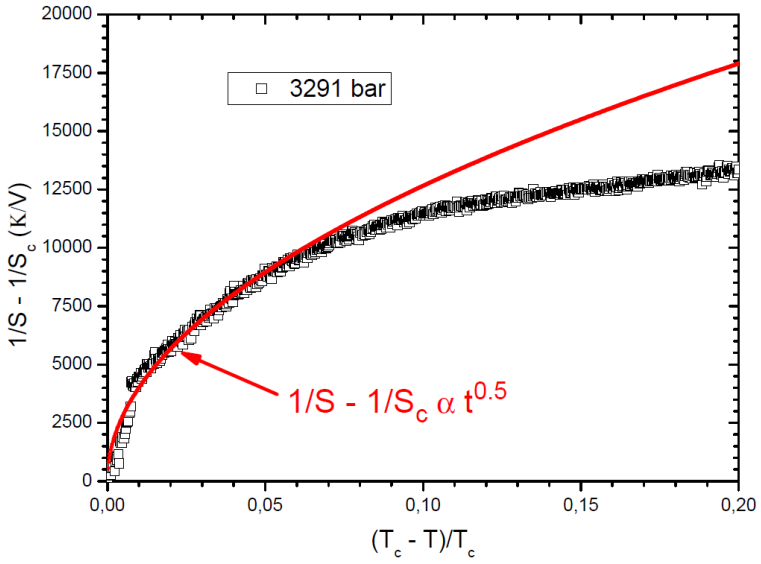

(a) Fit of the critical behaviour with temperature at 3291 bar.

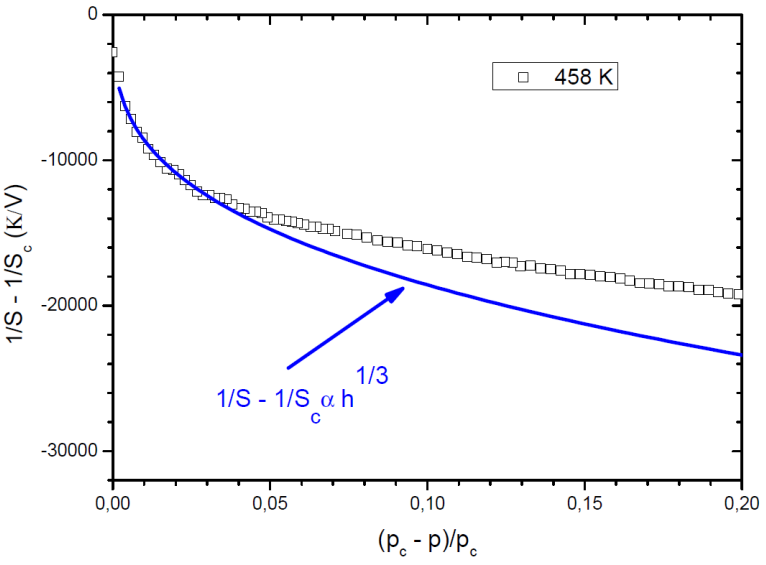

(b) Fit of the critical behaviour with pressure at 458K.

Figure 6.21: Power laws for the critical behaviour of the reduced temperature t and the reduced pressure h.

conductivity could be observed at the transition, but the resulting values did not correspond to the ones in the literature. We concluded that due to the thermal coupling of the pressure liquid to the heater, the effective heat energy going into the sample is unknown and hence a quantitative analysis was impossible. A calibration measurement on a sample with known thermal conductivity could give information about the amount of heat energy delivered to the sample.
The thermoelectric power was successfully measured as a function of temperature and pressure in the temperature range between room temperature and 493 K at various hydrostatic pressures between 500 bar and 6000 bar. Our results are in qualitative and roughly quantitative agreement with the few existing reference values in the literature [101, 100, 99] and we were able to observe clearly the MIT in our data.
Two experiments upon cooling from room temperature to approximately 230 K in a low vacuum of 10^{-2} bar showed the dependence of the measured absolute value on the experimental set-up. The results were in qualitative agreement with the literature [99]. In order to be able to compare the results of the different experiments all subsequent experiments were conducted with the same sample and thus the same set-up.
We were able to investigate the evolution of the Seebeck coefficient with temperature and pressure in the insulating phase, in the metallic phase and in the region of the transition. An experimental phase diagram (Fig. 6.14) could be established, showing a large hysteresis depending in which direction the transition was crossed below the critical point, T_c, and p_c could be determined from the experimental data. Finally, two crossover lines, as expected from the theory, were found above the critical point.
From a qualitative analysis of the temperature behaviour in the insulating phase, the band gap Δ could be determined with a value in the order of magnitude expected from the literature. The Fermi energy, calculated from the data in the metallic phase, is also of the correct order of magnitude and shows the expected strong decrease upon approaching the transition.
By the comparison with data from resistivity experiments we were able to extract information about the behaviour of the quasi-particle peak across the transition. The results were in qualitative agreement with the ones attended from theory.
Finally, several power laws for the critical behaviour of S near the critical point could be observed experimentally. As no theory for the critical behaviour of the Seebeck coefficient is at hand, we used the previously obtained information about K_1 to relate the inverse Seebeck coefficient to the critical exponents from electrical conductivity measurements. In the vicinity of the transition our data could be quite well reproduced and this confirmed our assumptions that the critical behaviour of S was governed by the critical behaviour of σ.

Chapter 7

Conclusion

7.1 Summary

The main goal of this work to investigate the high temperature metal-insulator transition from the paramagnetic metallic to the paramagnetic insulating phase of $(V_{0.989}\ Cr_{0.011})_2O_3$ near the critical point by means of two different experimental techniques was fulfilled.

The experimental set-up for ultrasound measurements was successfully installed, tested and used to investigate the MIT of V_2O_3. Our unique experimental equipment allowed us to investigate the transition at high temperature while the pressure was continuously changed. Due to experimental difficulties with micro cracks in the sample, which appeared upon crossing the transition, mostly only a qualitative analysis of our findings was possible. The points where data were on-hand in the literature could be verified by our results. Observation of the behaviour of the transversal mode of the speed of sound allowed to conclude that the high temperature Mott transition occurs without symmetry breaking and the order parameter is a scalar. Further, the theoretical prediction achieved by means of DMFT for the critical behaviour of the speed of sound in V_2O_3 by Hassan et al. [3] could be qualitatively verified. We were able to present the first systematic study of the influence of the band structure on the high temperature Mott transition in V_2O_3 and could verify the existence of a critical electronic temperature T_c^{el} that differs in the order of 3% or 4% from the temperature of the transition T_c of the bulk sample.

In the second part of this thesis the evolution of the Seebeck coefficient was investigated under the same experimental conditions. The very limited data in the literature were roughly in agreement with our findings. We were able to get detailed information about the behaviour of S in the insulating state and could roughly estimate the energy of the band gap as well as the behaviour in the metallic phase

where we could estimate the Fermi energy at least to the right order of magnitude and observe the attended breakdown of E_F at the phase transition where the quasi-particle peak disappears. The studies around the critical point allowed us to establish an experimental phase diagram including two theoretically predicted crossover lines [106]. Our phase diagram is in qualitative agreement with the one existing in the literature from resistivity data. Furthermore, we were able to show with the help of resistivity data in the literature that the change of the Seebeck coefficient at the Mott transition is rather driven by the change in the resistivity than by the change of the particle-hole symmetry. As a consequence of this we could, in analogy to the liquid-gas transition, relate the scaling laws for the critical parameters near to the transition found for the scaling of the conductivity to our data. In the vicinity of the transition our data were quite well reproduced by the mean field exponents found in the conductivity experiments.
By comparing the results of both experimental techniques it becomes clear that thermopower is much less sensitive to destruction of the samples at the transition. For the speed of sound it was even not possible to cross the transition well above T_c without a significant decrease in the signal intensity, which is caused by micro cracks in the sample or the separation of the transducer from the sample. In contrast, in the thermopower experiment it was possible to cross the transition even significantly below T_c without damage to the sample. As a result all data presented for the measurement using the pressure cell could be performed using the same sample, which eliminated uncertainties due to the sample preparation and it was possible to obtain a more complete overview of the transition with this technique. The estimated critical temperature T_c was identical for both experiments within the experimental errors. For the critical pressure we found a shift of p_c between the two experiments of around 700 bar. This could be explained with a different amount of chromium within the two specimens.

7.2 Further work

For a more quantitative analysis of the data for the speed of sound another temperature dependent measurement in the critical region is needed in order to be able to normalise our data correctly at the critical pressure. Due to experimental difficulties it was until now not possible to carry out this experiment successfully, but from the temperature dependent behaviour at the critical pressure γ could be estimated and be used for a more realistic simulation of the speed of sound.
We were able to show that in principle it is possible to calculate the thermal conductivity from the data acquired in order to estimate the thermoelectric power. In order to be able to use this inside the pressure cell with the pressure liquid the amount of energy dissipated at the heater that really heats the sample must be de-

termined. One approach to do this could be a calibration measurement, but this implies that the sample has to be always installed in the same way, which might prove quite difficult. Other solutions are not yet on-hand, but for measurements inside a cryostat, where the sample is thermally isolated, it should not cause any problems to measure the thermal conductivity simultaneously.
The coefficients that govern the thermal and electrical responses are reduced in the framework of DMFT to averages over the spectral density $\rho(\epsilon, \omega)$ [110] and can be given as:

$$S = \frac{-k_B}{e} \frac{A_1}{A_0}, \tag{7.1}$$

where the coefficients A_n are defined in the following manner:

$$A_n = \frac{N\pi}{\hbar k_B} \int_{-\infty}^{\infty} d\omega d\epsilon \frac{\rho^2(\epsilon, \omega)(\omega\beta)^n}{4\cosh^2\left(\frac{\beta\omega}{2}\right)} \phi(\epsilon).$$

For a particle-hole symmetric model the coefficient A_1 is zero and therefore S vanishes. Hence it is not possible to use the single site DMFT approach that had been, for example, employed by Hassan et al. [3] to calculate the sound speed using a single band, half-filled Hubbard model for V_2O_3.
With the help of LDA+DMFT it is possible to achieve more realistic simulations of the band structure, which have already been used to calculate the thermoelectric power by Palsson et al. [96] and Oudovenko et al. [111]. The obtained results are in agreement with the experimental data of real compounds such as $La_{1-x}Sr_xTiO_3$ [112].
In order to be able to compare our findings with theoretical calculations a more realistic model for the band structure of V_2O_3 that takes into account things such as orbital degeneracy and two d electrons has to be developed. At the moment this is under way by the theoretical group of our laboratory.

Appendix A

Tables of interatomic distances and bond angles

Atoms	Distances (Å) and bond angles (°)	
	V_2O_3	$(V_{0.99}\,Cr_{0.01})_2O_3$
M(1) - M(2)	2.697 (1)	2.700 (1)
M(1) - M(3)	2.880 (1)	2.884 (1)
M(1) - O(1)	2.051 (1)	2.050 (1)
M(1) - O(5)	1.968 (1)	1.970 (1)
O(1) - O(2)	2.676 (3)	2.673 (3)
O(1) - O(4)	2.804 (1)	2.802 (1)
O(1) - O(5)	2.889 (1)	2.890 (1)
O(4) - O(5)	2.952 (1)	2.958 (2)
O(1) - M(1) - O(2)	81.45 (7)	81.36 (5)
O(1) - M(1) - O(4)	88.46 (2)	88.36 (2)
O(1) - M(1) - O(5)	91.90 (5)	91.91 (4)
O(1) - M(1) - O(6)	168.62 (8)	168.43 (6)
O(4) - M(1) - O(5)	97.17 (3)	97.32 (2)
M(1) - O(1) - M(2)	82.23 (9)	82.36 (6)
M(1) - O(2) - M(3)	91.54 (3)	91.64 (2)
M(2) - O(2) - M(3)	133.21 (5)	133.23 (3)

Table A.1: Comparison of the interatomic distances and bond angles between the different atoms in pure [65, 62] and Cr-doped V_2O_3 in the PM phase [66] at room temperature (standard deviations in brackets).

Atoms	Distances (Å) and bond angles (°)		
	V_2O_3 at 600 °C	$(V_{0.99}\,Cr_{0.01})_2O_3$	$(V_{0.962}\,Cr_{0.038})_2O_3$
M(1) - M(2)	2.738 (1)	2.747 (1)	2.746 (1)
M(1) - M(3)	2.924 (1)	2.917 (1)	2.918 (1)
M(1) - O(1)	2.066 (1)	2.061 (1)	2.062 (1)
M(1) - O(5)	1.981 (1)	1.976 (1)	1.975 (1)
O(1) - O(2)	2.681 (3)	2.661 (2)	2.664 (2)
O(4) - O(5)	3.007 (1)	3.004 (1)	3.004 (1)
O(1) - O(4)	2.800 (1)	2.792 (1)	2.791 (1)
O(1) - O(5)	2.901 (1)	2.897 (1)	2.895 (1)
O(1) - M(1) - O(2)	80.89 (7)	80.42 (4)	80.49 (3)
O(4) - M(1) - O(5)	98.56 (3)	98.93 (2)	98.98 (2)
O(1) - M(1) - O(4)	87.52 (2)	87.51 (1)	87.46 (1)
O(1) - M(1) - O(5)	91.52 (2)	91.71 (3)	91.63 (2)
O(1) - M(1) - O(6)	167.00 (7)	166.50 (5)	166.51 (4)
M(1) - O(1) - M(2)	82.98 (9)	83.60 (5)	83.52 (4)
M(1) - O(2) - M(3)	92.48 (2)	92.49 (1)	92.54 (1)
M(1) - O(5) - M(4)	—	121.70 (7)	121.74 (6)
M(2) - O(2) - M(3)	132.98 (4)	133.05 (2)	133.03 (1)

Table A.2: Comparison of the interatomic distances of pure V_2O_3 at 600°C [62] and two differently doped with 1% [66] and 3.8% [65] of Chromium in the insulating phase (standard deviations in brackets).

Bibliography

[1] P. Majumdar and H. R. Krishnamurthy, Phys. Rev. Lett. **73**, 1525 (1994).

[2] P. Majumdar and H. R. Krishnamurthy, Phys. Rev. B **52**, R5479 (1995).

[3] S. R. Hassan, A. Georges, and H. R. Krishnamurthy, Phys. Rev. Lett. **94**, 036402 (2005).

[4] P. Limelette, *Propriétés de transport de systemes électroniques fortement corrélés*, PhD thesis, Université Paris XI, Orsay, France, 2003.

[5] P. Limelette *et al.*, Science **302**, 89 (2003).

[6] H. Bethe, Annalen der Physik **392**, 55 (1928).

[7] A. H. Wilson, Royal Society of London Proceedings Series A **133**, 458 (1931).

[8] J. H. de Boer and E. J. W. Verwey, Proceedings of the Physical Society **49**, 59 (1937).

[9] E. Wigner, Trans. Faraday Soc. **34**, 678 (1938).

[10] M. Imada, A. Fujimori, and Y. Tokura, Rev. Mod. Phys. **70**, 1039 (1998).

[11] D. B. McWhan *et al.*, Phys. Rev. Lett. **27**, 941 (1971).

[12] X. Obradors *et al.*, Phys. Rev. B **47**, 12353 (1993).

[13] S. Lefebvre *et al.*, Phys. Rev. Lett. **85**, 5420 (2000).

[14] P. Limelette *et al.*, Phys. Rev. Lett. **91**, 016401 (2003).

[15] K. Kanoda, JOURNAL OF THE PHYSICAL SOCIETY OF JAPAN **75** (2006).

[16] J. A. Wilson, *The Metallic and Nonmetallic States of Matter* (Taylor and Francis, London, 1985).

[17] J. B. Torrance, P. Lacorre, A. I. Nazzal, E. J. Ansaldo, and C. Niedermayer, Phys. Rev. B **45**, 8209 (1992).

[18] H. Takagi *et al.*, Phys. Rev. B **40**, 2254 (1989).

[19] A. Fujimori, Journal of Physics and Chemistry of Solids **53**, 1595 (1992), Special Issue Elecronic Structure and Fermiology of High-Tc Superconductors.

[20] Y. Tokura, J. B. Torrance, T. C. Huang, and A. I. Nazzal, Phys. Rev. B **38**, 7156 (1988).

[21] S. A. Carter, T. F. Rosenbaum, P. Metcalf, J. M. Honig, and J. Spalek, Phys. Rev. B **48**, 16841 (1993).

[22] T. Katsufuji and Y. Tokura, Phys. Rev. B **50**, 2704 (1994).

[23] N. F. Mott, Proceedings of the Physical Society. Section A **62**, 416 (1949).

[24] N. F. Mott, Can. J. Phys. **34**, 1356 (1956).

[25] N. F. Mott, Philosophical Magazine **6**, 287 (1961).

[26] N. F. Mott, Advances in Physics **16**, 49 (1967).

[27] J. Hubbard, Royal Society of London Proceedings Series A **276**, 238 (1963).

[28] J. Hubbard, Royal Society of London Proceedings Series A **277**, 237 (1964).

[29] J. Hubbard, Royal Society of London Proceedings Series A **281**, 401 (1964).

[30] A. Georges, G. Kotliar, W. Krauth, and M. J. Rozenberg, Rev. Mod. Phys. **68**, 13 (1996).

[31] A. Georges and G. Kotliar, Phys. Rev. B **45**, 6479 (1992).

[32] E. H. Lieb and F. Y. Wu, Phys. Rev. Lett. **20**, 1445 (1968).

[33] D. M. EDWARDS and A. C. HEWSON, Rev. Mod. Phys. **40**, 810 (1968).

[34] W. F. Brinkman and T. M. Rice, Phys. Rev. B **2**, 4302 (1970).

[35] M. C. Gutzwiller, Phys. Rev. **137**, A1726 (1965).

[36] G. Kotliar, S. Y. Savrasov, G. Pálsson, and G. Biroli, Phys. Rev. Lett. **87**, 186401 (2001).

[37] D. Fournier, M. Poirier, M. Castonguay, and K. D. Truong, Phys. Rev. Lett. **90**, 127002 (2003).

[38] D. Fournier, M. Poirier, and K. D. Truong, Physical Review B (Condensed Matter and Materials Physics) **76**, 054509 (2007).

[39] M. Lang and J. Mueller, Organic superconductors, 2003.

[40] M. de Souza *et al.*, Physical Review Letters **99**, 037003 (2007).

[41] M. de Souza, P. Foury-Leylekian, A. Moradpour, J.-P. Pouget, and M. Lang, Physical Review Letters **101**, 216403 (2008).

[42] A. Jayaraman, D. B. McWhan, J. P. Remeika, and P. D. Dernier, Phys. Rev. B **2**, 3751 (1970).

[43] M. Yethiraj, Journal of Solid State Chemistry France **88**, 53 (1990).

[44] D. ADLER, Rev. Mod. Phys. **40**, 714 (1968).

[45] M. Foex, C. R. Acad. Sci. **223**, 1126 (1946).

[46] D. B. McWhan, T. M. Rice, and J. P. Remeika, Phys. Rev. Lett. **23**, 1384 (1969).

[47] D. B. McWhan and J. P. Remeika, Phys. Rev. B **2**, 3734 (1970).

[48] D. B. McWhan, A. Menth, J. P. Remeika, W. F. Brinkman, and T. M. Rice, Phys. Rev. B **7**, 1920 (1973).

[49] Y. Ueda, K. Kosuge, and S. Kachi, Journal of Solid State Chemistry France **31**, 171 (1980).

[50] N. Otsuka, H. Sato, G. L. Liedl, and J. M. Honig, Journal of Solid State Chemistry France **44**, 230 (1982).

[51] R. E. Newnham and Y. M. de Haan, Z. Krist **117**, 235 (1962).

[52] F. J. Morin, Phys. Rev. Lett. **3**, 34 (1959).

[53] R. M. Moon, Phys. Rev. Lett. **25**, 527 (1970).

[54] E. P. Warekois, J. Appl. Phys. Suppl. **31**, 346S (1960).

[55] P. D. Dernier and M. Marezio, Phys. Rev. B **2**, 3771 (1970).

[56] D. B. McWhan and T. M. Rice, Phys. Rev. Lett. **22**, 887 (1969).

[57] A. C. Gossard, D. B. McWhan, and J. P. Remeika, Phys. Rev. B **2**, 3762 (1970).

[58] D. B. McWhan, A. Menth, and J. P. Remeika, J. Phys. (Paris) **C 32**, 1079 (1971).

[59] A. Menth and J. P. Remeika, Phys. Rev. B **2**, 3756 (1970).

[60] S. A. Shivashankar and J. M. Honig, Phys. Rev. B **28**, 5695 (1983).

[61] H. Kuwamoto and J. Honig, Journal of Solid State Chemistry France **32**, 335 (1980).

[62] W. R. Robinson, Acta Crystallographica Section B **31**, 1153 (1975).

[63] L. F. Mattheiss, Journal of Physics Condensed Matter **6**, 6477 (1994).

[64] S. Chen, J. E. Hahn, C. E. Rice, and W. R. Robinson, Journal of Solid State Chemistry **44**, 192 (1982).

[65] P. D. Dernier, Journal of Physics and Chemistry of Solids **31**, 2569 (1970).

[66] W. R. Robinson, Materials Research Bulletin **9**, 1091 (1974).

[67] H. Harrison, R. Aragon, and C. Sandberg, Mater. Res. Bull. **15**, 571 (1980).

[68] L. S. C. Inc., Cryogenic temperature controller, Model 340.

[69] DuPont-Electronics, single component epoxy cement (amine-curing agent), No. 6838.

[70] Yokogawa, Digital oscilloscope, DL 1620.

[71] Farnell, Resistor, WCR 0805 100R.

[72] E. Produits, high temperature epoxy resin, Structuralit 3446.

[73] P. J. Seebeck, Pogg. Ann. **6**, 133 (1826).

[74] W. D. Knight, Phys. Rev. **76**, 1259 (1949).

[75] C. P. Slichter, *Principles of Magnetic Resonance*, 3rd ed. (Springer Verlag, 1989).

[76] A. MENTH, A. C. GOSSARD, and J. P. REMEIKA, Journal de Physique Colloques **32**, C1 (1971).

[77] L. Landau and E. Lifschitz, *Théorie de l'Elasticité* (Editions Mir, 1967).

[78] H. Schade and K. Neemann, *Tensoranalysis*, 2nd ed. (de Gruyter, 2006).

[79] Tuell, R. and Elbaum, C. and Chick, B. B., *Ultrasonic Methods in Solid State Physics*, 1st ed. (Academic press, 1969).

[80] D. N. Nichols, R. J. Sladek, and H. R. Harrison, Phys. Rev. B **24**, 3025 (1981).

[81] H. Yang and R. J. Sladek, Phys. Rev. B **34**, 2627 (1986).

[82] Y. P. Varshni, Phys. Rev. B **2**, 3952 (1970).

[83] H. Yang, R. J. Sladek, and H. R. Harrison, Solid State Communications **47**, 955 (1983).

[84] D. N. Nichols and R. J. Sladek, Phys. Rev. B **24**, 3155 (1981).

[85] H. Yang, R. J. Sladek, and H. R. Harrison, Phys. Rev. B **31**, 5417 (1985).

[86] L. Landau, Phys. Abh. Sowjun. **11**, 26 (1937).

[87] W. Rehwald, Advances in Physics **22**, 721 (1973).

[88] C. Castellani, C. D. Castro, D. Feinberg, and J. Ranninger, Phys. Rev. Lett. **43**, 1957 (1979).

[89] G. Kotliar, European Physical Journal B **11**, 27 (1999), arXiv:cond-mat/9903188.

[90] M. J. Rozenberg, R. Chitra, and G. Kotliar, Phys. Rev. Lett. **83**, 3498 (1999).

[91] G. Kotliar, E. Lange, and M. J. Rozenberg, Phys. Rev. Lett. **84**, 5180 (2000).

[92] A. Georges, S. Florens, and T. A. Costi, JOURNAL DE PHYSIQUE IV **114**, 165 (2004).

[93] F. J. Blatt, P. A. Schroeder, and C. L. Foiles, *Thermoelectric power in metals*, 1st ed. (Plenum Press, 1976).

[94] J. M. Ziman, *Electrons and phonons*, 1st ed. (Oxford University, 1960).

[95] P. M. Chaikin, R. L. Greene, S. Etemad, and E. Engler, Phys. Rev. B **13**, 1627 (1976).

[96] G. Pálsson and G. Kotliar, Phys. Rev. Lett. **80**, 4775 (1998).

[97] N. W. Ashcroft and N. D. Mermin, *Solid State Physics*, 1st ed. (Brooks/Cole, 1976).

[98] N. F. Mott and E. A. Davis, *Electronic processes in non-crystalline materials*, 1st ed. (Claredon press, Oxford, 1971).

[99] H. Kuwamoto, J. M. Honig, and J. Appel, Phys. Rev. B **22**, 2626 (1980).

[100] A. Sinha, G. Chandrashekhar, and J. Honig, Journal of Solid State Chemistry **12**, 402 (1975).

[101] I. G. Austin and C. E. Turner, Philosophical Magazine **19**, 939 (1969).

[102] G. Wiedemann and R. Franz, Ann. Phys. **89**, 497 (1853).

[103] O. Maldonado, Cryogenics **32**, 908 (1992).

[104] V. Andreev, F. Chudnovskii, A. Petrov, and E. Terukov, PHYSICA STATUS SOLIDI A-APPLIED RESEARCH **48**, K153 (1978).

[105] H. Watanabe, Metrologia **39**, 65 (2002).

[106] M. J. Rozenberg *et al.*, Phys. Rev. Lett. **75**, 105 (1995).

[107] S.-K. Mo *et al.*, Phys. Rev. Lett. **93**, 076404 (2004).

[108] S.-K. Mo *et al.*, Physical Review B (Condensed Matter and Materials Physics) **74**, 165101 (2006).

[109] K. Held, G. Keller, V. Eyert, D. Vollhardt, and V. I. Anisimov, Phys. Rev. Lett. **86**, 5345 (2001).

[110] T. Pruschke, M. Jarrell, and J. Freericks, ADVANCES IN PHYSICS **44**, 187 (1995).

[111] V. S. Oudovenko and G. Kotliar, Phys. Rev. B **65**, 075102 (2002).

[112] V. S. Oudovenko, G. Pálsson, K. Haule, G. Kotliar, and S. Y. Savrasov, Physical Review B (Condensed Matter and Materials Physics) **73**, 035120 (2006).

Investigation of the Mott transition in chromium doped V_2O_3 by means of ultrasound and thermopower experiments

This work presents an experimental study of the high temperature Mott transition in chromium doped V_2O_3 by means of two different experimental techniques at pressures between ambient pressure and 6 kbar and temperatures from room T to 500 K. Ultrasound measurements as a direct probe of the compressibility were used to estimate the effects of the lattice on the Mott transition. We were able to present the first systematic study of the influence of the lattice degrees of freedom on the high temperature Mott transition in V_2O_3 and could verify the existence of a critical electronic temperature $T^{el}{}_c$ that differs in the order of 3% or 4% from the temperature of the transition T_c of the bulk sample. Furthermore, observation of the behaviour of the transversal mode of the speed of sound allowed to conclude that this transition occurs without symmetry breaking and the order parameter is a scalar. In the second part the evolution of the Seebeck coefficient was investigated under the same experimental conditions. The studies around the critical point allowed us to establish an experimental phase diagram. Furthermore, we were able to show that the change of the Seebeck coefficient at the Mott transition is driven by the change in the resistivity rather than by the change of the particle-hole symmetry. As a consequence of this we could relate the scaling laws for the critical parameters related to conductivity to our data. In the vicinity of the transition our data were quite well reproduced by the mean field exponents found in the conductivity experiments.

Étude de la transition de Mott dans V_2O_3 dopé avec chrome par mesures de la vitesse du son et du pouvoir thermoélectrique

Cette thèse présente une étude expérimentale de la transition de Mott dans V_2O_3 dopé au chrome par deux différentes techniques expérimentales entre la température ambiante à 500 K et sous pressions jusqu'à 6 kbar. La technique ultrasonore fournit une mesure directe de la compressibilité et a été utilisé pour estimer les effets de la réseau sur la transition de Mott. Nous avons été en mesure de mener la première étude systématique de l'influence des degrés de liberté du réseau sur la transition de Mott dans V_2O_3. On a vérifiée l'existence d'une température électronique critique $T^{el}{}_c$ qui diffère de l'ordre de 3% ou 4% par rapport à la température de transition effectivement observée T_c. L'observation du comportement du mode transverse de la vitesse du son a permis de conclure que la transition de Mott à haute température a lieu sans brisure de symétrie et le paramètre d'ordre est un scalaire. Dans la deuxième partie de la thèse l'évolution de coefficient du Seebeck a été étudiée dans les mêmes conditions expérimentales. Les études autour du point critique nous ont permis d'établir un diagramme de phase expérimentale. Nous avons montré que le changement de S à la transition est dominé par le changement de la résistivité plutôt que par le changement de la symétrie particule-trou. En conséquence, nous avons pu relier les lois d'échelle pour les paramètres critiques relatifs à la conductivité à nos données. Dans le voisinage de la transition nos données sont assez bien reproduites par les exposants de champ moyen observés dans les mesures de conductivité.